**DELFT UNIVERSITY OF TECHNOLOGY**

# FEASIBILITY STUDY OF COHESIVE ZONE MODEL ON CRACK PROPAGATION IN PIPELINE STEEL UNDER MONOTONIC AND FATIGUE LOADING

**Yipei Zeng**

**Student ID: 4319060**

**Y.Zeng@student.tudelft.nl**

**Section of Steel and Timber Constructions**
**Track of Structural Engineering**
**Faculty of Civil Engineering and Geosciences**
**Delft University of Technology**
**The Netherlands**
**February 2015**

# CONTENT

## ACKNOWLEDGEMENT

This master thesis project is conducted as a conjunction program between Technological University of Delft and Allseas. I would like to dedicate my sincere appreciation to the two corporations for providing me the right platform to carry out my thesis study.

Meanwhile, there are many names that I feel respectful to and can never get out of my mind. I would like to express my thanks to Prof. F.S.K. Bijlaard, Prof. L.J. Sluys and Dr. M.H. Kolstein and Ir. L. Houben, my university supervisors, for guiding me through the whole process from the very beginning. I feel grateful to Dr. B. Hu and Dr.N. Ermolaeva, my daily supervisors in the company, for providing me the chance and being supportive to improve my problem-solving skills. Also many thanks are delivered to Dr. L. Zhang for your patience as always in answering my questions.

Furthermore I would like to give a special thank you to Dr. Ingo Scheider. Although our contact was just between two emails, you showed your kindness sharing your experience with ABAQUS, which could mean a lot to me.

I feel very fortunate and honourable to have my excellent colleagues from the company and from the university. Thank you all for your friendship and your companion.

Last but not the least, I would like to thank my parents and family for everything you have done for me all the way coming along.

## NOMENCLATURE

| | |
|---|---|
| a | Crack Length |
| $\Delta a$ | Crack Extension Length |
| G | Energy Release Rate |
| Gc | Critical Value of Energy Release Rate |
| J | J-integtral |
| Jc | Critical Value of J-integral |
| K | Stress Intensity Factor |
| Kc | Critical Value of Stress Intensity Factor |
| Ki | Stress Intensity Factor at Crack Initiation |
| $K_I$ | Stress Intensity Factor at Crack Opening Mode 1 |
| $\Delta K$ | Range of Stress Intensity Factors |
| $\Delta K_{th}$ | Threshold Value of the Range of Stress Intensity Factors |
| $l_{cz}$ | Length of Cohesive Zone |
| W | Width of the Fracture Specimen |
| $\delta_0$ | Characteristic Separation |
| $\delta_c$ | Critical Separation |
| $\sigma_{\max}$ | Cohesive Strength |
| $\Gamma_n$ | Cohesive Energy |
| $\Omega$ | Domain of the Entity |
| $\Gamma_{ext}$ | Boundaries where externally imposed conditions is applied |
| $\Gamma_c$ | Boundaries of the discontinuity (cohesive zone) |
| CZM | Cohesive Zone Model |
| TSL | Traction-Separation Law |

## ABSTRACT

In this thesis project, author aimed to study the feasibility of the cohesive zone model in numerical simulation of crack propagation in pipeline steel.

In Section 3, the parametric study suggested preliminary parameter values calibrated from a SENT fracture specimen as $\Gamma_n \approx 3\% \frac{K_{Ic}^2}{E'}$, $\sigma_{\max} \approx 1.5\sigma_y$. The huge difference between the suggested values from the literature and the numerical results implies that the calibrated cohesive parameters should be distinguished for different TSLs, i .e there exists a TSL-shape dependency for the calibration of the cohesive parameter.

The influences of the cohesive parameters are studied through series of analysis. The cohesive energy indicates the energy needed for the full development of the cohesive zone. The relationship between the cohesive energy and the J-integral evaluated at the crack initiation can be found as $J_{\text{ini}} = \Gamma_n$. While the cohesive strength influences the plastification developing near the crack tip. A larger value allows for a higher level of plastification in the material and delays or prevents the full development of the cohesive zone and vice versa. Also a higher value of the cohesive strength increases the slope of the J-resistance curve, such increment in the crack resistance suggests $J = \Gamma_n + J_{pl}$ , i.e. the energy input from the applied load is absorbed by both creating new crack surface and plastification of material surrounding the crack tip. Meanwhile, for the triangle-shaped TSL, the initial stiffness is found to have a minor influence on the crack propagation.

The difference between the experiments and simulation results has suggested “more ductile” crack propagation in pipeline steel than the standard cohesive element is able to capture. The triangle-shaped TSL describes brittle or quasi brittle crack behaviour and is not suitable to model the fracture behaviours of the pipeline steel X65.

In Section 4, based on the proposition of Needleman, the author implemented a different TSL into a user defined cohesive element via ABAQUS Subroutine UEL. The complete element formulation for the axis-symmetrical problem is derived. The programming structure is provided. Accounting for the possible overclosure effect, a contact algorithm is implemented and has been verified in a simple patch test model.

In Section 5, the saturation problem has been verified with ABAQUS standard cohesive element on its incapability in fatigue crack propagation. An existing damage accumulation model introducing more model parameters proposed by Roe and Siegmund is applied. Regarding the newly introduced damage accumulation model, the influences of two additional parameters, the accumulative cohesive length $\delta_\Sigma$ and the endurance limit $\sigma_f$ are studied on a qualitative base. The accumulative cohesive length scales the separation increment and determines the amount of accumulated separation (or plastic deformation) at a certain load level. While the endurance limit incorporates the concept of stress into the damage model and controls the effective load range. The qualitative study verifies the model features and shows the potential of such user-defined cyclic cohesive element in fatigue simulation. Meanwhile, the cyclic CZM is proven more suitable for low-cycle fatigue problems. Since the evolution of the damage

is not monitored on a quantitative base, the functionality of the cyclic CZM needs to be looked into further and verified in its applications.

# 1.0 INTRODUCTION

## 1.1 Background

In engineering application, prevention and assessment of fracture and damage processes play an essential role in the development and designing of engineering constructions, components, and facilities in order to ensure their technical safety, durability, and reliability [8]. The various types of loading can lead to the occurrence of cracking, for instance static loading during load bearing conditions, fatigue loading from the internal pressure variation in the pipe. For the industry of pipe-laying, the propagation of a crack can finally lead to failure of the structural components. This may cause catastrophic consequences for the environment, the economy and even the lives of people. In many engineering components and materials, defects may exist as results from manufacturing or operation, such as collision, welding process etc. It is also very hard to ensure the structure is functioning free from such defects. Therefore, the mechanical assessment of crack-like defects is of great importance in engineering practice.

To understand better the fracture phenomenon and factors influencing the fracture process, a large variety of investigations have been carried out both experimentally and numerically. Fracture mechanics has been well applied in crack propagation prediction in large number of studies. However, such methods are not readily applicable to non-linear problems [2]. Application of cohesive zone models (CZM), as an alternative approach, has become more and more popular over the past two decades or more.

From different respective to fracture mechanics, the concept of CZM regards the fatigue crack process as a result of material deterioration with damage concentrated at the cohesive zone. By definition, this approach is more physically based and is able to cover both crack initiation period and crack propagation period, provided an appropriate material model [8]. Former experiments have shown its potential to model the crack initiation but necessarily with more rigorously determined model parameters [3]. Different from the classical fracture mechanics approach, the unrealistic singularities at the crack tip are removed. As no restrictive conditions are required to be imposed on the ratio of the length of the crack to the size of the plastic zone or the geometrical characteristic lengths, problems in which the conditions of small-scale yielding are violated can be advantageously addressed [9].

## 1.2 Objective

The application of CZM in ductile crack propagation has been studied over the recent three decades. As a essential part of the CZM, several Traction-Separation Law (TSL) has been developed. As will be addressed in Section 2.4 in more detail, in 1990, Needleman proposed an exponential TSL to describe micro damage. The normal traction versus separation relation across the interface is specified to have an exponential form consistent with the universal binding energy correlation of ROSE et al. (1981, 1983) and FERRANTE and SMITH (1985) [7]. This model has been applied for parameter calibration for metals such aluminium [23] and stainless steel [28]. There application for pipeline steel, specifically X65 is yet to be explored. From literature, similar simulation has given suggestions for the parameter calibration, for instance, the cohesive parameters for structural steel are determined around

$\Gamma_n \approx \frac{K_{Ic}^2}{E'}$, $\sigma_{\max} \approx 3\sigma_y$ [49],[16]. The commercial software ABAQUS has provided a triangle-shaped TSL. In [47], it is suggested that the influence of the TSL shape plays a minor role in crack propagation. However, this may not be a concrete conclusion for every material such as pipeline steel. It is interesting to study about the feasibility of the provided triangle TSL in simulation of crack propagation in pipeline steel under monotonic and fatigue loading. Will the cohesive parameters calibrated depend on the choice of TSL? If yes, to what level will the difference be and what is the reason for this? On the other hand, through a series of parametric study and comparison with experimental data, it is necessary to have a deeper understanding on the influences of the cohesive parameters on the crack propagation applying the triangle-shaped TSL. Also there is a debate on whether the initial stiffness will place an effect on the simulation on the crack propagation and this issue will also be addressed in this project.

Meanwhile, in recent two decades, cohesive zone model has also been adapted for fatigue simulations, sometimes also referred to as the cyclic cohesive zone model [2]. With introduced damage accumulation model, this method has been successfully employed to predict fatigue crack growth in metals [4, 13, 32], composite materials [3], fibre-metal laminate [31], weld specimen [2], and so on. Specifically, Silitonga et al [13][32] applied a cyclic cohesive zone with a certain damage accumulation model to simulate the fatigue crack propagation in Aluminum specimens via a Subroutine UEL. Also they managed to show the potential of cyclic CZM in predicting overload effect by looking into the decreasing interface separation. However, this model considered only separation with positive values and so as the applied load. While the plasticity induced crack closure effect could have an impact on the fatigue crack propagation [15], a numerical simulation accounting for this effect involves a separate implementation of a contact algorithm for loading cases with overclosure of the crack interfaces. In this project, a variety of load cases including compression is considered while implementing the user element in to the ABAQUS code. Furthermore, it is necessary to check about the features of the damage accumulation model from both a numerical and physical point of view.

# 2.0 THEORIES

## 2.1 Fracture Mechanics

### 2.1.1 Fracture Phenomena

The term “fracture” describes the local detachment of material cohesion in a solid body [8]. Locally the fracture process can be described on a microscopic level and is controlled by its physical and micro-structural properties. The global appearance of the fracture on a macroscopic level consists of formation and propagation of one or multiple cracks in the body and can be addressed applying the solid mechanics and mechanics of material [14]. As the fracture and failure process occur on all length scales, different perspectives are taken for different purposes. For instance, the engineers may prefer the macroscopic scale while the material scientists find more interest in the microscopic phenomena of a material. According to the author’s academic background, the cracking process in this project is studied on the macroscopic level. A draft regarding different level of fracture processes is shown in Fig.1

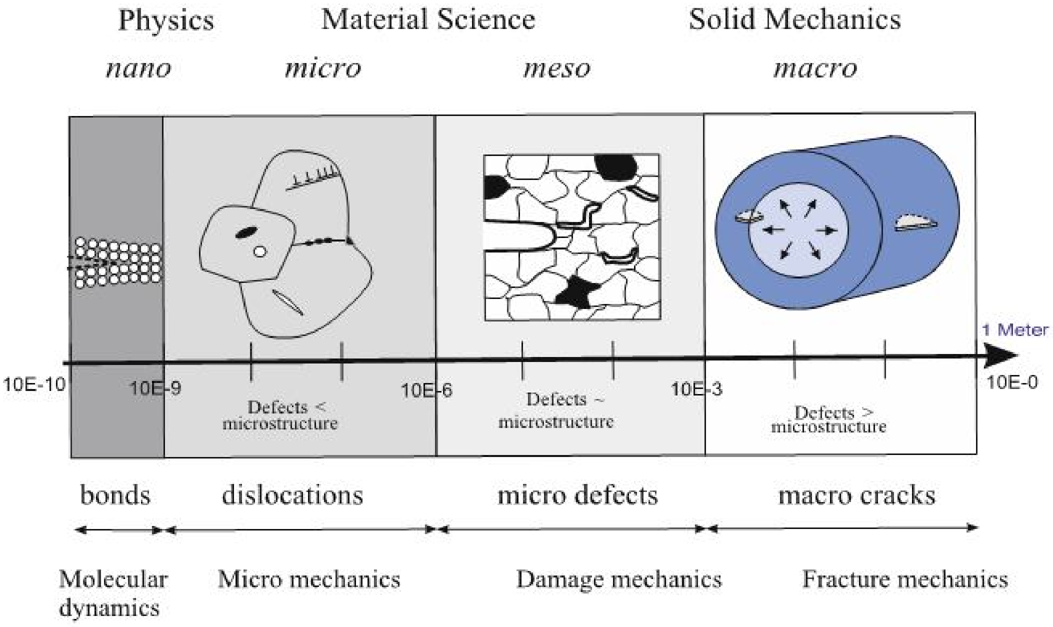

Figure 1 Fracture Processes as Different Scales and Levels [8]

The specific field which deals with fracture and failure processes in engineering materials and constructions is called fracture mechanics [8]. In fracture mechanics, the defects are explicitly introduced as cracks, representing the defects due to the manufacturing process, e.g. material delamination, initial cracks, pores, flaws, etc.

### 2.1.2 Classification of Fracture Growth

1. According to the Type of Loading

The types of fracture can be assigned to different mechanical loads, based on their temporal features. Static loads are often considered typically in loading-bearing structures; dynamic loads are associated with accelerated deformation and inertia forces [8]; (cyclic or random) variable loads with even low value can lead to crack formation and propagation and finally to the failure of the structure. This project covers the fracture growth under monotonic static loading and fatigue loading. The former is studied in details.

2. According to the Stability

A crack that can extend abruptly without increasing the external loading is called unstable; whilst a crack that grows with the necessity of increasing external loading is called stable.

3. According to the inelastic deformations of material

For brittle fracture, the load-displacement runs linearly till the crack initiation and the plastic zones are very small; for ductile fracture, the fracture process is associated with large inelastic deformation in the material and the load-displacement diagram shows a non-linear relationship.

### 2.1.3 Fracture modes

In fracture mechanics some assumptions are made to define a crack. Firstly, the separation of the body is described as two crack faces (2D) or two crack surfaces (3D), which converge at the crack tip (2D) or crack front (3D). Secondly, an ideal sharp crack tip, considering its size to the crack length and the body dimensions, is assumed with radius $\rho=0$, although in reality the crack tip always has a finite radius of curvature [15].

With regard to different movements of the two crack faces, three independent modes are distinguished as following and schematically described in Fig.2:

Mode 1: Opening mode: the crack opens perpendicular to crack plane. This can be caused by tension or bending;

Mode 2: In-plane sliding mode: the crack faces are displaced perpendicular to the crack front in their plane;

Mode 3: Out-of-plane tearing mode: the crack faces are displaced parallel to the crack front in their plane.

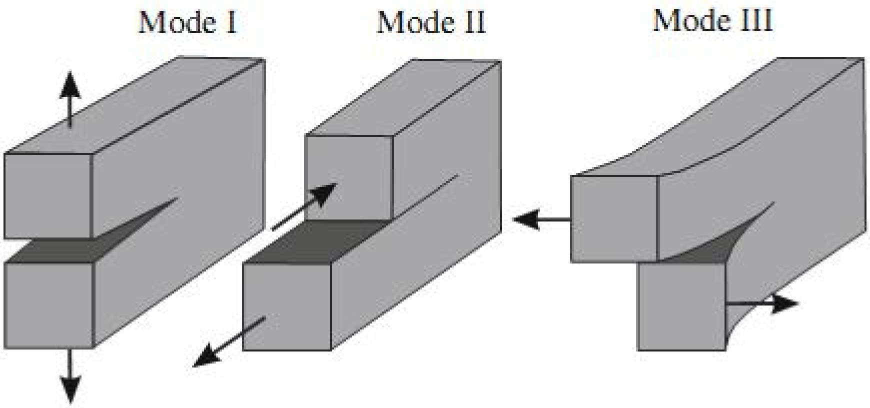

Figure 2 Three Crack Opening Modes [8]

### 2.1.4 Linear-Elastic Fracture Mechanics

In Linear-Elastic Fracture Mechanics (LEFM), crack problems are in bodies whose deformation behaviour can be assumed to be linear-elastic [8]. The realistic material or geometrical non-linearity effects is considered to be negligible taking into account that such effects are limited in small areas neglected compared to the crack size or the body dimensions. In this section, some basic concepts from LEFM are introduced and attention will be paid to mainly 2D crack problems.

#### 2.1.4.1 Eigenfunctions of Plane Elastic Crack Problem

Solutions for elastic plane problems as boundary value problems are obtained by Williams in 1957 [36]. As listed below, the stress and displacement field can be formulated in the form of complete series expansion in polar coordinates, where the unknown coefficients $a_n$ , $b_n$ and $c_n$ needs to be determined by the boundary conditions and represent different modes respectively [8, 36].

$$\sigma_{\mathrm{ij}}(r,\theta)=\sum_{n=1}^{\infty} r^{\frac{n}{2}-1}\left[a_n\tilde{M}_{ij}^{(n)}(\theta)+\mathrm{b}_n\tilde{N}_{ij}^{(n)}(\theta)+\mathrm{c}_n\tilde{L}_{ij}^{(n)}(\theta)\right]$$

$$u_{\mathrm{i}}(r,\theta)=\frac{1}{2\mu}\sum_{n=1}^{\infty}\left[a_n\tilde{F}_i^{(n)}(\theta)+\mathrm{b}_n\tilde{G}_i^{(n)}(\theta)+\mathrm{c}_n\tilde{H}_i^{(n)}(\theta)\right] \tag{Eq.1}$$

For Mode I, with order n=1, the well known near field solutions are obtained as following [8]. One may extend to higher order terms, e.g. n=2 with second order terms known as the T- stresses to study the constraint effect [27].

$$\begin{Bmatrix}\sigma_{11}\\ \sigma_{22}\\ \tau_{12}\end{Bmatrix}=\frac{K_I}{\sqrt{2\pi r}}\begin{Bmatrix}\cos\frac{\theta}{2}\left[1-\sin\frac{\theta}{2}\sin\frac{3\theta}{2}\right]\\ \cos\frac{\theta}{2}\left[1+\sin\frac{\theta}{2}\sin\frac{3\theta}{2}\right]\\ \sin\frac{\theta}{2}\cos\frac{\theta}{2}\cos\frac{3\theta}{2}\end{Bmatrix}=\frac{K_I}{\sqrt{2\pi r}}\begin{Bmatrix}f_{11}^I(\theta)\\ f_{22}^I(\theta)\\ f_{12}^I(\theta)\end{Bmatrix}$$

$$\sigma_{33}=0\ for\ plane\ stress;$$

$$\sigma_{33}=\upsilon(\sigma_{11}+\sigma_{22})=\frac{K_I}{\sqrt{2\pi r}}2\upsilon\cos\frac{\theta}{2}\ for\ plane\ strain$$

$$\begin{Bmatrix}u_1\\ u_2\end{Bmatrix}=\frac{K_I}{2\mu}\sqrt{\frac{r}{2\pi}}\begin{Bmatrix}\cos\frac{\theta}{2}\left[\kappa-\cos\theta\right]\\ \sin\frac{\theta}{2}\left[\kappa-\cos\theta\right]\end{Bmatrix}=\frac{K_I}{2\mu}\sqrt{\frac{r}{2\pi}}\begin{Bmatrix}g_1^I(\theta)\\ g_2^I(\theta)\end{Bmatrix} \tag{Eq. 2}$$

#### 2.1.4.2 Stress Intensity Factor: K-concept

For isotropic linear-elastic material behaviour, the asymptotic near field solutions are always of the same mathematical form [8] as one can see in the above equations in Section 2.1.4.1. Such field is entirely determined by the stress intensity factors (SIF), which is determined by the solution of the specific boundary value problem and thus depends on the geometry of the body, crack size, applied loading, etc. The concept of SIF is developed by Irwin [37], based on the following ideas:

a) The dominance of $K_I$ is strong in a finite region round the crack tip with radius of $r_k$ and fades at the larger distance $r>r_k$;

b) In reality, a fracture process zone with a size of $r_B$ develops where the elasticity theory is violated and K-singularity is not valid. However, it is assumed that $r_B$ is much smaller than $r_k$ so that the fracture process are controlled by the K-near-field-solution,

c) The fracture process is controlled by the SIF, independent of the type of crack configuration[8]. Thus, the boundary value problem is incorporated into the SIF as:

K=K(geometry, loading, fracture, material)

d) Crack initiates when the SIFs reaches a critical material limit ($K=K_c$), which is known as fracture toughness and can be experimentally determined by means of a standard fracture experiments.

#### 2.1.4.3 Energy release rate

The energy balance during crack propagation in conservative system is compiled by Griffith (1921) as following [38]:

$$\frac{\Delta(W_{ext} - W_{\text{int}})}{\Delta A} = -\frac{\Delta\Pi}{\Delta A}$$

**(Eq.3)**

Where the right-hand-side represents the amount change of potential energy, supplied by the left-hand-side: the external load and elastically stored internal energy during crack propagation by ΔA[8] (increment of crack surface area). The former is denoted as energy release rate G when ΔA reaching infinite small (zero), i.e.

$$G = -\lim_{\Delta A \to 0} \frac{\Delta\Pi}{\Delta A} = -\frac{d\Pi}{dA}$$

**(Eq.4)**

The energetic fracture criterion by Griffith states that a crack initiates when the provided energy release rate reaches a critical material parameter G= Gc. The dimension of G is [force*length/length$^2$] or J/m$^{2,}$ N/m. The relation between the parameters G and K in LEFM can is given as [8]

$$\begin{aligned} &G_I == \frac{K_I^2}{E'} \\ &\textit{with } E' = E \textit{ in plane stress;} \\ &E' = \frac{E}{1-\upsilon^2} \textit{ in plane strain.} \end{aligned}$$

**(Eq.5)**

#### 2.1.4.4 J-integral

Cherepanove(1967) and Rice(1968) introduced another fracture-mechanical load parameter – the J-integral[8]. The formerly introduced concept, energy release rate can be expressed with such path-independent line integral, i.e. G=J (related issues will be specified in Section 3.3). This parameter has proven extremely valuable not only in linear-elastic fracture mechanics but also in application at inelastic material behaviour [8].

### 2.1.5 Elastic-Plastic Fracture Mechanics

Pipeline steel materials possess elastic-plastic deformation behaviour. The high stress concentration at the crack tip can exceed the material yield limit under a low remote loading the thus plastic zone is formed. The size of the plastic zone can expand with increasing loading. Different stages of the plastification in a body are shown schematically in Fig.3.

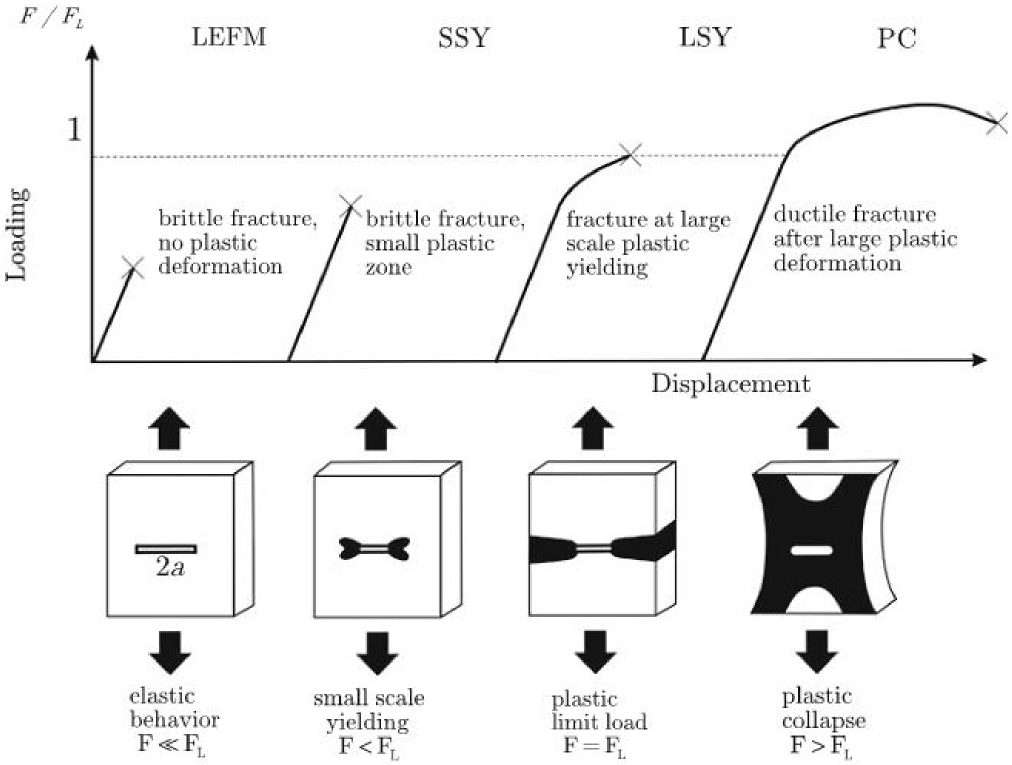

Figure 3 Stages of Plastic Deformation in a Body with Crack [8]

It causes a redistribution of the stress and strain field which leads to blunting of the crack tip[8]. The increasing plastification is accompanied with enhancement of the force-displacement curve. The higher ratio of fracture toughness and yield stress of the material, the higher is the extent of the plastification before facture[8]. Thus the plastic deformation influences the crack process and this task is pursued in Elastic-Plastic Fracture Mechanics (EPFM).

### 2.1.5.1 Small scale yielding

Small scale yielding (SSY) refers to the situation where the size of the plastic zone is small compared to the length of the crack and the body dimensions [8]. For ideal-plastic material, by inserting the stresses from the elastic crack tip solution into the Von Mises yield criterion, the plastic zone size can be obtained as following, according to Irwin's correction[8]:

$$r_p(\theta=0)=\frac{1}{2\pi}\left(\frac{K_I^2}{\sigma_F}\right)^2\begin{cases}1 & \textit{plane stress}\\(1-2\upsilon)^2 & \textit{plane strain}\end{cases}$$

$$\textit{with } \sigma_F \textit{ the yield stress} \qquad \text{(Eq.6)}$$

**The Dugdale's model**

In 1960, Dugdale created a fracture model[5] as a superposition of two condition, see Fig.4

1. A hypothetical crack with length 2(a+d) in an infinite plane under constant tension $\sigma$ , where d represents the length of a strip on which the plastic deformation is concentrated.
2. The material in the yield zone ( $a<|x_1|<a+d$ ) compressed by the traction force on the crack surfaces.

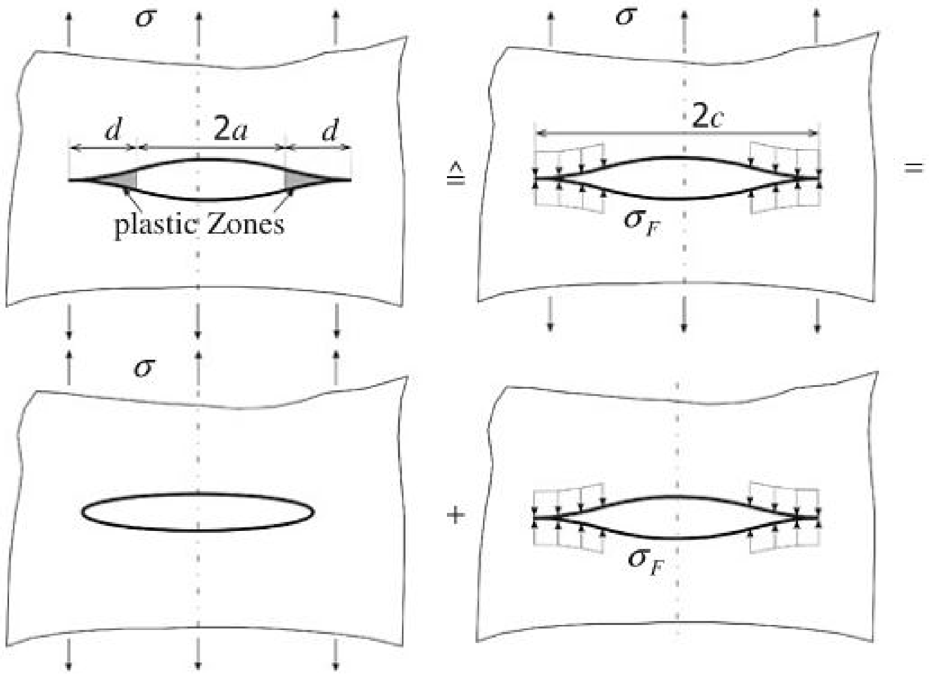

Figure 4 Dugdale's Model for Strip Yield Zone [8]

### 2.1.5.2 J-integral in EPFM

The near field solution derived for an elastic-plastic material by Hutchinson and Rice & Rosengreen is given below, known as HRR-field [8].

$$
\begin{aligned}
\sigma_{ij} &= \sigma_0 \left[ \frac{J}{\alpha\varepsilon_0\sigma_0 I_n} \frac{1}{r} \right]^{\frac{1}{n+1}} \tilde{\sigma}_{ij}(\theta, n) \\
\varepsilon_{ij} &= \alpha\varepsilon_0 \left[ \frac{J}{\alpha\varepsilon_0\sigma_0 I_n} \frac{1}{r} \right]^{\frac{1}{n+1}} \tilde{\varepsilon}_{ij}(\theta, n) \\
u_i &= \alpha\varepsilon_0 \left[ \frac{J}{\alpha\varepsilon_0\sigma_0 I_n} \frac{1}{r} \right]^{\frac{1}{n+1}} r^{\frac{1}{n+1}} \tilde{u}_i(\theta, n)
\end{aligned}
\qquad \text{(Eq.7)}
$$

Where n is the material hardening exponent in Ramberg-Osgood law.

One can see in the HRR-solution that the stresses, strains and displacements are proportional to the J value. Similar to the SIF K in LEFM, the J-integral quantifies the intensity at the crack tip field. Similarly, if the loading in the crack tip region reaches a material specific value, the crack initiation occurs. Since J-integral as a fracture criterion is based on the plastic deformation theory, the validity of J-integral is limited to the stationary cracks under monotonic loading [8]. Under these conditions a deviation from the strong proportionality has a minor effect on the path dependence of J-integral [8]. A distinguish must be made about J-integral in EPFM from in LEFM, for elastic material behaviour, linear or non-linear, the J-integral is identical with the energy release rate, as discussed before. However, in EPFM, the plastic strain energy is dissipated and cannot supply to the crack driving force, Therefore, this energetic interpretation and meaning of J are lost in EPFM [8].

With the help of numerous analytical and numerical calculations, formulas have been delivered to evaluate the elastic $J_{el}$ and plastic $J_{pl}$ part of J -integral as following

$$J = J_{el} + J_{pl} = \frac{K_I^2}{E'} + \frac{\eta}{B(w-a)}\int_0^{u_p} F du \qquad \text{(Eq.8)}$$

Where B, w, a represents the thickness, width of the fracture specimen and the crack size; $\eta$ is the correction function [8].

### 2.1.5.3 Crack Growth Resistance Curves

Most materials don't fail spontaneously at the critical resistance, but after crack initiation they build up a considerable resistance against further crack propagation[8]. For ductile crack propagation, an experimental crack growth resistance curves can be obtained, as Fig.5. The first part of the resistance curve ($J_R$-curve) corresponds to the crack tip blunting process and can be approximately described as a steep line, called the blunting line. With rising load the real physical crack initiation happens at $J_i$ by fracturing front of the blunted crack. This point is difficult to record during the measurements. After the crack initiation, the second part of the $J_R$-curve can be fitted by a power curve, according to the standard ASTM [40].

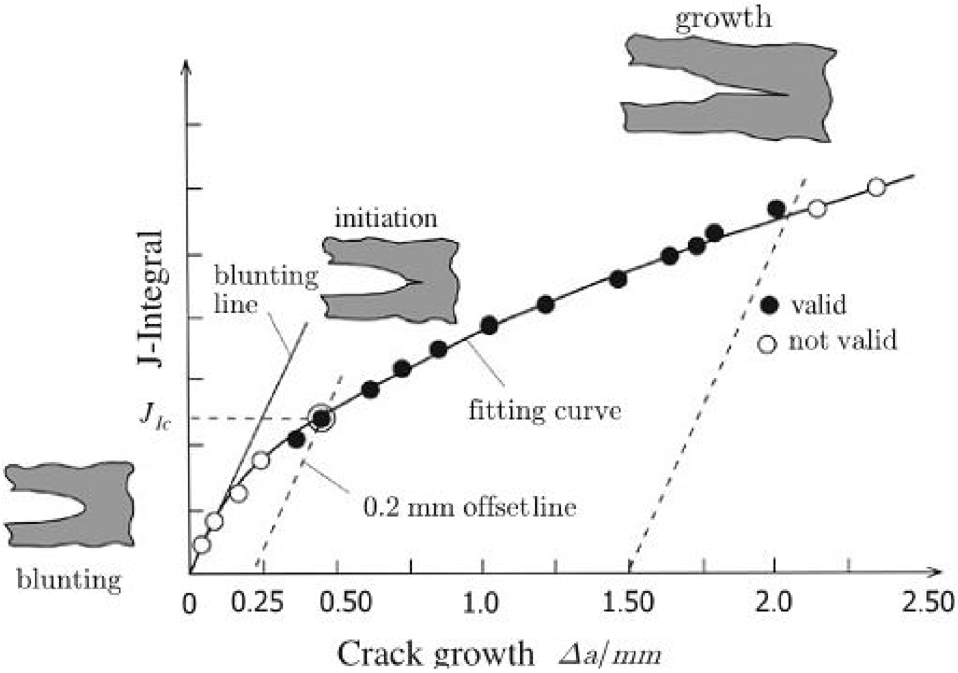

Figure 5 Sketch of the Ductile Crack Growth Resistance Curve [8]

The crack resistance curves reveal the material characteristics. However, it has been found that the $J_R$-curves is strongly affected by different geometry of the specimens (thickness, shape, initial crack size a/W etc.) [8]. It has been observed that for all specimens with the same material, the initiation value of $J_i$ is equal. But the curves afterward are significantly different, as shown in Fig. 6 [8]. Such influences can be incorporated into a stress state variable - stress triaxiality. The higher the triaxiality, the flatter are the resistance curves, meaning a facilitated process of ductile crack propagation [8].

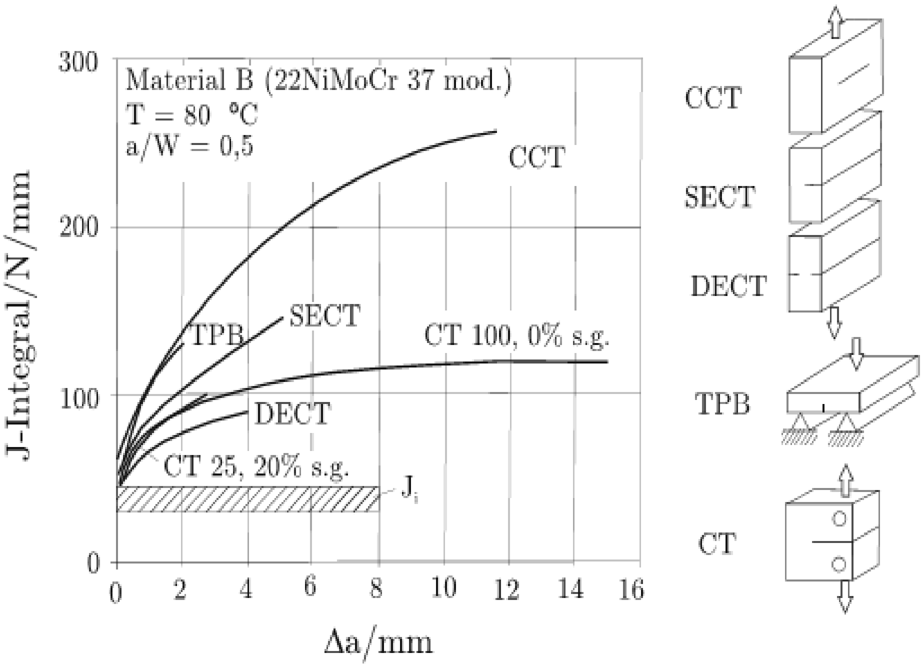

Figure 6 Crack Resistance Curves and Initiation Values Obtained by Various Specimen Geometries for Steel 22NiMoCr37 [8]

## 2.2 Fatigue

### 2.2.1 Fatigue Phenomena

The fatigue life usually covers a crack initiation period and a crack growth period. The initiation period is supposed to include some micro crack growth, often too small to be visible. In the crack growth period, the crack is growing until complete failure. It is technically significant to consider the crack initiation and crack growth periods separately because different factors are influencing each stage of fatigue crack growth. In the crack initiation period, fatigue is a material surface phenomenon as result of cyclic slip and is mainly governed by surface constraint and surface roughness [15]. As soon as the number of grains along the crack front becomes sufficiently large, crack growth occurs as a more or less continuous process along the entire crack front. The crack front can be approximated by a continuous line, which could have a semi-elliptical shape. How fast the crack will grow depends on the crack growth resistance of the material. Two important surface aspects are no longer relevant. Crack growth resistance when the crack penetrates into the material depends on the material as a bulk property and thus is no longer a surface problem [15].

### 2.2.2 Non-propagating/Propagating Cracks

Distinguish must made on different initial crack sizes when we discuss between the non-propagating cracks and propagating ones. On one hand, after some crack growth the crack tip stress field of these small cracks changes from plane stress at the free surface to plane strain deeper in the material. It implies an increased restraint on cyclic slip, and apparently crack arrest could occur as a consequence of insufficient cyclic slip. In this case, it is not really a material barrier that stops crack growth, but a change in the crack tip stress field. Such small cracks should be referred to as mechanically short cracks [15]. On the other hand, when the significance of material structural barriers is associated with their effect on cyclic slip at the tip of micro-crack, such cracks are referred to as micro-structurally small cracks[42], as observed in Fig. 7.

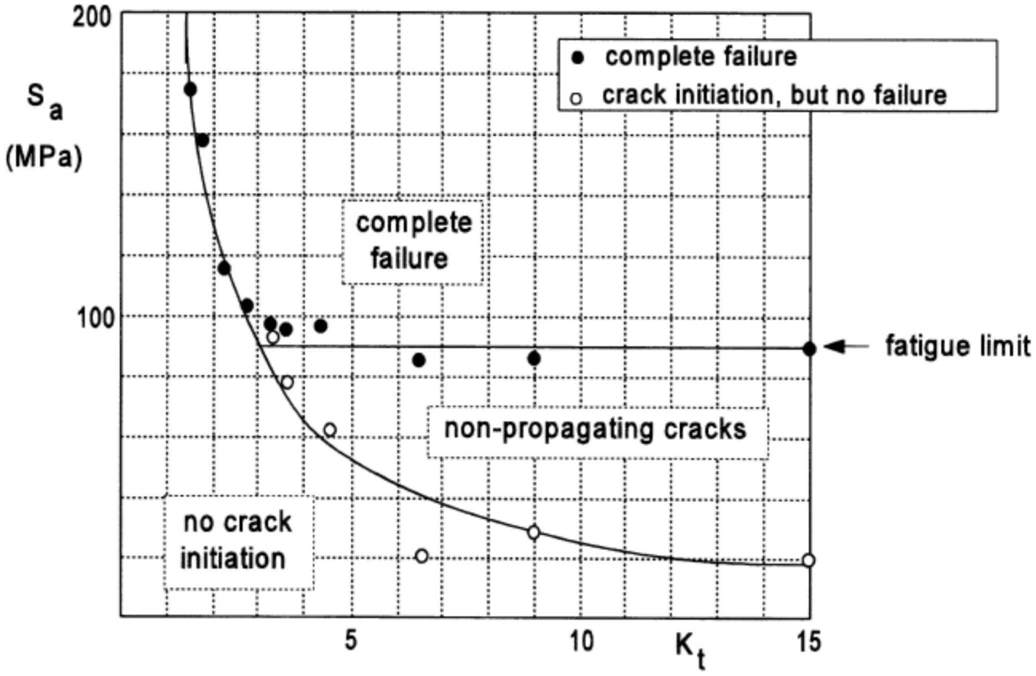

Figure 7 Observations of Frost [42] on Non-propagating Cracks as a Function of Kt .Material: Mild Steel.

The scope of this project would be focusing on the propagating cracks, the growth of which is then depending of the crack growth resistance of the material as a bulk property, referred to a crack growth of macro crack, i.e. the load spectrum should contain stress cycles above the fatigue limit.

### 2.2.3 Fatigue Crack Growth Law

The fatigue crack growth results from experiments are frequently plotted with the crack growth rate as a function of the range of K-values on a double log scale, as shown in Fig.8. One can see that two vertical asymptotes occur in a da/dN-ΔK graph,.

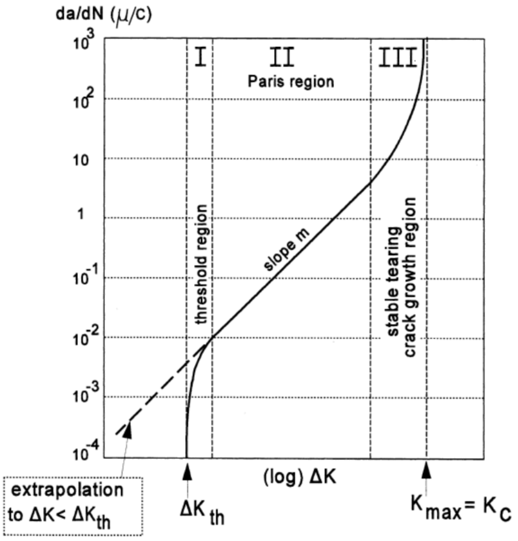

Figure 8 Three Regions of the Crack Growth Rate as a Function of ΔK[15]

The left asymptote at $\Delta K = \Delta K_{th}$ indicates a threshold ΔK-value which is too low to cause crack growth. The right asymptote occurs for a ΔK cycle with $K_{max} = K_c$. It means that $K_{max}$ reaches a critical value which leads to complete failure of the specimen[15]. Respectively, the function da/dN = f (ΔK) is supposed to cover three different parts, indicated by I, II and III. The corresponding regions are referred to as: (i) the threshold ΔK-region, (ii) the Paris-ΔK-region, and (iii) the stable tearing crack growth region. In region II, Paris et al. observed similar the crack growth rate based on the SIF, which led to the application of the Paris Law according to the similarity principle [43].
According to Paris (1963) [44], the relation between da/dN and K can be formulated by a power function.

$$\frac{da}{dN} = C(\Delta K)^m$$

(Eq.9)

With C and the exponent m as material parameters. Paris model doesn't account for the influence of the stress ratio R, either for the region II and III. In 1967, Forman [45] introduced a model accounting for the effect of R and the case when Kmax in a cycle it close to Kc

$$\frac{da}{dN} = \frac{C(\Delta K)^m}{(1-R)(K_c - K_{\max})}$$

(Eq.10)

Later on in 1976, Priddle[46] proposed a model to consider the both two asymptotic conditions as,

$$\frac{da}{dN} = C\left(\frac{\Delta K - \Delta K_{th}}{K_c - K_{\max}}\right)^m$$

(Eq.11)

## 2.3 Approaches

### 2.3.1 Fracture Mechanical Approaches

The application of fracture mechanics in (fatigue) crack propagation provides principles or criteria that indicate:

1. the criteria for crack initiation or crack extension. For instance, the threshold value of Kc or Ji mentioned in Section 2.2 for monotonic loading, or in case of fatigue loading, a loading condition above the fatigue threshold value $\Delta K_{th}$ would initiate crack growth.
2. the direction of crack propagation. Different criteria for crack propagation direction are discussed in [8] and tested in [34]. In the present study, the fatigue crack growth can be easily assumed to occur perpendicularly to the global-Mode-I tensile loading.
3. the amount of crack growth. In case of fatigue problem, the application of Paris law or other modified fatigue crack propagation law is frequently adopted, e.g. in [30]

In numerical simulation, crack extension implies new crack faces which require updating boundary values. All these above principles need to be incorporated into the finite element model by appropriate algorithms. This procedure in principle models crack propagation as a temporal sequence of Boundary Value Problem (BVP) with discrete, growing crack lengths $a_i$, and a material separation along the crack increment $\Delta a_i$ is assumed as discontinuous[8]. Typical techniques are not discussed specifically here but can be found in [8] including node release technique, element modification (splitting, elimination, adaptive stiffness etc.), remeshing techniques and so on.

### 2.3.2 Damage Mechanical Model

Damage mechanical model were developed very intensively and successfully for the simulation of ductile crack propagation in metallic materials in the last two decades [8]. The global FE model prescribes the loading conditions that the component is under onto the damage zone [16], i.e. dealing with the damage events in the crack process zone. There are mainly two groups of damage models that are most commonly used: Models based on micromechanical processes of damage and phenomenological models [8]. The former is not considered in the present study due to the scope of the project. The latter, phenomenological models do not depend on a specific failure mechanism and can therefore be used for arbitrary damage [8]. The cohesive zone model (CZM), which the author will be apply in his present study, can be attributed by its nature to phenomenological models and will be discussed in detail in the next section.

## 2.4 Cohesive Zone Modelling

### 2.4.1 Development

The cohesive zone model can be traced back to the Dugdale yield strip model in 1960 [5], as mentioned in section 2.1.5. The magnitude of the traction on the crack faces in the plastic zone is equal to the yield strength of an elastic-ideally plastic material, see Fig. 9. Since the stresses at the crack tip are limited up to the yield strength, the unrealistic singularities in fracture mechanics are removed, which is another favoured property of CZM over the conventional fracture mechanical approach. The cohesive zone model in its present form starts from the work of Barrenblatt [6], who replaced the yield strength with a cohesive law to simulate the decohesion of atomic lattices, see Fig 10.

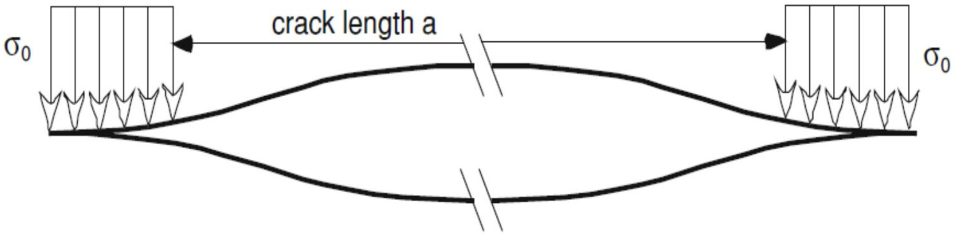

Figure 9 Yield Strip Model by Dugdale [16]

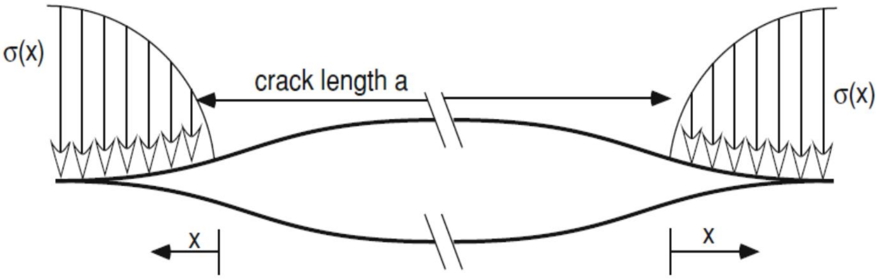

Figure 10 Barrenblatt Model, the Traction is a Function of Distance Ahead of Crack Tip x [16]

Material degradation and separation are concentrated in a discrete plane, represented by cohesive elements which are embedded in the continuum elements representing the test piece or structural component [16]. The first application of cohesive zone model was conducted by Hillerborg et al for fracture behaviour in concrete in 1976[47]. The first analysis of micro damage in ductile material was performed by Needleman in 1987 and the first macroscopic crack extension in ductile materials was analysed by Tvergaard and Hutchinson [16].

In recent two decades, cohesive zone model has also been adapted for fatigue simulations, sometimes also referred to as the cyclic cohesive zone model [2]. With introduced damage accumulation model, this method has been successfully employed to predict fatigue crack growth in metals [4, 13, 32], composite materials [3], fibre-metal laminate [31], weld specimen[2], and so on.

### 2.4.2 Traction-Separation Law

As mentioned before, the crack tip processes during crack propagation, can be replaced by a narrow-banded area, consisting of two fictitious surfaces that collapse on each other in un-deformed situation. Application of external loading can result in the separations of the two surfaces, i.e. displacement jumps. The behavior of the material separation under external loading can be described by a constitutive relationship between the tractions and displacement jumps, and such relationship is referred to as the Traction-Separation Law (TSL). The CZM employs a material model represented by a TSL describing the loss of load bearing capacity of the material as a function of a separation, irrespective of the physical details of damage occurring in an actual material [16]. Thus, it can be applied to both ductile and brittle damage and failure processes. It is noted that cohesive models here do not describe material deformation but only separation [16].

In literature, quite a number of TSLs can be found. Some typical examples are given in Fig.11 .

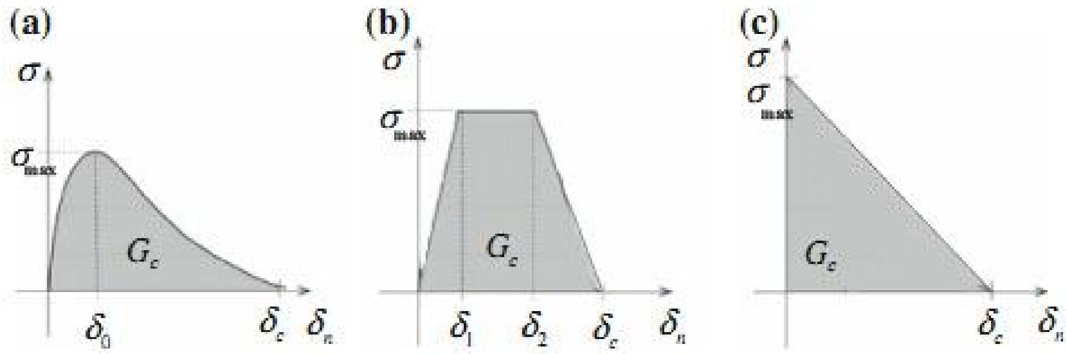

Figure 11 Typical TSLs

All these TSLs suggest in common that the crack extends when the separation reaches a critical value of $\delta_c$, illustrated in Fig.12. The maximum traction is the other material parameter (also model parameter) called cohesive strength $\sigma_{\max}$ . In detail, three models are discussed further in the following.

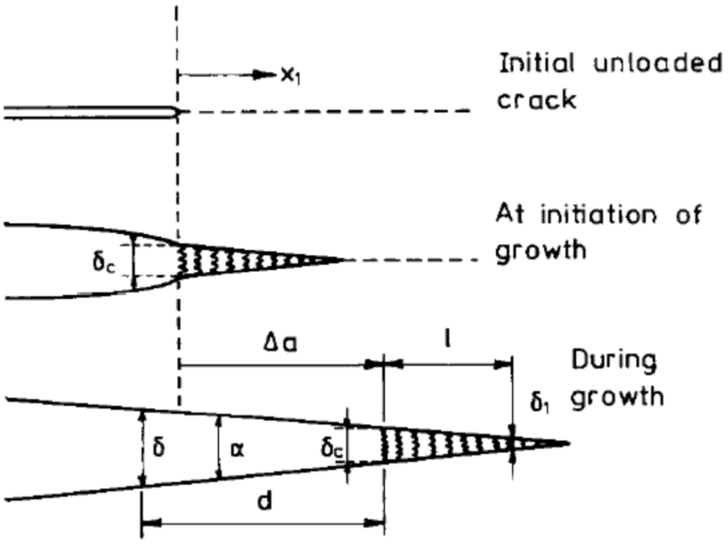

Figure 12 Schematization of Crack Extension [39]

1. The model as schemed in Fig. 12 (c) is proposed by Hillerborg for brittle fracture in concrete [47]. The infinite initial stiffness can be easily understood for pure brittle materials. No separation occurs before the traction reaches the cohesive strength, which means all the inelastic deformation can be assumed to be material separation[16]. Afterward, the traction on the interfaces decays linearly or bi-linearly.

2. Models such as Fig.11(a.b) are usually applied for ductile materials[16]. Referring to Fig(a), a potential based model proposed by Needleman[7] is given as:

$$\mathrm{T_n} = \sigma_{\max} e \exp\left(-\frac{\Delta_n}{\delta_0}\right)\left\{\frac{\Delta_n}{\delta_0}\exp\left(-\frac{\Delta_t^{\,2}}{\delta_0^{\,2}}\right)+(1.0-q)\frac{\Delta_n}{\delta_0}\left[1.0-\exp\left(-\frac{\Delta_t^{\,2}}{\delta_0^{\,2}}\right)\right]\right\}$$

$$\mathrm{T_t} = 2\sigma_{\max} eq\frac{\Delta_t}{\delta_0}\left(1.0+\frac{\Delta_n}{\delta_0}\right)\exp\left(-\frac{\Delta_n}{\delta_0}\right)\exp\left(-\frac{\Delta_t^{\,2}}{\delta_0^{\,2}}\right)$$

$$\Gamma_n = \sigma_{\max} e\delta_0, \quad \Gamma_t = \sqrt{\frac{e}{2}}\tau_{\max}\delta_0$$

$$\tau_{\max} = \sqrt{2eq}\,\sigma_{\max}, \quad q = \frac{\Gamma_t}{\Gamma_n} \qquad \text{(Eq.12)}$$

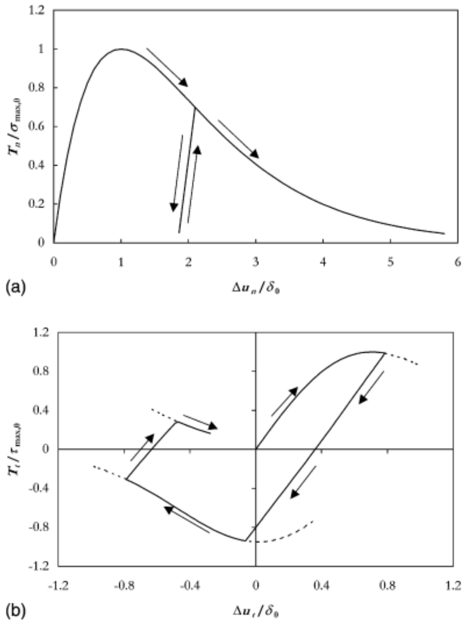

**Figure 13 Schematization of TSL proposed by Needleman: (a) in Normal direction (b) in Tangential Direction [31]**

One can see that the traction increases initially in a finite slope with increasing separation up to the cohesive strength $\sigma_{\max}$ , and the corresponding normal separation is designated as a characteristic value $\delta_0$. While the separation exceeds $\delta_0$, the traction decreases exponentially approaching a horizontal asymptotic with zero traction at infinity. In this case, the critical separation is defined in a manner that the work done between separation $\Delta_n = 0$ and $\Delta_n = \delta_c$ equals to $0.95\Gamma_n$ [7], the characteristic separation corresponds to the separation when the traction reaches at the cohesive strength. The relationship between $\delta_0$ and $\delta_c$ reads [7]: $\delta_c = 16e/9\delta_0 \approx 4.8325\delta_0, e = \exp(1)$

3. Hutchinson introduced a TSL with trapezoidal shape depicted as Fig.11 (b) [39], where $\Gamma_n = \frac{1}{2}\sigma_{\max}(\delta_c + \delta_2 - \delta_1)$; and $\delta_1 / \delta_c = 0.15$, $\delta_2 / \delta_c = 0.5$ is suggested and is of minor influence on the cohesive behaviour according to [39]. Material hardening behaviour can also influence the cohesive parameters.

Description about other TSLs such as those proposed by Bazant, Scheider, etc.[16] can be found in literature. In general, the choice of TSL shape depends on the fracture behavior of material (brittle or ductile).

### 2.4.3 Cohesive parameters

For different TSL shapes, the cohesive parameters need to be determined individually, known as shape dependence, suggested by I. Scheider et al [21]. Commonly, given a specific shape of TSL, the two material parameters mentioned above are sufficient to define the cohesive behaviour: cohesive strength $\sigma_{\max}$ , critical separation $\delta_c$ . However, it has been proven more practical to use, without increasing the number of independent variables, another related material parameter $\Gamma_n$ [16], the cohesive energy defined as the area under the TSL curve.

According to [8], the cohesive energy, representing the energy supplied for crack surface separation, can be evaluated by the J-integral at the crack tip. One can immediately recognise this relation in LEFM. Within the framework of EPFM, the separation energy correlates with the physical initiation value $\Gamma_n = G_c \approx J_i$ , provided that the J-integral is sufficiently path independent [8]. Thus, the relationship is established between classical fracture mechanics and cohesive zone model.

The cohesive parameters can be determined from experiments as rough estimation and optimised from numerical simulation. Guideline for initially estimated values for structural steel is given in [16]. For a given TSL shape, the cohesive parameters can be determined as stress-state-dependent variables and thus the transferability problem is solved automatically, otherwise the cohesive parameters should be determined from conditions with similar triaxiality [24]. Cohesive zone model in plane stress condition may encounter thickness sensitivity problem [23, 26] but is not considered here for simplicity.

### 2.4.4 Cohesive zone model in fatigue crack growth simulation

CZM regards the fatigue crack process as a result of progressive material deterioration, and are sometimes called cyclic cohesive zone model. To apply cohesive zone model to simulate crack growth under fatigue loading, two additional characteristics of the cohesive behaviour must be taken into account:

1. Unloading Algorithm

This must be implemented in the traction–separation law to account for the reduction of separation and traction on the interfaces.

In general two alternatives for the unloading situation is considered. As shown in Fig. 14. Distinguishes can be made for differences of material behaviour during unloading. Fig.13 (a) shows a unloading situation where the cracks close completely when no loads acting on the crack faces, which is suggested for brittle facture [16]; in contrast Fig.13 (b) suggests a remaining separation, which represents ductile fracture [16]. But the difference between these two unloading algorithms and its impacts on the crack propagation have not been thoroughly studied in literature yet and is considered of minor importance in general practice given the fact of the CZM being a phenomenological model [10], as one may find that these two unloading algorithms are frequently not distinguished specifically for different types of materials.

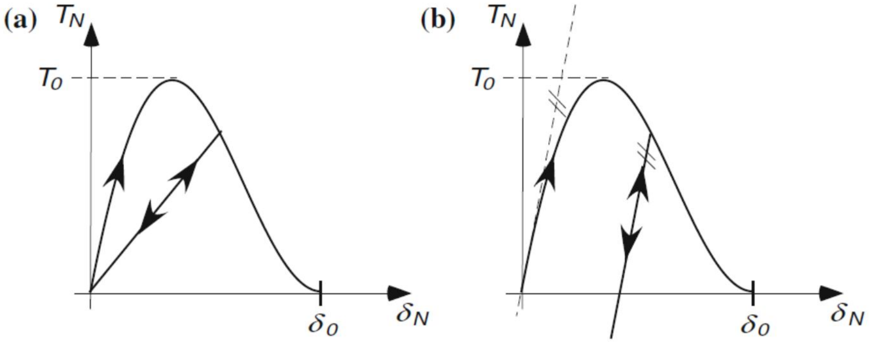

Figure 14 Unloading Algorithms[16]

2. Damage Accumulation

If the load history contains identical cycles and unloading/reloading is equal, which is commonly simulated, saturation occurs easily during cyclic loading and material degradation does not increase anymore[16]. The saturation problem will be proved in Section 5.1 in the following.

One solution is to define different unloading/reloading paths, where unloading is usually set to occur linearly and reloading follows a quadratic equation, as shown in Fig. 15

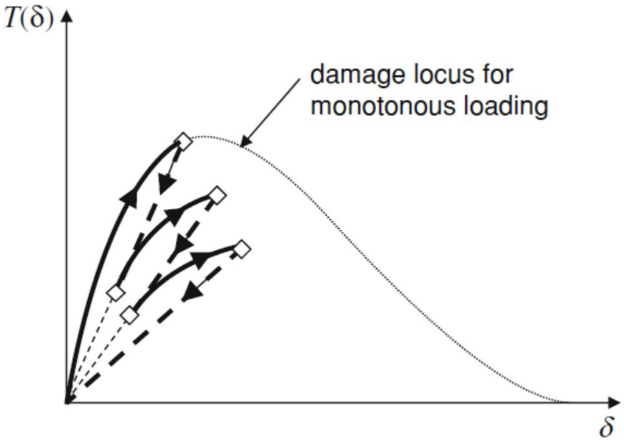

Figure 15 Cyclic Cohesive Zone Model with Different Paths for Unloading and Reloading [16]

Another solution for the saturation problem is by introducing a damage variable, that accumulates over the load cycles and by which the cohesive strength is degraded. With appropriate setting of model parameters to the damage evolution model, cyclic CZM is able to reproduce the classical curves of Paris Law[4]. One typical example could be the work by Roe and Siegmund (2003) [10], who suggested a damage model under the assumptions of the typical damage evolution laws (Lamaitre J., 1996) [11] and applied it successfully to a thermoplastic adhesive. Later on, Silitonga S. et al(2014) [13] modified this damage evolution model by introducing a concept of cohesive energy dissipation to simulate the FCG in Aluminium alloy.

## 3.0 CRACK PROPAGATION UNDER MONOTONIC STATIC LOADING USING ABAQUS STANDARD COHESIVE ELEMENT

## 3.1 Patch test under Mode 1 loading

### 3.1.1 Model Establishment

ABAQUS 6.10 provides a special cohesive element with response based on traction (stress) and separation (displacement jump). In order to study the Traction-Separation Law, simple Mode 1 problem is studied here. In the patch model, a square plate (1mm*1mm) is loaded at the top edge under displacement control and attached the bottom edge to the cohesive zone representing the crack process zone. The model is discretized into of a single cohesive element COH2D4 and a single continuum plane stress element CPS4R with elastic material property of Young's modulus E=210Gpa and the Poisson's ratio v=0.3. As depicted in Fig. 16, the boundary conditions are applied at the bottom edge of the cohesive element with displacement constraints in two directions.

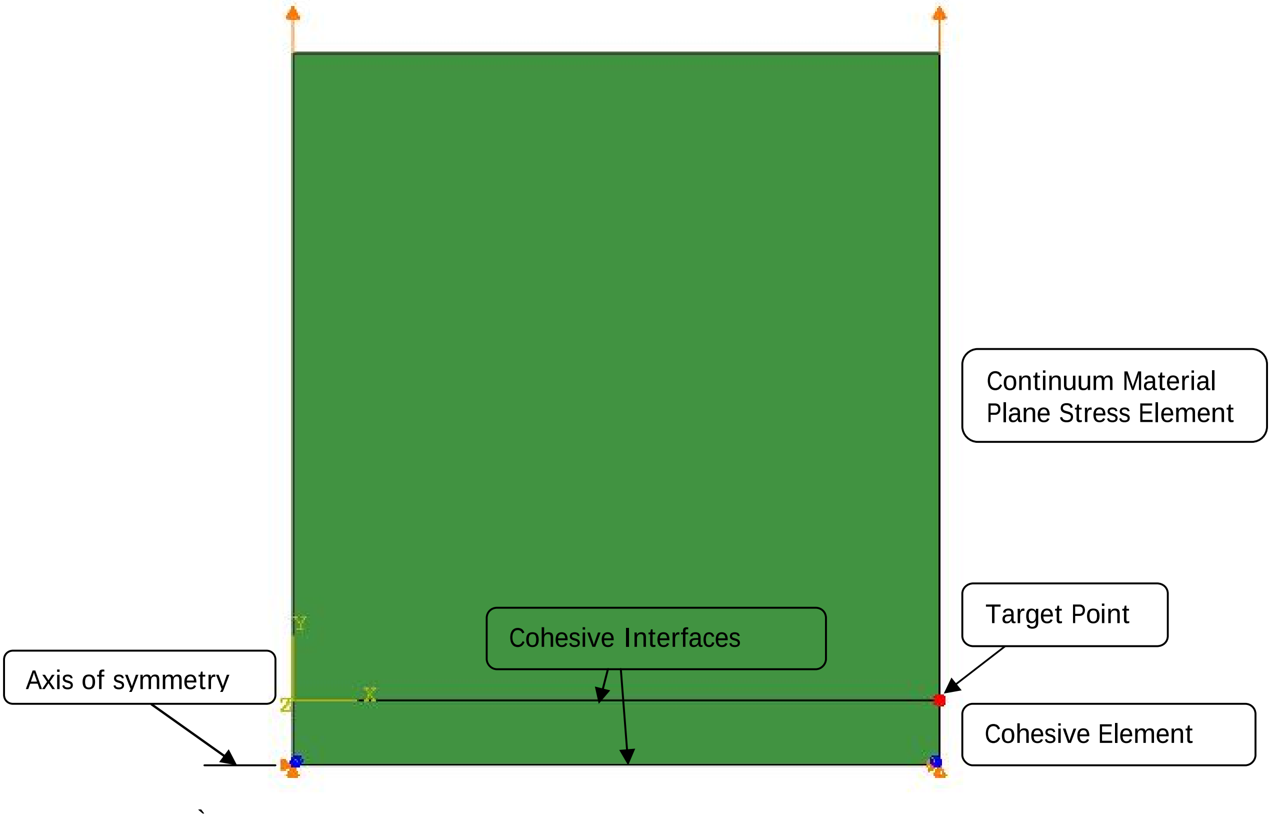

Figure 16 Patch Test Model

This model is also applied later in Section 4 and Section 5 to justify the implemented TSL. Changes to the model will be specified separately if applicable.

### 3.1.2 Verification of Traction-Separation Law in ABAQUS

The available TSL in ABAQUS assumes initially linear elastic behaviour followed by the initiation and evolution of damage. The elastic behaviour is written in terms of a linear elastic constitutive matrix that relates the nominal stresses to the nominal strains across the interface [41]. By specifying the value of constitutive thickness the elastic behaviour of the cohesive layer is related back to the continuum material as bulk material property. If no exceptions are made, the initial elastic response of the cohesive element is kept as: E=210Gpa, constitutive thickness is 1.0mm. Once a damage initiation criterion is met, material damage can occur according to a certain damage evolution law. To make it more comparable to different TSL mentioned in Section 2.4.2, the damage initiation criteria is set as maximum nominal stress $\sigma_{\max} = 1329 Mpa$ and the critical separation is set as 0.6mm. A linear damage evolution law that describes linear softening behaviour studied here as schematised in Fig.17.

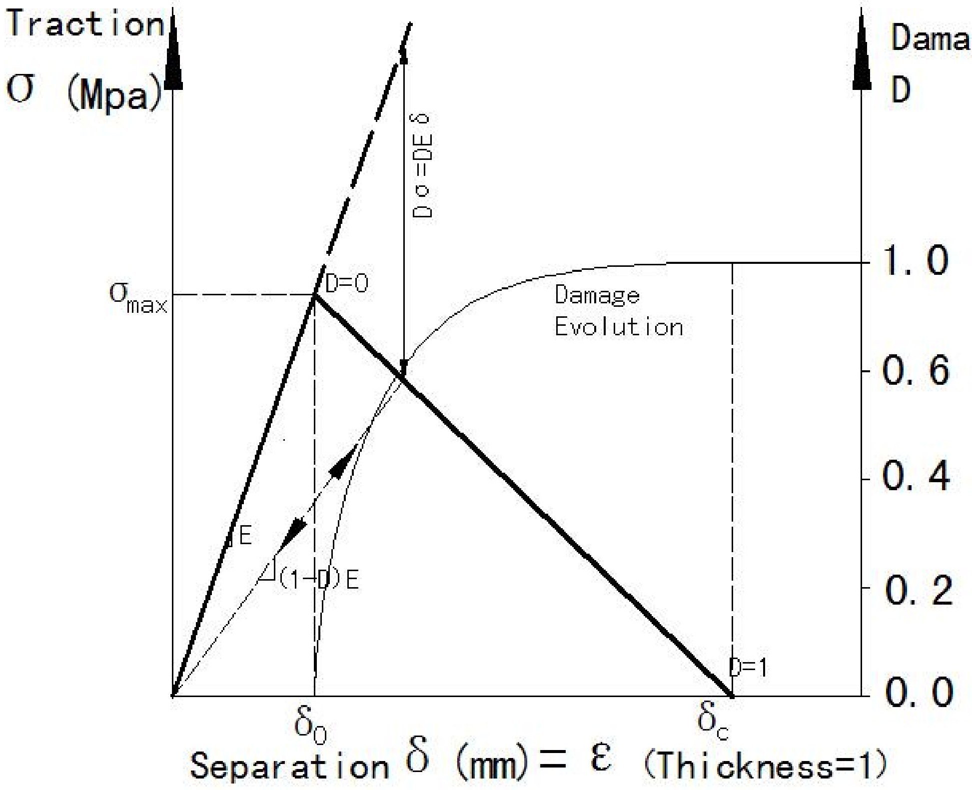

Figure 17 Schematisation of TSL with Linear Softening

If the damage initiation criterion is specified without a corresponding damage evolution model, no damage will occur and the cohesive element will maintain its load bearing capacity, i.e.no crack propagation. In our study, the criterion for damage initiation is chosen as the maximum traction, referred to as the cohesive strength. In ABAQUS, once the corresponding initiation criterion is reached, the damage evolution law describes the rate at which the material stiffness is degraded [41]. In Section 3, all the analysis applied a triangle-shaped TSL. The linear softening is formulated by the damage evolution in the manner of [41],

$$D_c = \frac{\delta_c(\delta_n - \delta_0)}{\delta_n(\delta_c - \delta_0)}$$

A schematization of the damage evolution model can be found in Fig.17. The physical background of damage evolution in metals consists of initiation, growth and coalescence of voids. To include such a mechanical behaviour in a macroscopic sense, the concept of Continuum Damage Mechanics has been developed [1]. As an essential part of a continuum damage formulation, the damage evolution law is used to calculate the amount of damage during the deformation process. The damage evolves from 0 (no damage) to 1 (fully damaged material) as a function of separation (or strain when a constitutive thickness is defined as 1 as the case here in the project.)

As depicted in Fig.18, the TSL implement with and without linear damage evolution model is verified in the patch model. The target point where the data is obtained is located at the upper face of the cohesive element, the red node as shown in Fig.16. The nodal displacement in the plot has been doubled due to axisymmetry.

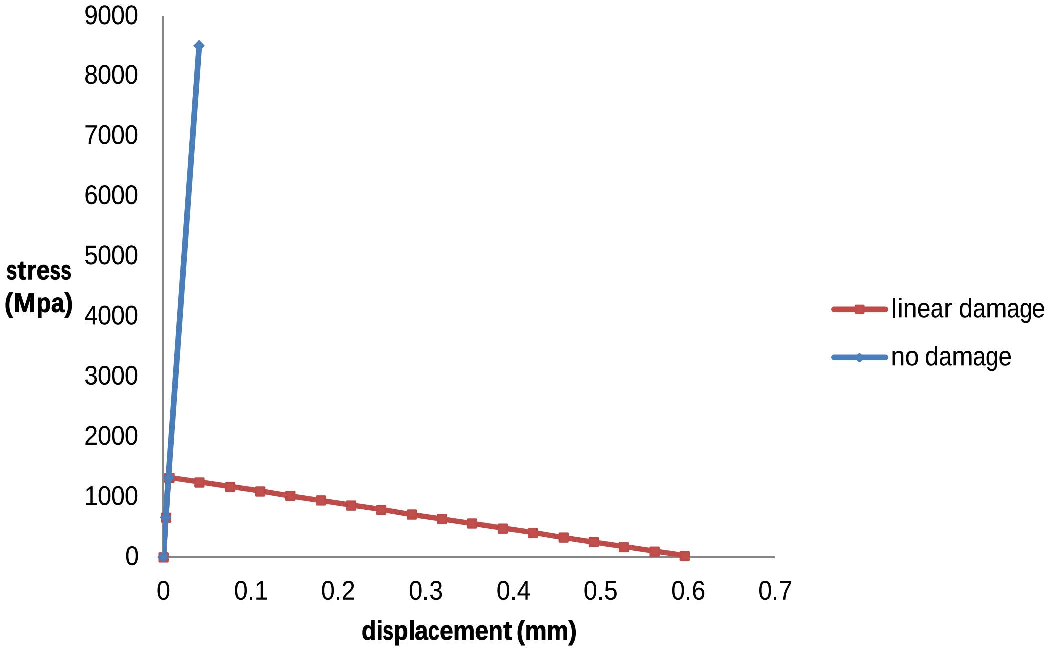

Figure 18 Verified TSL with and without Damage Evolution

In addition, the author tried different settings of incremental size during the analysis. Due to the softening behaviour of the TSL, it is common that the criteria for convergence cannot be reached and the analysis gets aborted with errors. The following recommendations are concluded to improve the convergence problem.

1. Increasing the number of steps doesn't helps with the convergence;
2. Automatic incremental size is always suggested;
3. Smaller initial incremental size is helpful in convergence and in obtaining more accurate result.

### 3.1.3 Symmetry Test

Since all the problems from this project focus on Mode 1 fracture under global tensile loading. The property of symmetry is utilised to improve the analysis efficiency and to reduce the calculation time. This means that the model inputs for the cohesive layer which coincides with the symmetry axis should be modified, so that half of the separation corresponds to the magnitude of the traction at the un-halved level of separation according to the original TSL implemented. Please note that the separation considered here is the one in the normal direction which lies perpendicular to the cohesive interfaces. Meanwhile the influence on the shear separation is considered negligibly small. To justify this, the author has built another model as shown in Fig. 19.

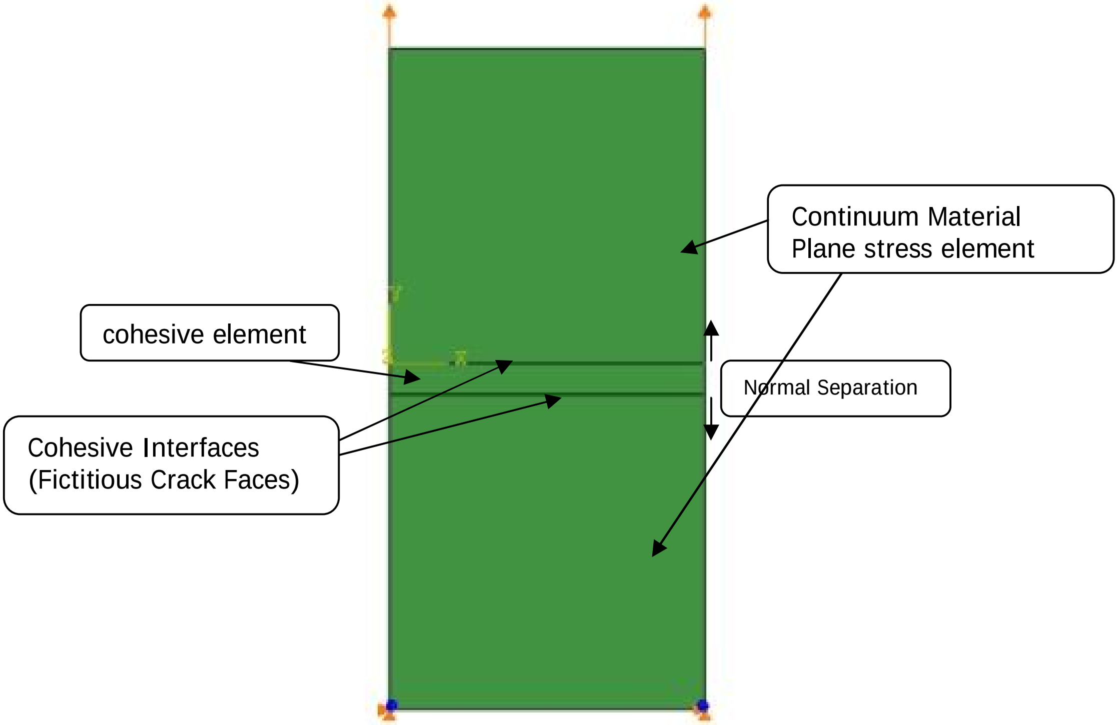

Figure 19 Complete Model for Symmetry Test

The modified TSL is verified as intended in Fig. 20 and the global load-displacement response at the loaded edge satisfies the expectation in Fig. 21

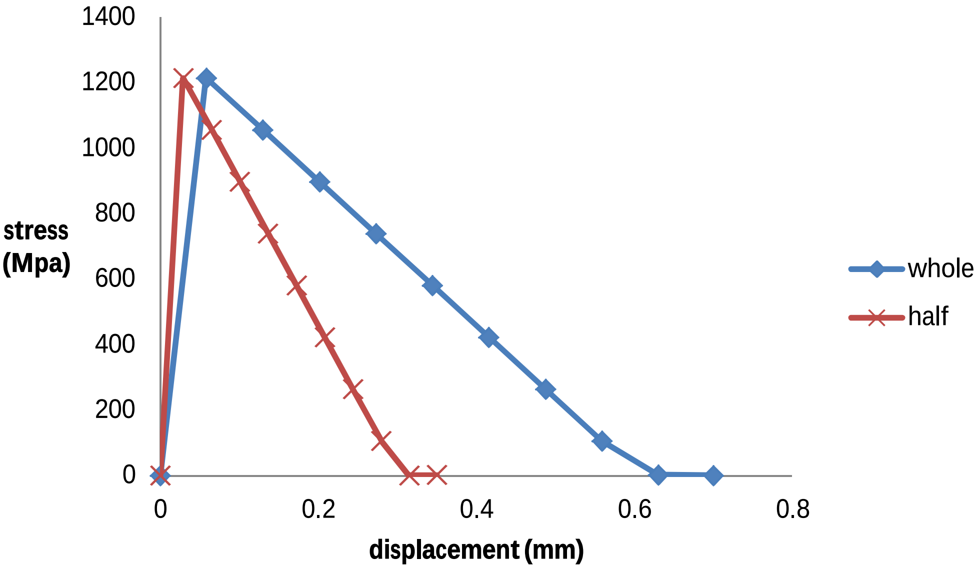

Figure 20 Reproduced TSL Implemented in the Whole and Half Model Respectively

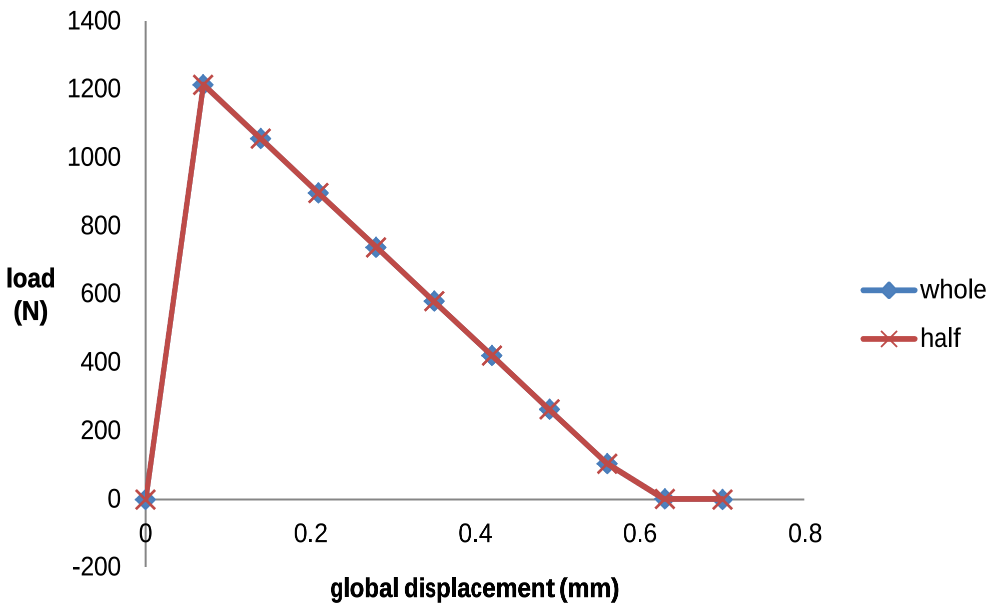

Figure 21 Global Load-Displacement of the Whole and Half model

## 3.2 Study on the Cohesive Parameters

### 3.2.1 SENT Specimen Model

To study the influences of the cohesive parameters, a Single Edge Notched Tension (SENT) specimen is introduced. The geometry of the specimen follows the specifications in [18], with length*width=25mm*10mm. The aspect ratio (the ratio between the initial crack length and the specimen width) is 0.5. As shown in Fig.22, the shadowed part of the real specimen is analysed in the simulation.

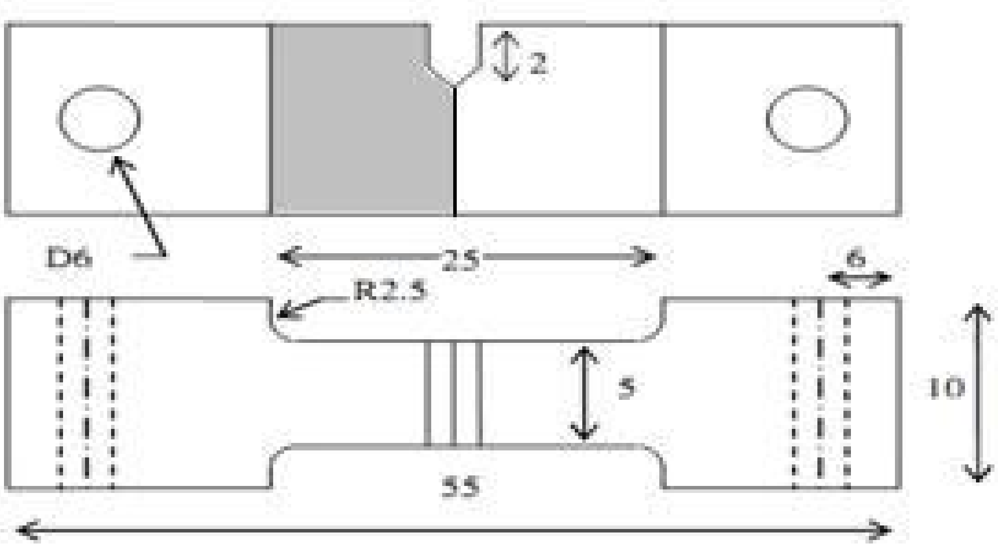

Figure 22 Figuration of the SENT Fracture Specimen [18]

The thickness of the specimen is 5mm, which is considered a too small value to satisfy the plane strain condition according to [40], thus a 2D plane stress model is established.

According to [16], the recommended element size for fine mesh of approximately $50-100\mu m$ is considered sufficient. In our study the smallest element size at the refinery region is $20\mu m$ if no exceptions are specified. Meanwhile, the fine mesh zone length should exceed the crack length needed to reach the steady state [39]. According to [18] the crack extension length ranges from 0.6 to 1.4 mm. So the fine mesh zone length of 3mm is chosen here. The thickness of the cohesive layer is $1\mu m$ and considered small enough compared to the geometry of the whole model. Half of the specimen is modelled due to symmetry condition in Mode 1 tensile loading. The final meshed model is shown in Fig. 23 and the details around crack process zone is zoomed in as in Fig. 24

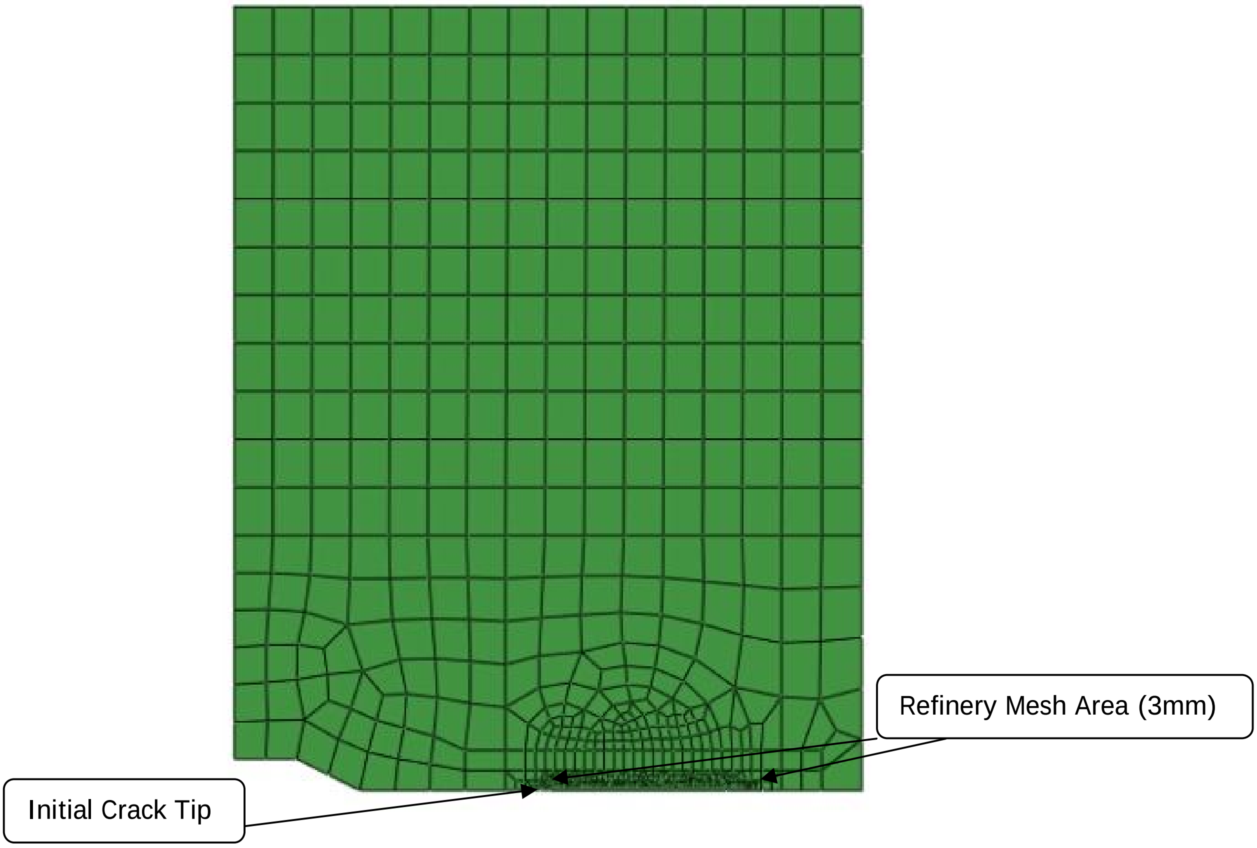

Figure 23 Model of the Fracture Specimen Established for Analysis

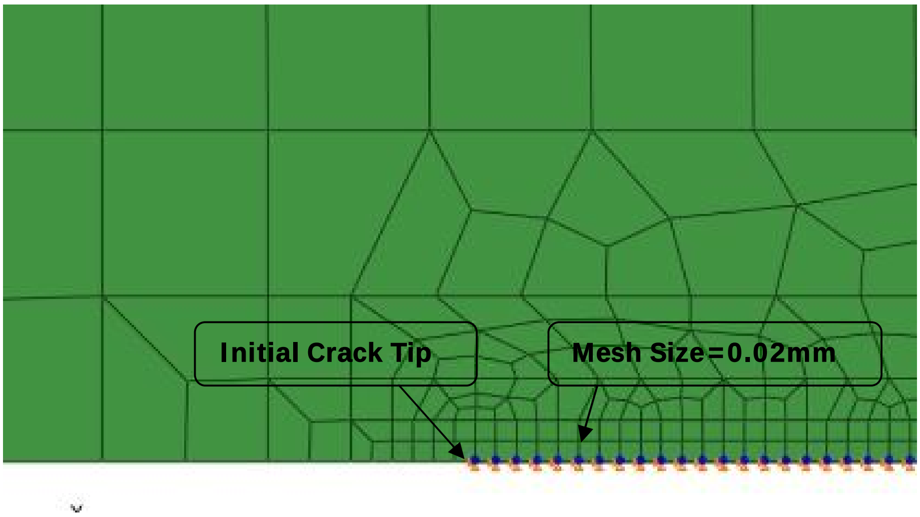

Figure 24 Mesh in Detail around the Cohesive Zone

### 3.2.2 Material Properties

The elastic-plastic property of the continuum material (pipeline steel X65) is taken from the experimental data obtained by the company Allseas. The 0.2% yield strength is $\sigma_y = 443Mpa$ .Elastic modulus is 207Gpa, the Poisson's ratio is 0.3. In this project, all the analysis is conducted in static load steps, the time/rate dependency of the material is not considered.

According to the suggestions in [16], for structural steel, the rough estimation for the cohesive energy and the cohesive strength is given respectively as

$$\begin{aligned}&\Gamma_n = G_{Ic} = \frac{K_{Ic}^2}{E'} = \frac{\left(280\sqrt{Mpa \cdot m}\right)^2}{207000Mpa} = 378.7\ N/mm,\\ &\sigma_{\max} = 3\sigma_y = 3*443 = 1329Mpa \qquad .\\ &with\ E' = \begin{cases} E\ in\ plane\ stress \\ \dfrac{E}{1-\upsilon^2}\ in\ plane\ strain \end{cases}\end{aligned} \qquad \text{(Eq.13)}$$

The value of $K_{IC}$ as an rough estimation is obtained from [17] as $K_{IC} = 280\sqrt{Mpa*m}$ . ABAQUS requires specifying the critical separation $\delta_c$ to identify the failure of the cohesive element. As introduced in Section 2.4.2, the value of $\delta_c$ is determined from the area under the TSL curve which is in a triangle shape.

$$\delta_c = \frac{2*\Gamma_n}{\sigma_{\max}} = \frac{2*378.7}{1329} = 0.5699mm$$

### 3.2.2 Methodologies

The influences of the cohesive parameters are analysed through a series of parametric studies divided into groups of cases. All the cases that have applied different combination of parameters are included in Table 1..

**Table 1 Cases for analysis in parametric study**

| | $100\%\Gamma_n$ | $50\%\Gamma_n$ | $25\%\Gamma_n$ | $12.5\%\Gamma_n$ | $6.25\%\Gamma_n$ | $3.125\%\Gamma_n$ |
|---|---|---|---|---|---|---|
| $\sigma_{\max}=3\cdot\sigma_y$ <br> $=1329M\text{pa}$ | Case 1<br>207-<br>0.5699 | Case 2-1<br>207-<br>0.2850 | Case 2-2<br>207-<br>0.1425 | | | |
| $\sigma_{\max}=1.5\cdot\sigma_y$ <br> $=664.5M\text{pa}$ | | Case 2-3<br>207-<br>0.5699 | Case 2-4<br>207-<br>0.2850 | Case 2-5<br>207-<br>0.1425 | Case 2-6<br>207-<br>0.0713<br>Case 2-7$^*$<br>103.5-<br>0.0713 | Case 2-10<br>207-<br>0.0356 |
| $\sigma_{\max}=1\cdot\sigma_y$ <br> $=443M\text{pa}$ | | Case 2-9<br>207-<br>0.428 | Case 2-8<br>207-<br>0.2140 | | | |

* Case 2-7 adopts the same values as Case 2-6 does for the cohesive strength and cohesive energy but varies with a halved initial stiffness, the TSL of which is schematized in Fig.25 .

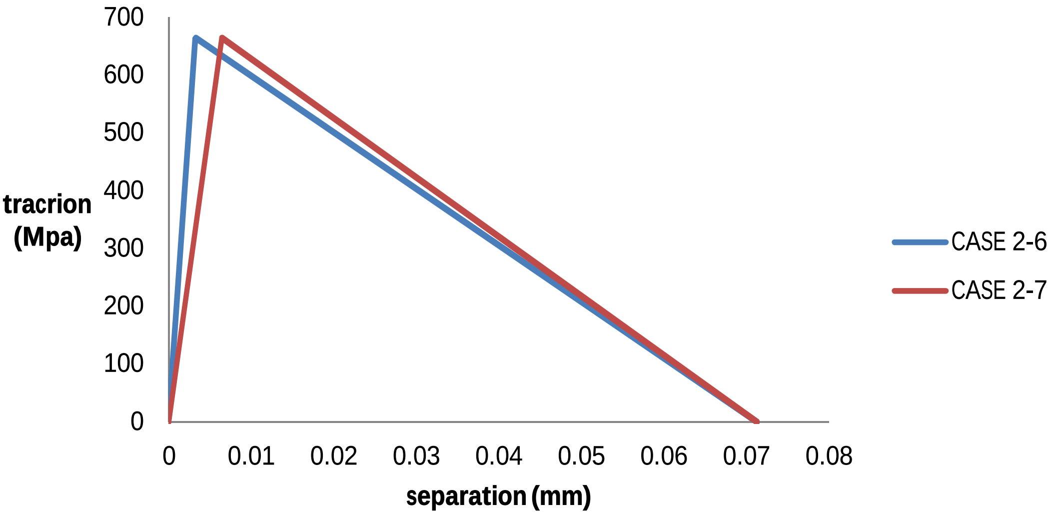

Figure 25 TSL Implemented for Case 2-6 (stiffness 207 Gpa) and 2-7 (Stiffness 103.5 Gpa)

As one can see in the table, the two major parameters for check are: 1) the cohesive strength which varies from $3\cdot\sigma_y$ to $1\cdot\sigma_y$; 2) the cohesive energy, the variation of which is realised by the adjustment on the critical separation. Since the number of the cases is large, the author has numbered all the cases with different marks, and the following numbers are the initial elastic stiffness (in Gpa) and the critical separation (in mm). The external load is applied on the top edge of the specimen under displacement control to elongate the specimen up to 0.3 mm, as shown in Fig.26. The geometrical nonlinearity is activated during the analysis for every case.

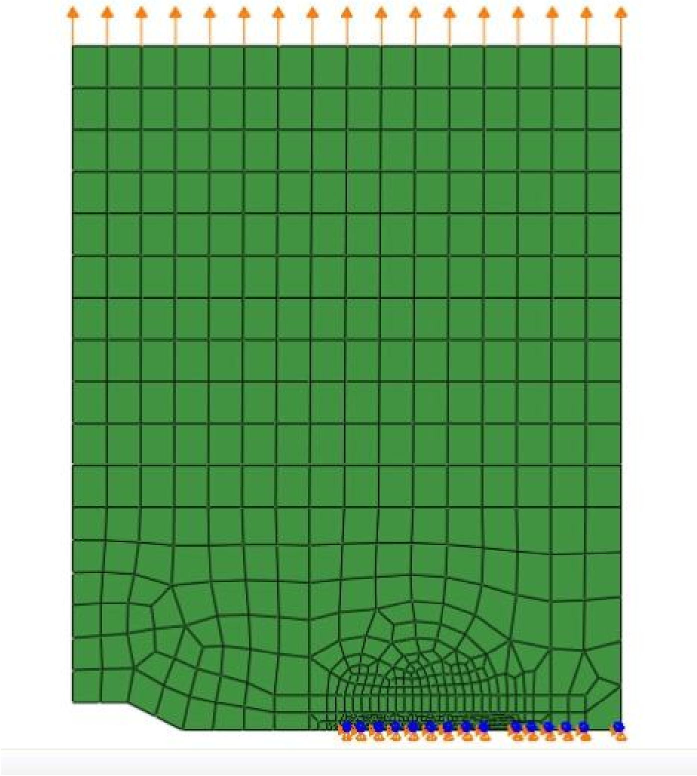

Figure 26 Boundary Conditions of the Model

### 3.2.3 Results

#### 3.2.3.1 Influences of the Cohesive Strength

A $\sigma_{\max} = 3 \cdot \sigma_y$

When the cohesive strength equals to $3 \cdot \sigma_y$, there is no crack initiation observed regardless of value of cohesive energy used.

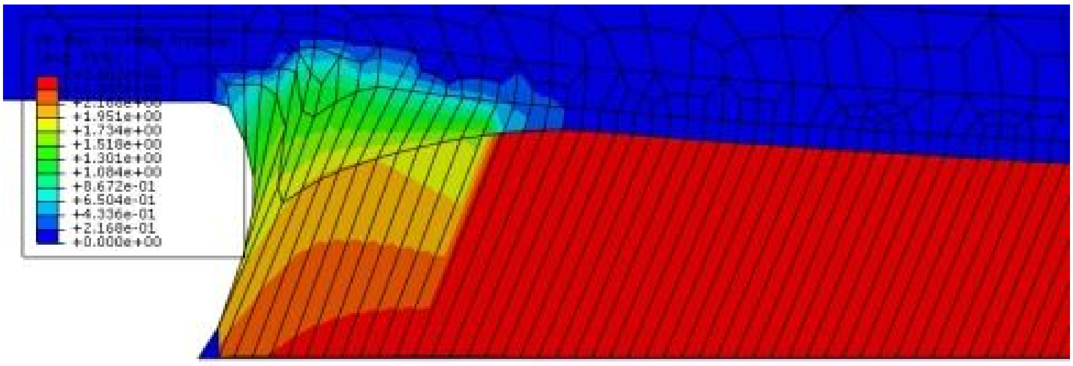

Figure 27 Contour Plot of the Plastic Strain for Case 1(cohesive energy = $100\%\Gamma_n$at Global Displacement Level =0.3mm)

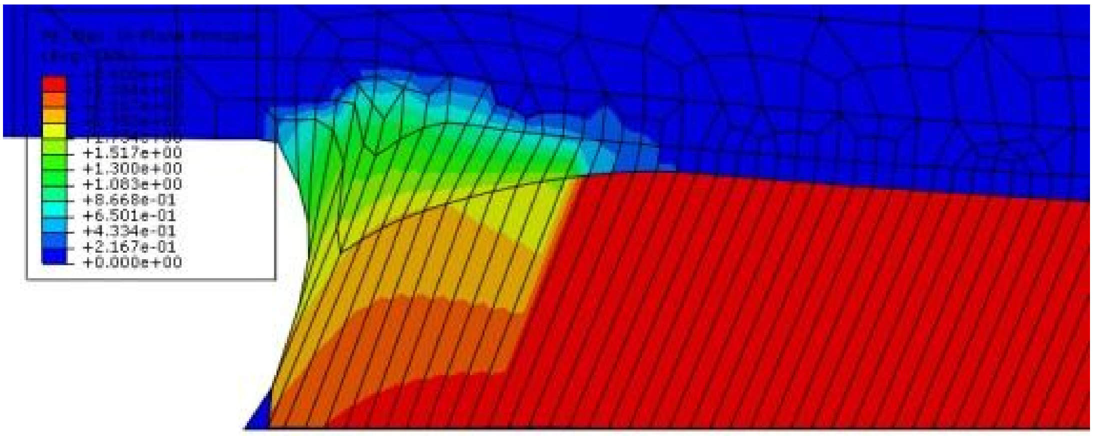

Figure 28 Contour Plot of the Plastic Strain for Case 2-2($\text{cohesive energy} = 25\%\Gamma_n$at Global Displacement Level =0.3mm)

As shown in Fig.27 and Fig.28, one can see that, for both cases, the elongation in the adjacent continuum material is very large and the plastic zone has developed to a further region before we can observe any crack initiation.

In addition, the global load-displacement curve in tension direction is plotted in Fig.29. The external load is obtained as the summation of the reaction force in the tension direction at each node of the load edge.

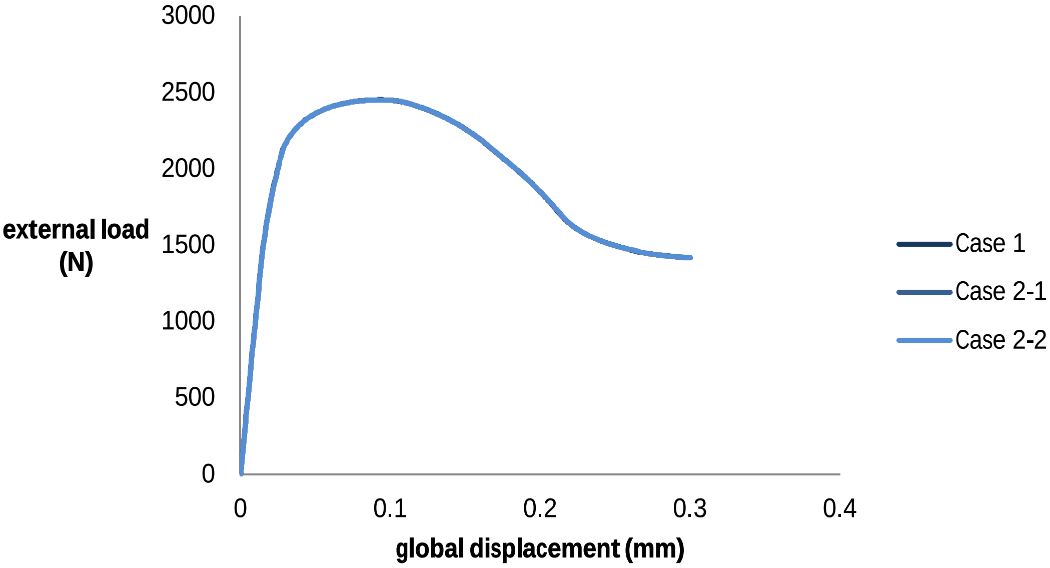

Figure 29 Global Load-displacement for Cohesive Strength $\sigma_{\max} = 3\sigma_y$

From the above we can find that the global softening behaviour in each of these three cases is almost identical and is governed by the plastification of the continuum material itself. The influences of the cohesive energy are suppressed because a too high cohesive strength has prevented the initiation of the damage process.

B $\sigma_{\max} = 1.5 \cdot \sigma_y$

When the cohesive strength equals to $1.5 \cdot \sigma_y$, the damage process is facilitated and can be observed due to the lowered criterion for damage initiation. Typical results depicted as examples in Fig.30 and Fig.31 can be found as following.

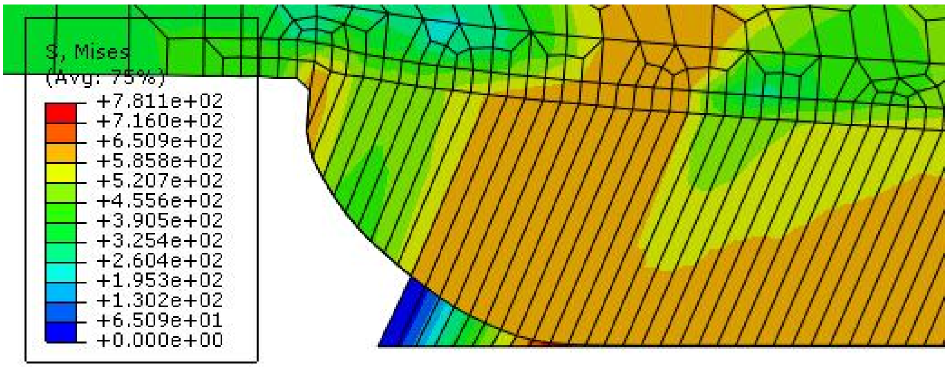

**Figure 30 Final Crack Extension for Case 2-5(cohesive energy = $12.5\%\Gamma_n$ at Global Displacement level =0.3mm)**

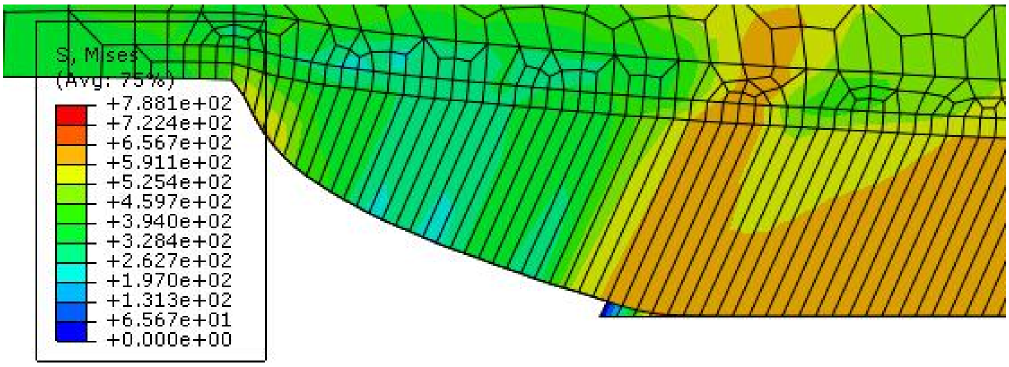

**Figure 31 final crack extension for Case 2-10(cohesive energy = $3.125\%\Gamma_n$ at Global Displacement Level =0.3mm)**

The plastic zone developed at the crack initiation is plotted in Fig.32.

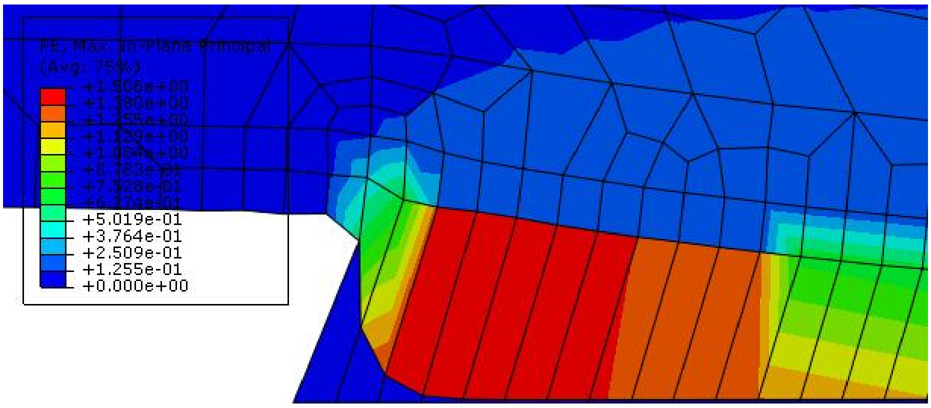

**Figure 32 contour plot of the plastic strain for Case 2-5 (at global displacement level =0.13mm when crack initiates)**

Moreover, it has been noticed that the value of the cohesive energy plays a more important role in cracking process and this will be addressed in detail in the following Section 3.2.3.

C $\sigma_{\max} = 1 \cdot \sigma_y$

One can expect that an further lowered value of the cohesive energy may accelerate the crack initiation and that a smaller size of the plastic zone at crack initiation. This has been proved in the analysis of Case 2-8and Case 2-9 and shown in Fig.33.

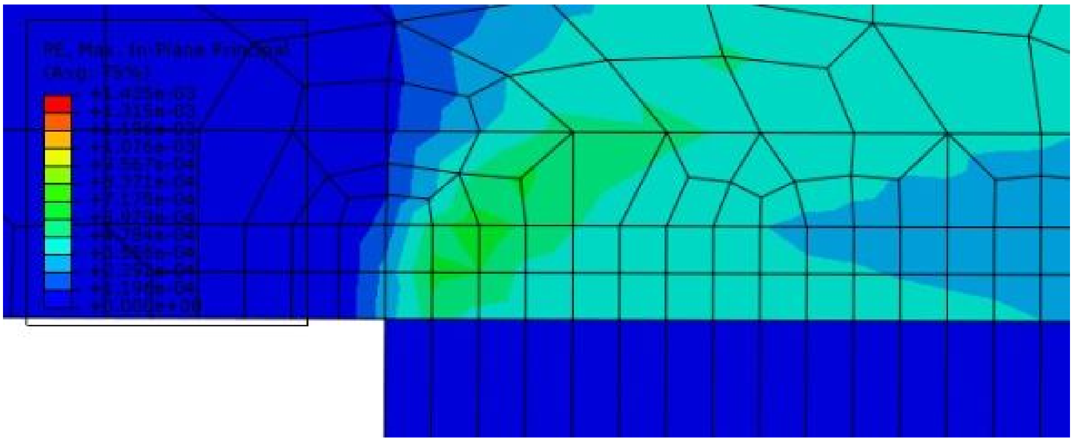

Figure 33 contour plot of the plastic strain for Case 2-9 (at global displacement level =0.04mm when crack initiates)

In both the two cases, the crack initiates rapidly and extends to an abrupt rupture of the failure. This can also be reflected in the global load-displacement curves as in Fig.34.

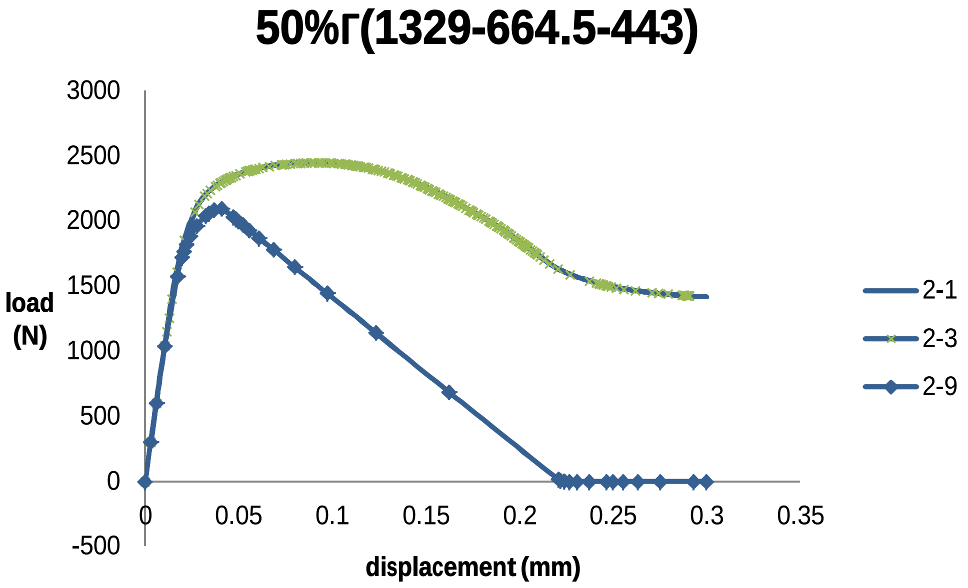

Figure 34 global load-displacement curves for Case 2-1, 2-3 and 2-9 cohesive energy = $50\%\Gamma_n, \sigma_{max} = 3\sigma_y, 1.5\sigma_y, 1.0\sigma_y$ respectively

### 3.2.3.2 Influences of the Cohesive Energy

A influences on the global behaviour

The influences of the cohesive energy on the crack propagation is viewed among Case2-3, 2-4, 2-5, 2-6, 2-7 and 2-10. No crack propagation is found in Case2-3( $50\%\Gamma_n$ ) and Case 2-4( $25\%\Gamma_n$ ). This is because of the excessively tolerant criteria for the failure, i.e. the critical separation is a too large value that slows down the damage process in the cohesive element. However, crack propagation is observed with an even lowered value in the cohesive energy.

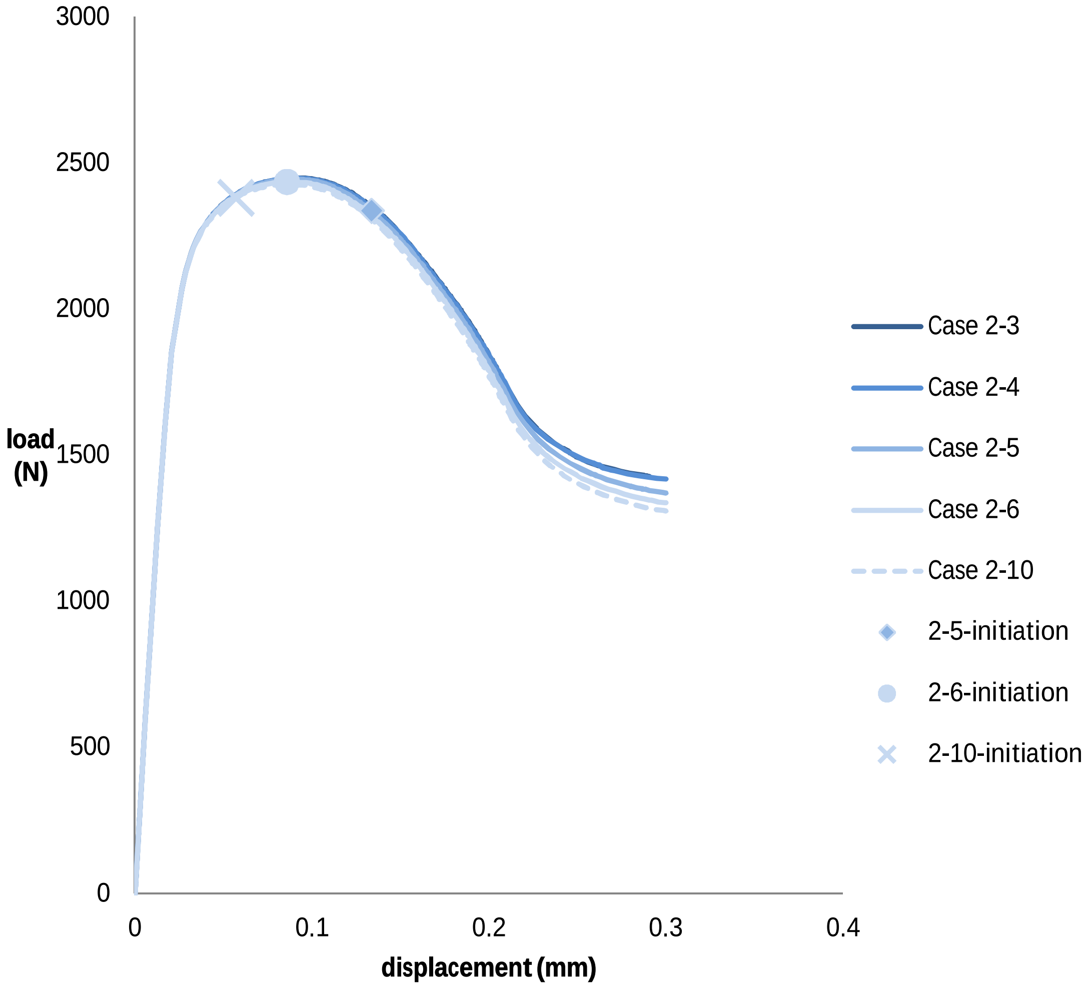

Figure 35 Global Load-Displacement Curves for Cases with $\sigma_{max} = 1.5\sigma_y$

As depicted in Fig.35, with smaller cohesive engergy the crack initiates ealier. Meahwhile the global load-displacement curve drops to a lower level, which can be explained as less energy needed for the formation of the new crack faces.

B influences on the crack extension process

It is interesting to study how would the input cohesive engergy influence the crack propagation in the Case 2-5,6,7,10. Fig.36 has shown the crack extension during the loading process. For the 4 cases in the figure, One can see that

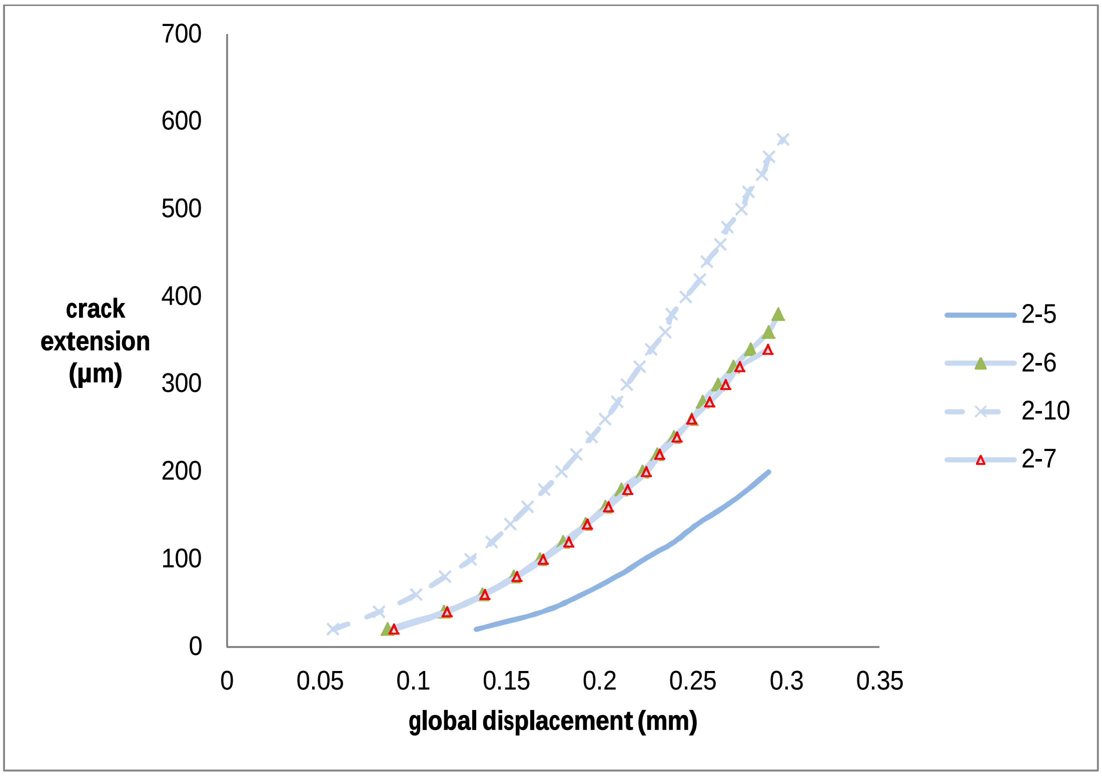

Figure 36 Crack Extension During loading process

1) the crack propagation speed is increasing accoding to the increasing tangent of the curve, and tend to stablise in the later stage;

2) the crack propagates faster given smaller cohesive engergy;

3) the final crack size increases with decreasing cohesive energy.

C influences on the cohesive zone length

As shown in Fig.37, the cohesive zone is defined as the damage process zone in front of the current crack tip, which starts from the location reaching just the cohesive strength to the location where critical separation occurs (the crack tip). The length of the cohesive zone is denoted as $l_{cz}$.

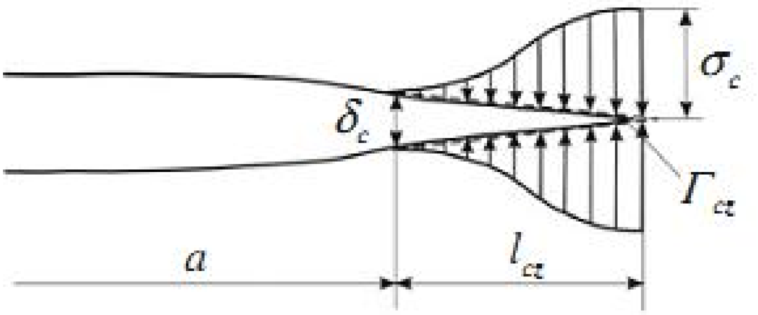

Figure 37 Cohesive Zone ahead of the Crack Tip

Where a represents the current crack length.

Because the interfacial constitutive relation is specified along the entire interface which is a predefined crack path in our case, no cohesive zone size needs to be determined by the analysis.

However, the cohesive zone length may reflect a linkage between the cohesive parameters and the physical behaviour of the cracking process. As shown in Fig.38, the change of cohesive zone length which lies ahead of and moves along with the corresponding crack tip is plotted, one can find that

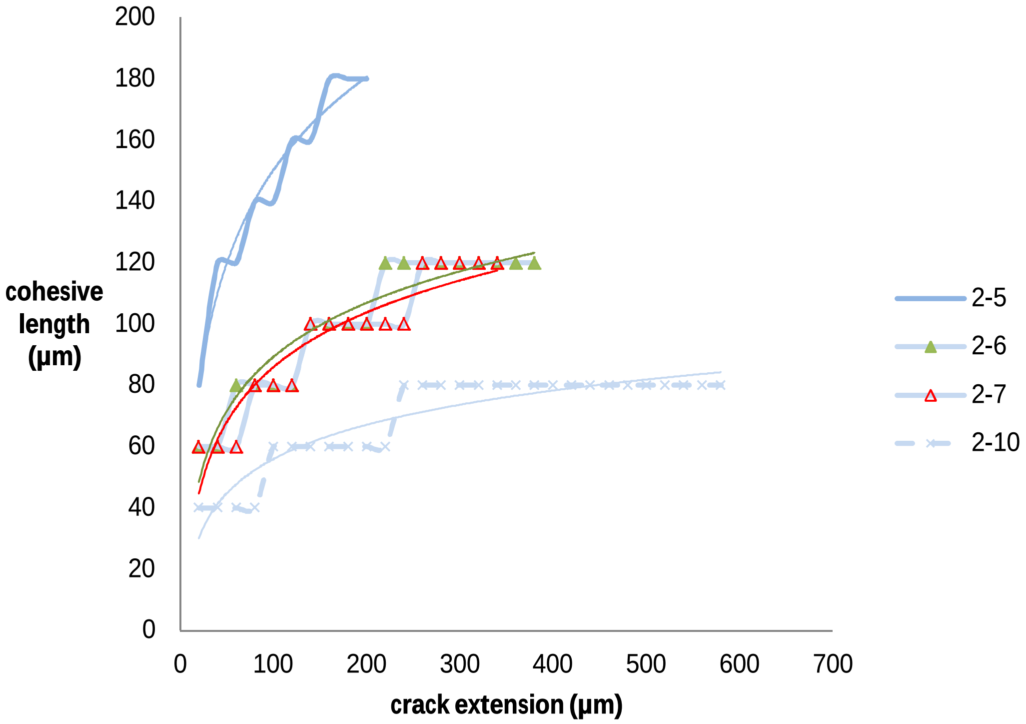

Figure 38 Change of Cohesive Length during Crack Extension

1) the cohesive zone length increases during crack propagation and tends to stabilize to a steady value as the crack propagates;

2) the cohesive zone length increases when the cohesive energy increases, because a higher level of cohesive energy requires a larger area to for the energy dissipation.

In addition, Case 2-6 and Case 2-7 have applied the same cohesive strength and cohesive energy but different values for initial elastic stiffness. From Fig.36 and Fig.38, one can say that during crack propagation the influence of the initial elastic stiffness is minor.

### 3.2.4 Mesh Refinement Test

From the previous study, the final crack extends to a maximum of 0.58mm, thus the previously stated fine mesh zone of 3mm is proven to be able to cover the whole crack propagation process. On the other hand, it is observed that the cohesive length, e.g. in Case 2-6, has covered over 3 elements, it is interesting to find out whether the mesh size of 0.02mm here is sufficiently small to capture the softening behaviour with the presence of high plastification in the surrounding material.

Thus the mesh of the fracture specimen model is refined to a level of 0.01mm, and the fine mesh zone is kept as 3mm as before. The detail of mesh around the cohesive zone can be found in Fig.39.

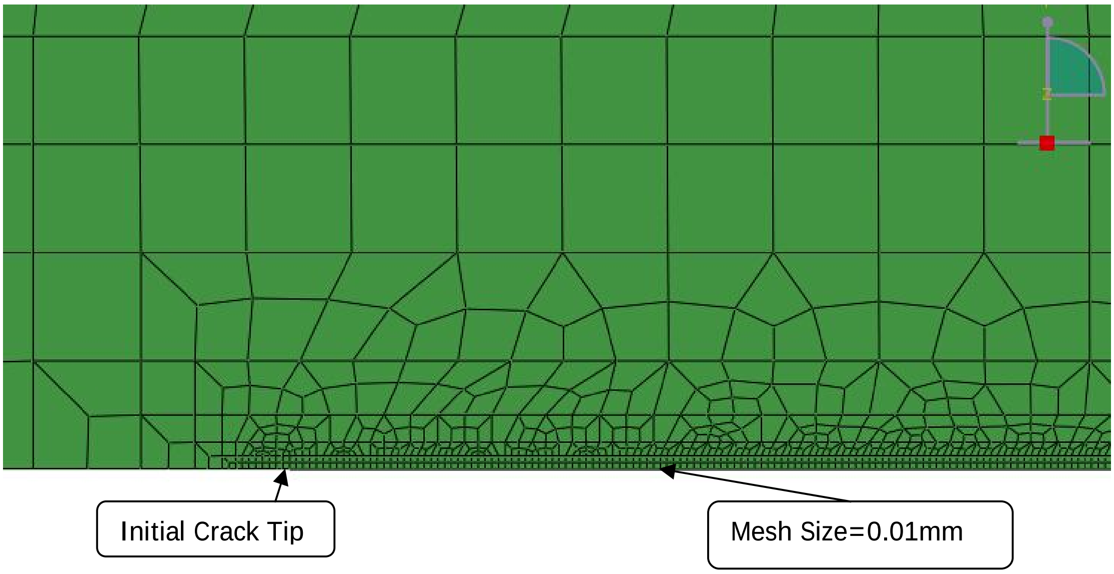

Figure 39 Mesh Detail around the Cohesive Zone with Refined Mesh Size=0.01mm

The material input and boundary conditions are still applied same as Case2-6 previously. The result of crack extension during loading is plotted in Fig.40 in comparison with that of Case 2-6.

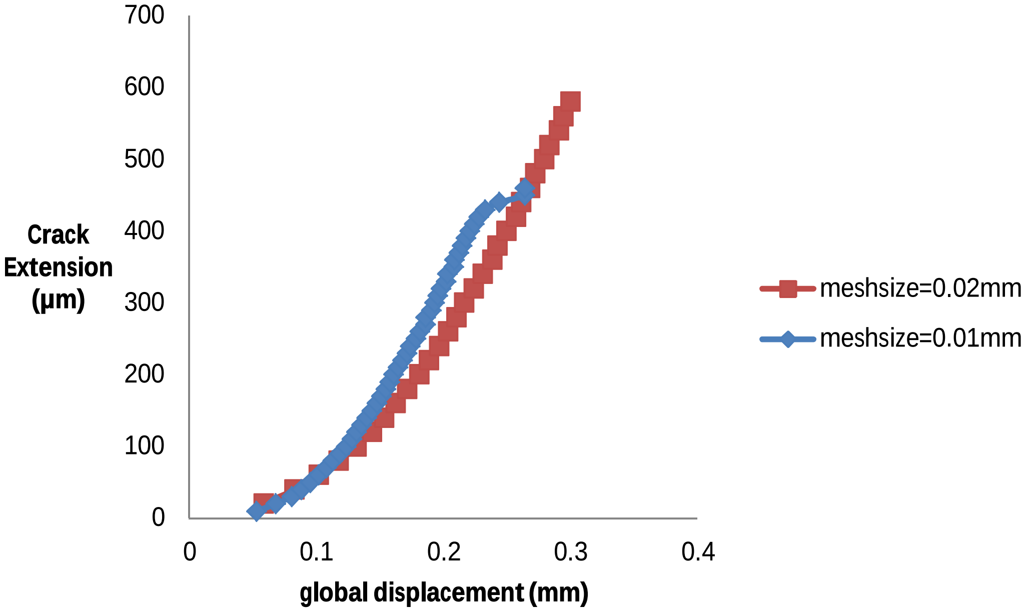

Figure 40 Comparison Between the Two Mesh Sizes

As one can find that different sizes for the model gives different results on crack simulation, which indicates that the mesh size has a influence on the crack behaviour in the cohesive zone. However, the difference between the results of the two mesh sizes is small, especially in the earlier stage. This implies that the mesh size of 0.02 mm can provide relatively accurate results regarding the crack initiation period or one may say that the latter is less sensitive to the mesh size than the propagation period. In all, it is assumed that the difference is small and the mesh size of 0.02 is able to provide results accurate to an acceptable level. In order to reduce the time of computation and to improve the simulation efficiency, the fracture specimen model in later analysis is applied with the mesh size of 0.02mm.

### 3.2.5 Conclusions

From the parametric study on the cohesive parameter, one may conclude that

1) There is a huge difference in the parameter calibration between the suggestions in literature and the work done in this section, in terms of cohesive energy and cohesive strength. For preliminary study, to observe crack propagation, the reasonable values are suggested approximately as

$$\Gamma_n \approx 3\% \frac{K_{Ic}^2}{E'}, \quad \sigma_{\max} \approx 1.5\sigma_y$$

2) The cohesive strength influences the plastification developing near the crack tip. A larger value facilitates the plastification in the material and delays or prevents the full development of the cohesive zone and vice versa.

3) The cohesive energy controls the energy needed for the full development of the cohesive zone. In this way, a larger value of cohesive energy delays the crack initiation and decreases the speed and the amount of crack extension. The size of the cohesive zone tends to stabilize during crack propagation. And the cohesive zone length increases with increased level of cohesive energy

## 3.3 Comparison with Experimental Test Results

### 3.3.1 Methodologies

In this section, the ABAQUS standard cohesive element with triangle-shaped TSL will be applied in calibration for the experimental test results. The geometry and mesh information of the model applied remains the same as in the Section 3.2.2 in accordance with [18], but the elastic-plastic property of the continuum material is changed to the actual material used in the SENT fracture test as in [18]. The material properties in the form of Ramberg-Osgood Law are listed in Table.2.

$$\varepsilon = \frac{\sigma}{E} + \alpha \frac{\sigma_0}{E}\left(\frac{\sigma}{\sigma_0}\right)^{n} \qquad \text{(Eq.14)}$$

**Table 2 Material Input**

| | |
|---|---|
| elastic modulus | 211 Gpa |
| Poisson's ratio | 0.29 |
| $\sigma_0$ | 504 Mpa |
| $\alpha$ | 0.926 |
| n | 7.53 |

The experimental test results are recorded as J-Resistance Curves as introduced previously in Section 2.1.5. According to the study in Section 3.2, the approximations for the cohesive parameters are

$$\Gamma_n = 12N/mm, \quad \sigma_{\max} \approx 1.5\sigma_y$$

In order to calibrate the experimental results with numerical simulation and to study further on how the influences of the cohesive parameters are reflected in J-Resistance Curve. A new series of simulation cases with marks are analysed and can be traced in Table 3..

**Table 3 Cases for analysis in parametric study**

|  | $\Gamma_n = 18N/mm$ | $\Gamma_n = 12N/mm$ | $\Gamma_n = 6N/mm$ |
|---|---|---|---|
| $\sigma_{\max} = 2.5 \cdot \sigma_y$<br>$=1260Mpa$ |  | Case 3-1<br>211-0.0190 |  |
| $\sigma_{\max} = 2 \cdot \sigma_y$<br>$=1008Mpa$ |  | Case 3-2<br>211-0.0238 |  |
| $\sigma_{\max} = 1.75 \cdot \sigma_y$<br>$=882Mpa$ |  | Case 3-3<br>211-0.0272 |  |
| $\sigma_{\max} = 1.5 \cdot \sigma_y$<br>$=756Mpa$ | Case 3-6<br>211-0.0476 | Case 3-4<br>211-0.0317 | Case 3-7<br>211-0.0158 |
| $\sigma_{\max} = 1.25 \cdot \sigma_y$<br>$=630Mpa$ |  | Case 3-5<br>211-0.0381 |  |

### 3.3.2 Path Dependency of J-integral

Path-independent integrals are applied to calculate the intensity of a singularity of a field quantity without knowing the exact shape of this field in the vicinity of the singularity[20]. They are derived from conservation laws.

The concept of path independent integral introduced by CHEREPANOV and RICE (as mentioned in Section 2.1) in linear elastic fracture mechanics, as shown in Fig.41.

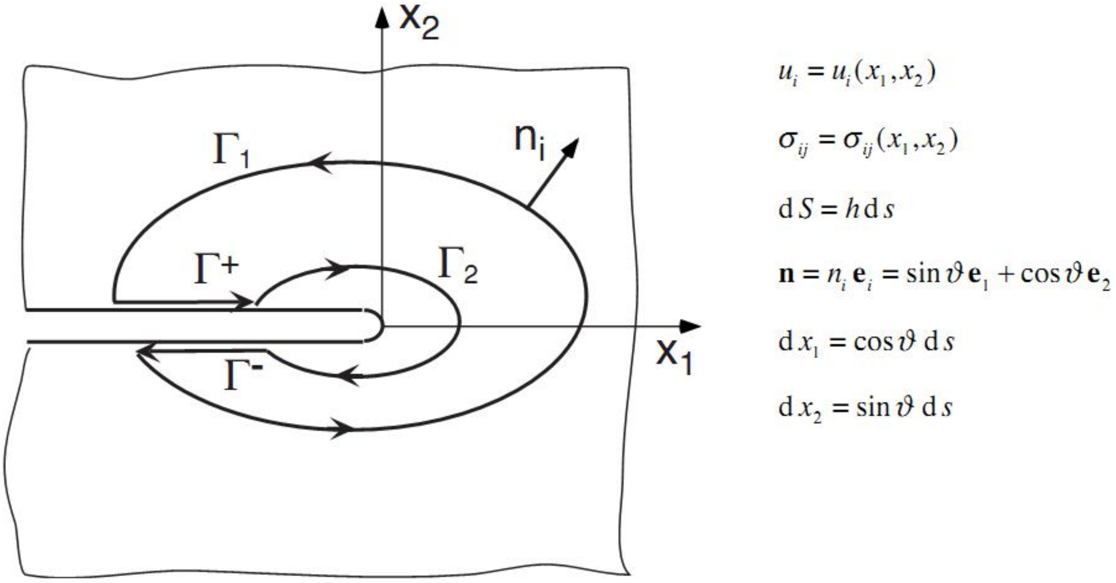

**Figure 41 Definition of Contours for J-integral Evaluation [20]**

The first component of the J-vector is the "J-integral" and can be calculated in the expression as following[20]

$$J = \int_{\Gamma} [W dx_2 - \sigma_{jk} n_k u_{j,1} ds]$$

ABAQUS software calculates the J-integral using the virtual crack extension technique[19].The severest restriction for J results from the assumed existence of a strain energy density, W, as a potential from which stresses can be uniquely derived[20] and in an elastic–plastic material may not allow non-proportional loading and elastic unloading[19]. It does not only exclude any local unloading processes e.g. crack propagation process but also local re-arranging of stresses, i.e. yield conditions near the crack process zone[20]. Therefore, the J-integral will become path dependent as soon as plasticity occurs when the contour $\Gamma$ passes the plastic zone from the yield condition [20]. In other words, as plastic zone develops around the crack tip, the singularity vanishes gradually and becomes not "strong" enough to sustain the property of path independence.

The following of this section aimed to prove the path dependency in the elastic-plastic analysis. The crack tip is selected as the node at the location of the initial crack tip, the red node as one can see in Fig.42. In total, the number of contours is specified as 10 and ABAQUS will decide the actual path of each contour automatically, in the way that the size of the contour increases with increasing number of contour.

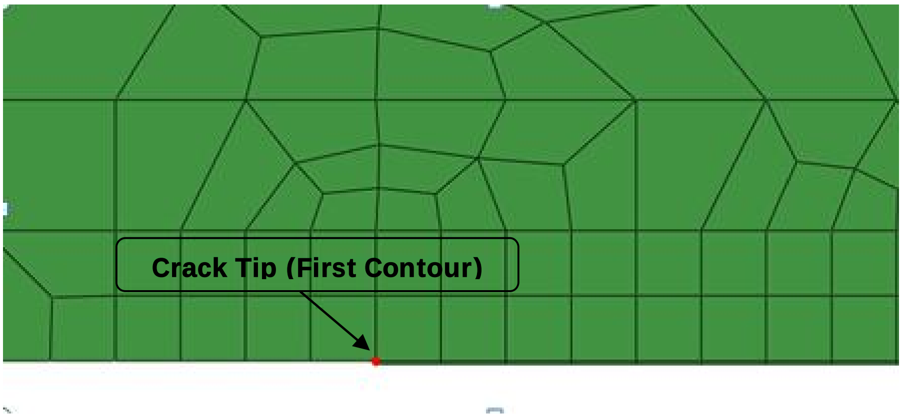

Figure 42 Location of the Crack Tip (red point) Chosen for the Evaluation of J-integral

The analysis configuration is kept the same as Case 2-6. And the results have been plotted in Fig.44 at different crack extension as “snapshot”

Fig.43 shows the change of J-integral during the crack extension. One can see that the value of J-integral increases with increasing contour size but tend to be stabilise as long as the contour has covered the plastic region (i.e. the contours does not cross a plasticised area). Since the plastic zone grows along with the crack propagation, as the plastic zone extends to a larger area, a larger contour is needed in order to improve the path dependence situation and the validity of the data obtained.

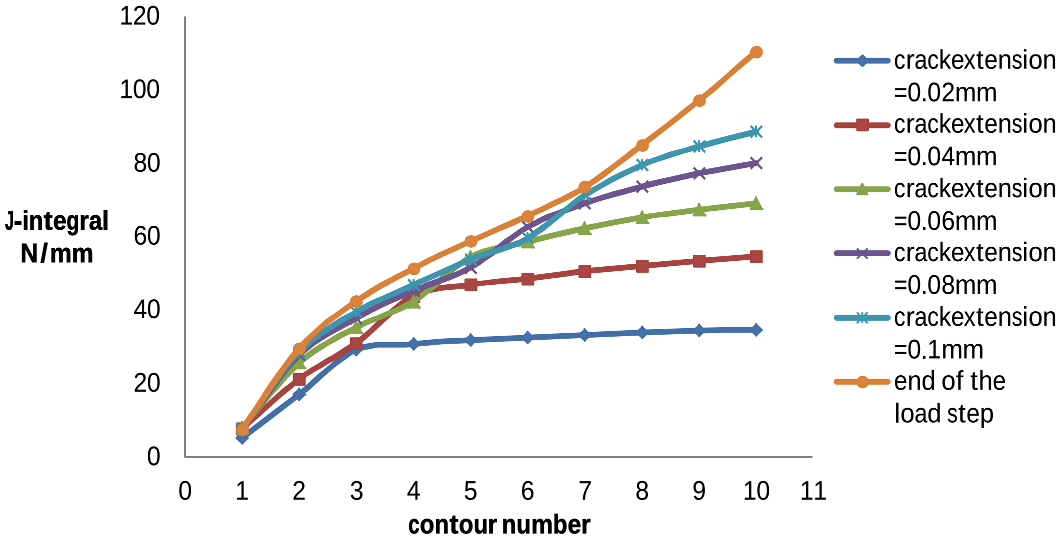

Figure 43 J-integral Evaluated at Each Contour During Crack Extension

As the evaluation of J-integral during crack propagation brings the problem of numerical accuracy, the solution investigated by W. Brocks and I. Scheider[20] has suggested that defining the crack tip a set of nodes as that form the first integral contour and increase the size of the first contour, which helps to mitigate the disturbance of the local plastification and to decrease the number of contours needed to reach the far field value.

### 3.3.3 Results

#### 3.3.3.1 Influences of the Cohesive Parameters on the J-Resistance Curve

As described in Section 3.3.2, the crack tip defined for the calculation of J-integral are depicted in Fig.44. The number of the contour is 10 to make sure the reliability of the J-integral and has been verified afterward.

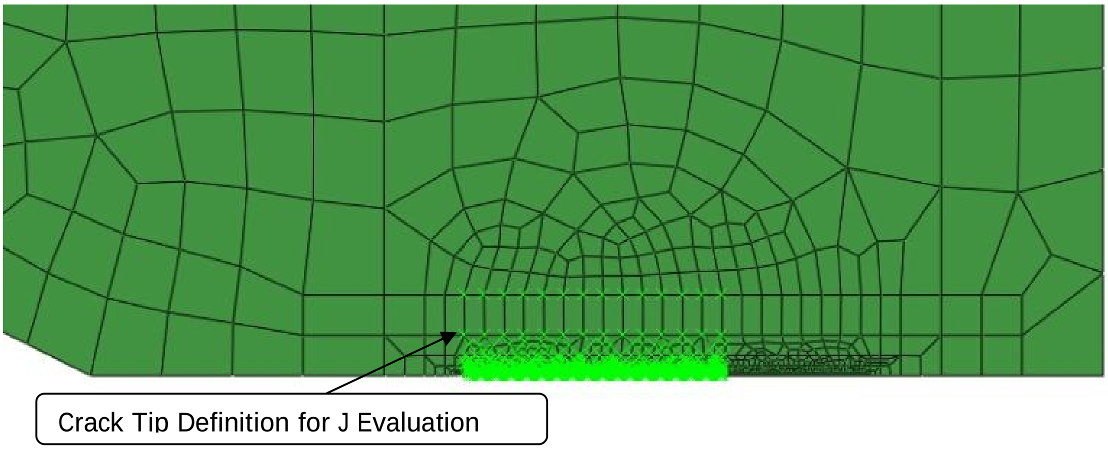

**Figure 44 Definition of the Crack Tip (First Contour)**

The reproduced J-resistance curves are plotted in tow groups, as referred to Fig.45 and Fig.46

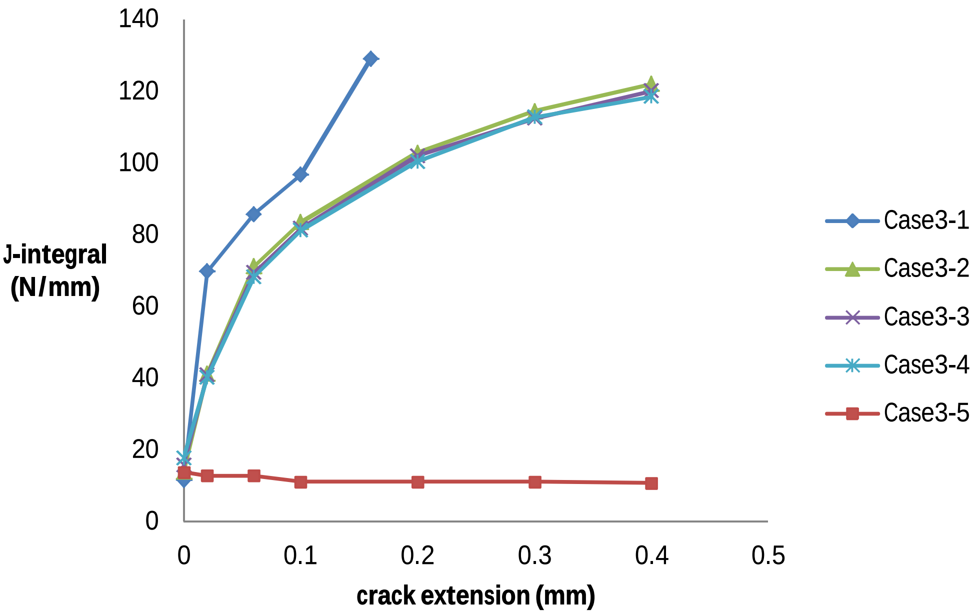

**Figure 45 J-resistance Curves for Cases with $\Gamma_n = 12\mathrm{N/mm}$**

The figure has shown the cases with constant cohesive energy $\Gamma_n = 12N/mm$ but variation in cohesive strength. The crack initiation point (crack extension=0.mm)is defined in the way that the separation of the node pair at the location of initial crack tip has reached the critical separation $\delta_c$, as illustrated in Section 2.4.2 (Fig.12). One may find that

1. The J-integral evaluated at the crack initiation are most equal;
2. The higher the cohesive strength, the faster the J-integral increases while crack propagates, as indicated by the slope of the J-resistance curves, in other words, the higher the cohesive strength, the steeper of the J-resistance curve and vice versa

3. With a higher cohesive strength, a larger value of the J-integral is obtained at the same crack extension.

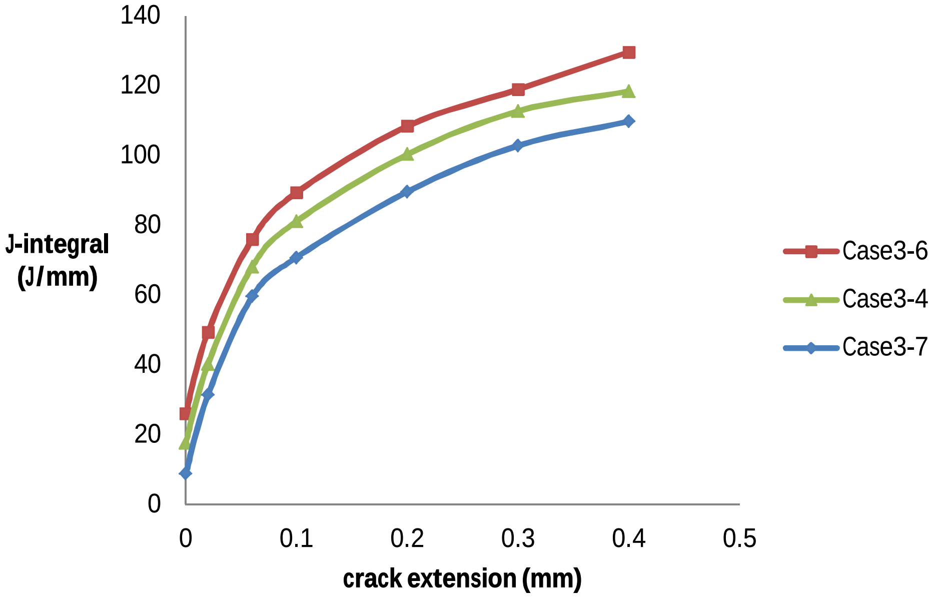

Figure 46 J-resistance Curves for Cases with $\sigma_{max} = 1.5\sigma_y$

Fig. 46 has included the results from the cases with constant cohesive strength $\sigma_{\max} = 1.5 \cdot \sigma_y$ but variation in the cohesive energy. The following observations can be made:

1. The higher the input cohesive energy, the higher value of J-integral is obtained accordingly;
2. Increase in the input cohesive energy leads to the upward shifting of the J-resistance curve but no influence on the slope of the curve.

The observations have suggested a strong relationship between the cohesive energy and the J-integral evaluated at the crack initiation. In Fig.48, the distribution of the J-integral obtained in all the cases at crack initiation is compared the input value of the cohesive energy (solid line). One find that the difference between the two terms can be consider very small. Especially for the cases with $\Gamma_n = 12N/mm$, the variation of J-integral also occurs around the level of the input value of cohesive energy. Taking into account of the numerical errors, one may assume that $J_{\text{ini}} = \Gamma_n$ . This is physically comprehensible considering the theory as introduced in Section 2.4.3

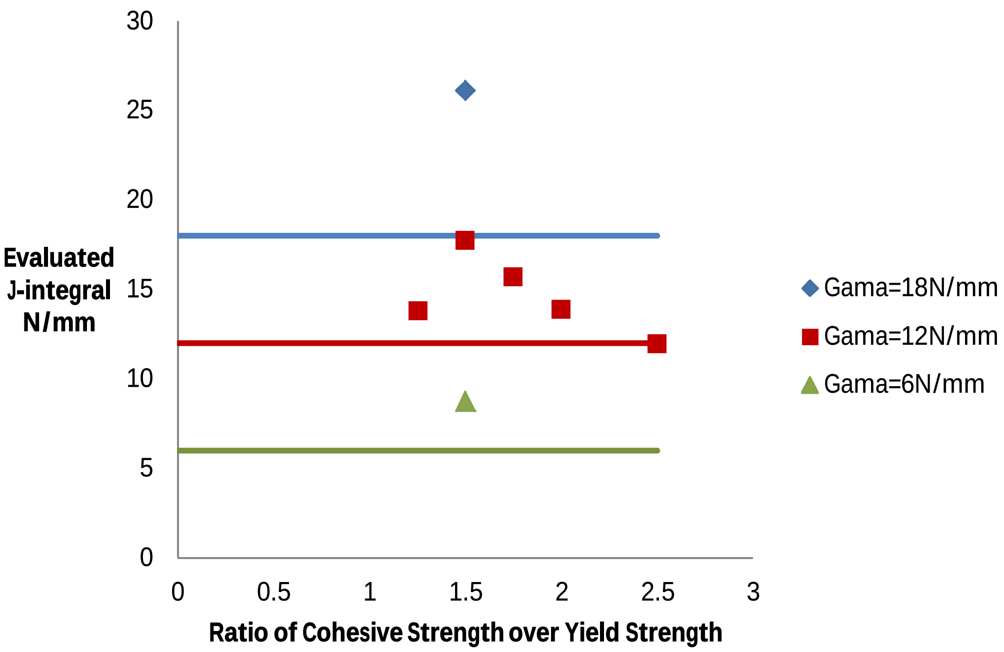

Figure 47 Comparison of J-integral Evaluated at Crack Initiation with Input Cohesive Energy

Moreover, as concluded in Section 3.2.3, increased cohesive strength allows for further development of plastic zone, this could explain the increase of J-integral at the same crack extension. One may assume that the energy input from the applied load is absorbed by both creating new crack surface and plastification of material surrounding the crack tip, i.e.

$$J = \Gamma_n + J_{pl}$$

This can be supported by the fact that the J-integral in EPFM consists of elastic and plastic part, i.e. $J = J_{el} + J_{pl}$ as introduced in Section 2.1.5.2. In other words, a steeper J-resistance curve represents a "more ductile" crack propagation, which can be controlled by the cohesive strength.

### 3.3.1.2 Comparison with Experimental Results

The experimental data obtained from the SENT test needs to be calibrated by the result of the simulation. The experimental test data in the form of J-resistance series are listed in Table 4 [18]

**Table 4 Experimental Results of the Fracture Test**

| crack extension (mm) | J-integral (N/mm) |
|---|---|
| 0.6 | 506 |
| 0.7 | 523 |
| 1.0 | 794 |
| 1.2 | 777 |
| 1.2 | 1055 |
| 1.4 | 1292 |
| 1.4 | 1030 |
| 1.5 | 1351 |

As shown in Fig.48, one may find that the difference between the experiments and simulation results is big. It is very hard to obtain experimentally an accurate J value at the moment of crack initiation (where crack extension = 0), so the cohesive energy calibrated is not comparable in this case due to lack of experimental data. However, it is observable that the trend line for the experimental J-resistance curve indicates a much higher slope than the simulation results.

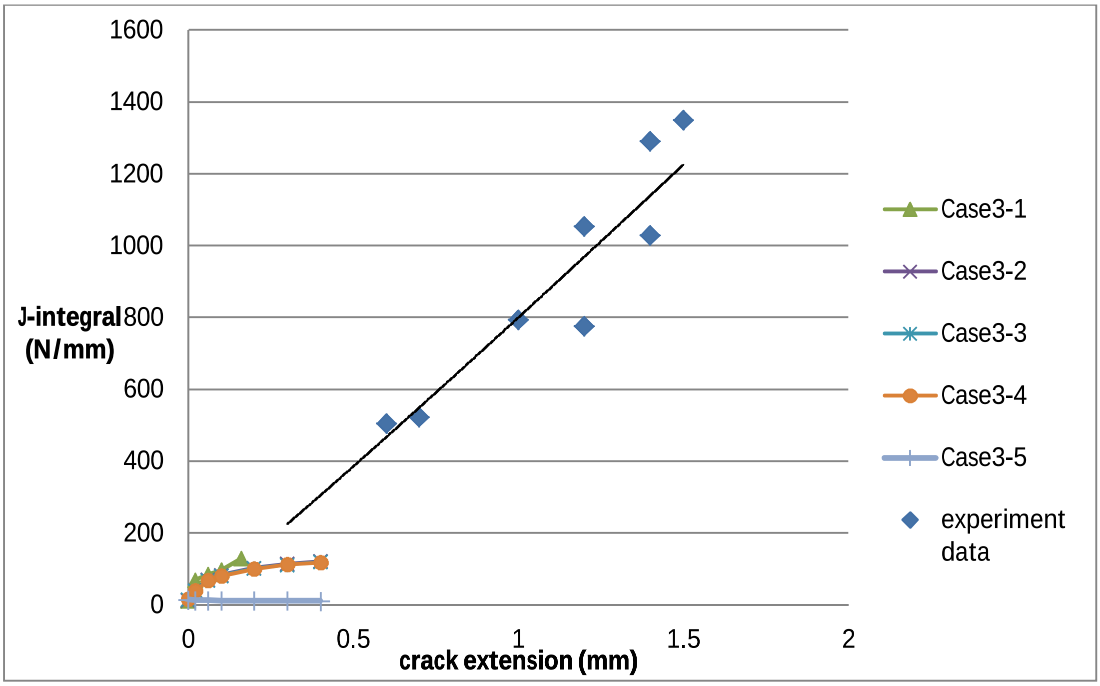

Figure 48 Comparison of the Experimental Test Data to Calibrate the Simulation Results

As concluded before, this suggests that the plastic component is larger and that the real situation occurs in a “more ductile” sense. Therefore a higher value of cohesive strength is expected. However, it is proven not realistic in Case 2-1 and Case 2-2 because a too high value (i.e. $\sigma_{\max} = 3 \cdot \sigma_y$) blocked the damage in the cohesive zone where it is supposed to take place and made the adjacent material governing. This implies that the ABAQUS standard cohesive element with triangle shaped TSL is not able to capture the ductile behaviours of crack propagation in pipeline steel X65.

### 3.3.4 Conclusions

In this section one may conclude that

1) The distribution of the path-dependent J-integral is an increasing function of the path size in elastic-plastic analysis.

2) The influence of the cohesive parameters on the J-resistance curve is studied further. On one hand, an increased cohesive energy gives a higher J-integral evaluated as crack initiation. The fact that an increasing cohesive energy shifts the curve upward on a whole scale implies that the cohesive energy doesn't change the ductility once the crack is propagating with the given TSL shape.

On the other hand, a higher cohesive strength allows for a greater level of plastic energy dissipation and thus increases the slope of the J-resistance curve i.e. the ductility. To a large level, the results align with the conclusions obtained in 3.2.

3) The cohesive parameter calibration for pipeline steel X65 may not be conducted using ABAQUS standard cohesive element. This may be explained that the failure mechanism implemented in ABAQUS is different. The triangle shape of TSL is not able to capture the ductile crack propagation in pipeline steel and is more suitable for brittle or quasi brittle material. Meanwhile, according to the manual [41], the TSL applied has described the separation between the two fictitious crack faces only while ABAQUS relate the TSL back to the damage mechanism developing in a bulk material, e.g. adhesives. Thus it is necessary to implement the intended separation behaviour into the cohesive element, which can be accomplished by user subroutine UEL (user element) or in some cases UMAT (user material) [48]. In this project, subroutine UEL is developed and are illustrated in Section 4 and Section 5Crack Propagation under Monotonic Static Loading using user defined element

# 4.0 CRACK PROPAGATION SIMULATION UNDER MONOTONIC STATIC LOADING USING UEL

## 4.1 Finite Element Formulation

The implementation of an element follows a sequence of establishment of equilibrium equation (and in weak form), spatial discretization, and the calculation of nodal force vector $f_{\mathrm{c}}$ and tangential stiffness $K_c$ [29]. The last two terms $f_{\mathrm{c}}, K_c$ will be provided to the ABAQUS main code as $-RHS, AMATRX$ through the UEL subroutine interface. The weak from of the governing equilibrium equation is obtained from the principle of the virtual work [29]. As depicted in Fig.49, the domain $\Omega$ is divided into two subparts $\Omega_{+}, \Omega_{-}$ by a predefined cohesive layer $\Gamma_c$, which allows the crack to propagate.

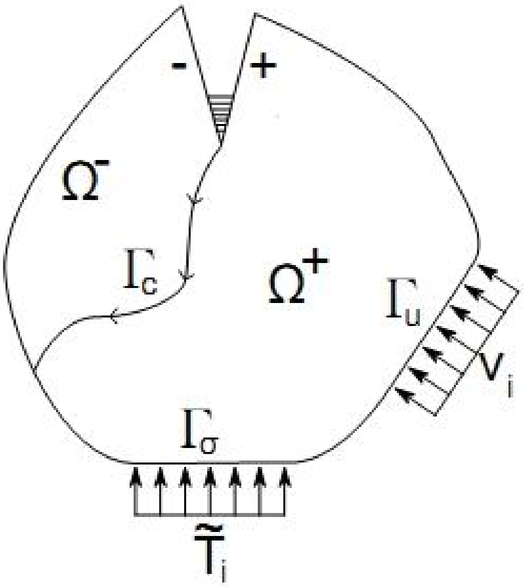

Figure 49 Illustration of the boundary value problem [48]

The summation of the virtual strain energy in the domain ( $\Omega = \Omega_{+} + \Omega_{-}$ ) and the cohesive fracture energy evaluated on the interfaces $\Gamma_c$ is equal to the work done by the external traction $T_{ext} = T_{\sigma} + T_u$ on the boundary $\Gamma_{ext} = \Gamma_{\sigma} + \Gamma_u$, given in the following [35].

$$\int_{\Omega} \delta\varepsilon \cdot \sigma dV + \int_{\Gamma_c} \delta\Delta \cdot T_c dS = \int_{\Gamma_{ext}} \delta u \cdot T_{ext} dS$$

**(Eq.15)**

Firstly, the entity is discretized into finite elements. The solution variables here is the displacement field $u(\bar{x}) = \mathrm{H}\bar{u}(\bar{x})$, this process is completed in the pre-processor in ABAQUS

Where $\mathrm{H}$ is the shape function characterising the field interpolation during discretization,

$\bar{u}(\bar{x})$ *or* $\bar{u}$ is the nodal displacement in global coordinate system $\bar{x}$ .

Secondly, the user defined cohesive element incorporates the relation between the local separation and traction which is ultimately relating the global nodal displacement to the nodal forces. In order to obtain the local separation from the global nodal displacement, the global coordinates $\bar{x}$ are first transformed to the local coordinates $\tilde{x}$ of the user defined cohesive element by a transformation matrix $\Lambda$ and $\tilde{x} = \Lambda\bar{x}$

$$\Lambda = \begin{bmatrix} \cos\theta & \sin\theta \\ -\sin\theta & \cos\theta \end{bmatrix}$$

**(Eq.16)**

Where $\theta$ is the angle between in the local and the global coordinate system.

Commonly, the local coordinate system should be determined in the deformed shape [16]. In our project, because of axis-symmetry, the local $\tilde{x}$ axis complies with the symmetry axis. As shown in Fig. 50, a 4-noded element is considered, with 2 degrees of freedom (DOF) at each node.

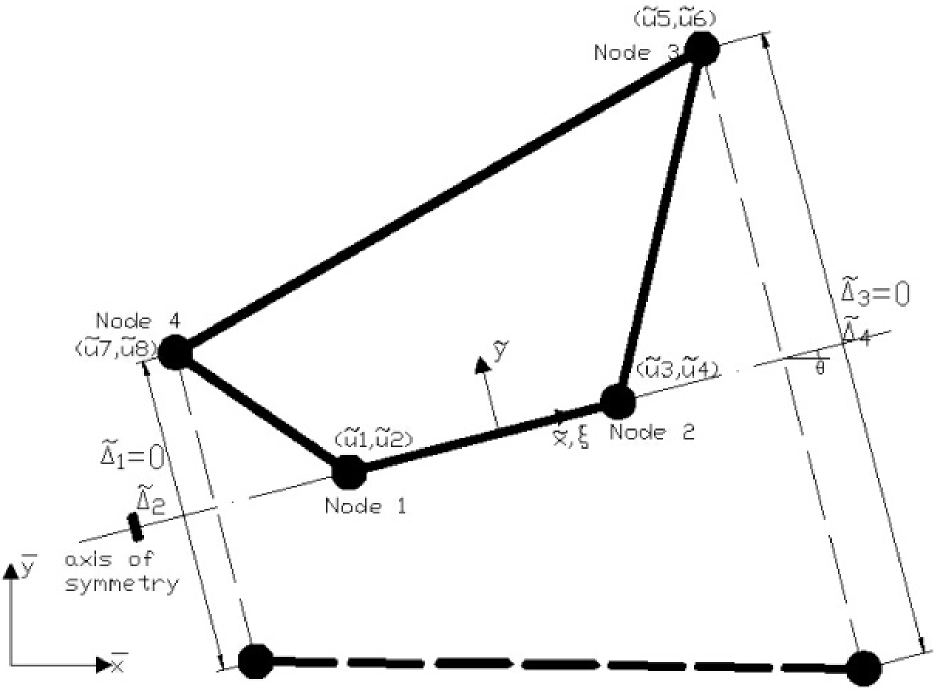

**Figure 50 illustration of the user cohesive element under deformed situation**

Similarly, the global nodal displacement $\bar{u}$ is transformed to the local nodal displacements $\tilde{u}$ by an 8*8 rotational matrix $R$

$$R = \begin{bmatrix} \Lambda & 0 & 0 & 0 \\ 0 & \Lambda & 0 & 0 \\ 0 & 0 & \Lambda & 0 \\ 0 & 0 & 0 & \Lambda \end{bmatrix}$$

**(Eq.17)**

Thirdly, one can obtain the local separation at the node pairs (two pairs in one 4-noded element) as local nodal displacement jump by $\tilde{\Delta} = L\tilde{u}$ .

Where $L$ is a local displacement-separation relation matrix;

$\tilde{u}(\tilde{x})$ or $\tilde{u}$ The nodal displacement in local coordinate system $\tilde{x}$

$\tilde{\Delta}(\tilde{u})$ or $\tilde{\Delta}$ The separation at the nodal pair in local coordinate system $\tilde{x}$

Again, since an axisymmetric problem is considered, the separation in the local $\tilde{x}$ direction is zero (Fig.50). Then one can rewrite the relation $L$ as

$$\underbrace{\begin{bmatrix} \tilde{\Delta}_1 \\ \tilde{\Delta}_2 \\ \tilde{\Delta}_3 \\ \tilde{\Delta}_4 \end{bmatrix}}_{\tilde{\Delta}} = \underbrace{\begin{bmatrix} 0 & 0 & 0 & 0 & 0 & 0 & 0 & 0 \\ 0 & -2 & 0 & 0 & 0 & 0 & 0 & 2 \\ 0 & 0 & 0 & 0 & 0 & 0 & 0 & 0 \\ 0 & 0 & 0 & -2 & 0 & 2 & 0 & 0 \end{bmatrix}}_{L} \underbrace{\begin{bmatrix} \tilde{u}_1 \\ \tilde{u}_2 \\ \tilde{u}_3 \\ \tilde{u}_4 \\ \tilde{u}_5 \\ \tilde{u}_6 \\ \tilde{u}_7 \\ \tilde{u}_8 \end{bmatrix}}_{\tilde{u}}$$

**(Eq.18)**

$$\tilde{\Delta}_1 = 0; \tilde{\Delta}_2 = 2(\tilde{u}_8 - \tilde{u}_2); \tilde{\Delta}_3 = 0; \tilde{\Delta}_4 = 2(\tilde{u}_6 - \tilde{u}_4)$$

**(Eq.19)**

Fourthly, the element separation at each integration point can be interpolated from the separation at the node pair. Here the cohesive element is one-dimensional and a linear interpolation rule is applied, as shown in Fig. 51.

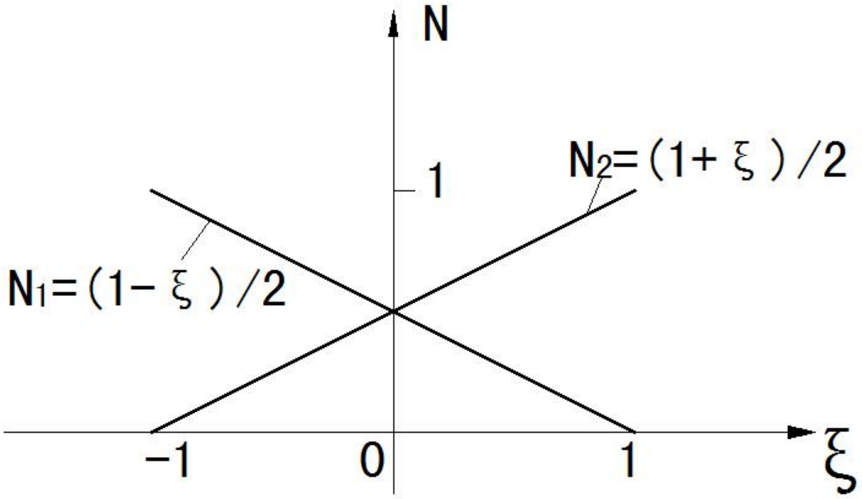

Figure 51 linear interpolation functions

Where the linear shape functions in the natural coordinate ( $\xi$ ) are given as

$$N_1 = \frac{1-\xi}{2}, N_2 = \frac{1+\xi}{2}; \quad \xi \in [-1,1] \tag{Eq.20}$$

The separation at each integration point is then determined in $\Delta = N\tilde{\Delta}$ and detailed as following

$$\underbrace{\begin{bmatrix} \Delta t \\ \Delta n \end{bmatrix}}_{\Delta} = \underbrace{\begin{bmatrix} N_1(\xi = x_i) & 0 & N_2(\xi = x_i) & 0 \\ 0 & N_1(\xi = x_i) & 0 & N_2(\xi = x_i) \end{bmatrix}}_{N} \underbrace{\begin{bmatrix} \tilde{\Delta}_1 \\ \tilde{\Delta}_2 \\ \tilde{\Delta}_3 \\ \tilde{\Delta}_4 \end{bmatrix}}_{\tilde{\Delta}} \tag{Eq.21}$$

Where $x_i$ is natural coordinates of the integration point;

$\Delta(\tilde{x})$ *or* $\Delta$ is the separation at the integration point in local coordinate system $\tilde{x}$

Next, the relationship from between the local separation and the global nodal displacement can be determined based on the previous equations.

$$\Delta = B_c \bar{u} = \underbrace{\mathrm{NLR}}_{B_c} \bar{u} \tag{Eq.22}$$

Finally, the internal nodal force vector $f_c$ is given based on the $B_c$ matrix as [35]

$$f_c = \int_{\Gamma_c} B_c^T T_c dS \tag{Eq.23}$$

The gradient of the nodal force vector $f_c$ leads to the tangential stiffness matrix $K_c$ [35], which is

$$K_c = \frac{\partial f_c}{\partial \bar{u}} = \int_{\Gamma_c} B_c^T \frac{\partial T_c}{\partial \Delta} \frac{\partial \Delta}{\partial \bar{u}} dS = \int_{\Gamma_c} B_c^T \underbrace{\frac{\partial T_c}{\partial \Delta}}_{D_c} B_c dS = \int_{\Gamma_c} B_c^T D_c B_c dS \tag{Eq.24}$$

Where the index c implies cohesive element.

## 4.2 Traction-Separation Law

The TSL implemented is a potential based one proposed by Needleman as introduced in Eq.12 in Section 2.4.2. Since there is no shear separation considered, i.e. $\Delta_t = 0$, the TSL is simplified as following.

$$\mathrm{T_n} = \sigma_{\max} \frac{\Delta_n}{\delta_0} \exp\left(1 - \frac{\Delta_n}{\delta_0}\right) \qquad \textbf{(Eq.25)}$$

The UEL has also considered several load cases as required in the fatigue analysis later. Regarding the algorithm for unloading and reloading cases, the unloading is assumed to occur to be origin of the TSL and the same path is followed in reloading condition, given by

$$T_n = T_{n,\max} + \left(\frac{T_{n,\max}}{\Delta_{n,\max}}\right)(\Delta_n - \Delta_{n,\max}) \qquad \textbf{(Eq.26)}$$

Since there is no tangential separation considered in our axis-symmetrical problem, the interaction between the crack face separations in two directions is ignored.

A crack surface contact model considering overclosure effect is formulated in the algorithm context of the CZM. The traction-overclosure relation follows a linear path such that high penalty stiffness is prescribed for the case of $\Delta_n < 0$ , here the penalty stiffness is chosen as the initial stiffness of the TSL at the location of $\Delta_n = 0$.

$$T_n = K\Delta_n = \frac{\sigma_{0,\max} e}{\delta_0} \Delta_n; \quad \Delta_n < 0 \qquad \textbf{(Eq.27)}$$

## 4.3 Programme Structure

A flowchart of the solution procedure is plotted as the following.

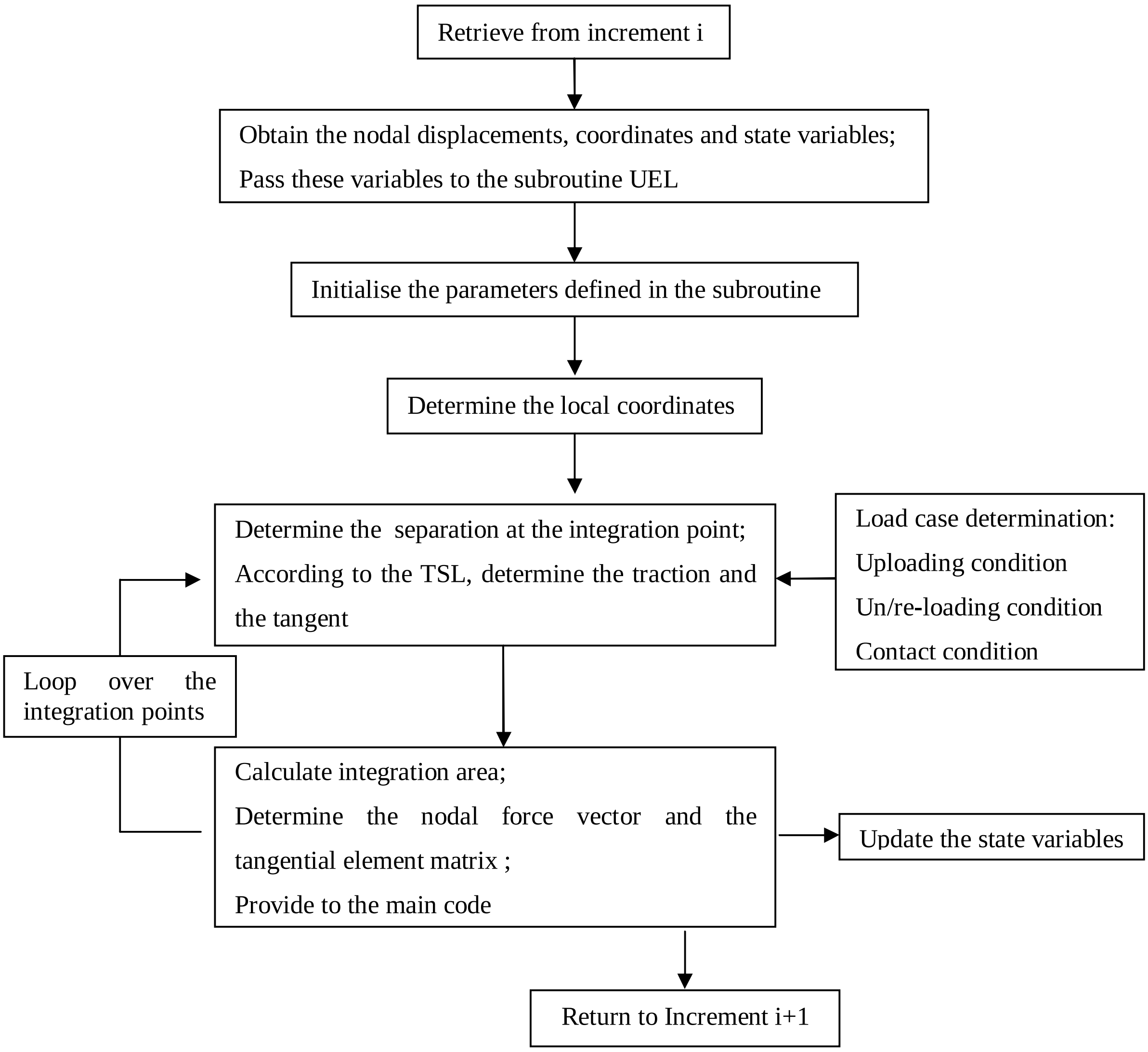

The result of this programme structure leads to the contribution of the user element in terms of the right hand side component and the tangential stiffness matrix at each call to the subroutine during the iteration process.

## 4.4 Patch Test

In order to verify the functionality of subroutine, the patch model as introduced in Section 3.1.1 is applied here and also in the Section 5.3, the static load and later fatigue load is still applied on top edge of the continuum square plate under displacement control method, while the standard cohesive element is replaced by the user element. The implementation of UEL in the INP file for analysis is provided in the Appendix.

The cohesive parameters in the Patch tests are set as:

$$\Gamma_n = 378.7N/mm, \quad \sigma_{\max} = 1260Mpa$$

$$\delta_0 = \frac{\Gamma_n}{e \cdot \sigma_{\max}} = 0.11mm$$

$$\delta_c = 5\delta_0 = 0.55mm$$

In Test 1, the plate is elongated to 0.3mm, where failure of the element is expected. The response of the model in plotted in Fig.52.relating stress and the doubled nodal displacement at the red node in Fig.16.

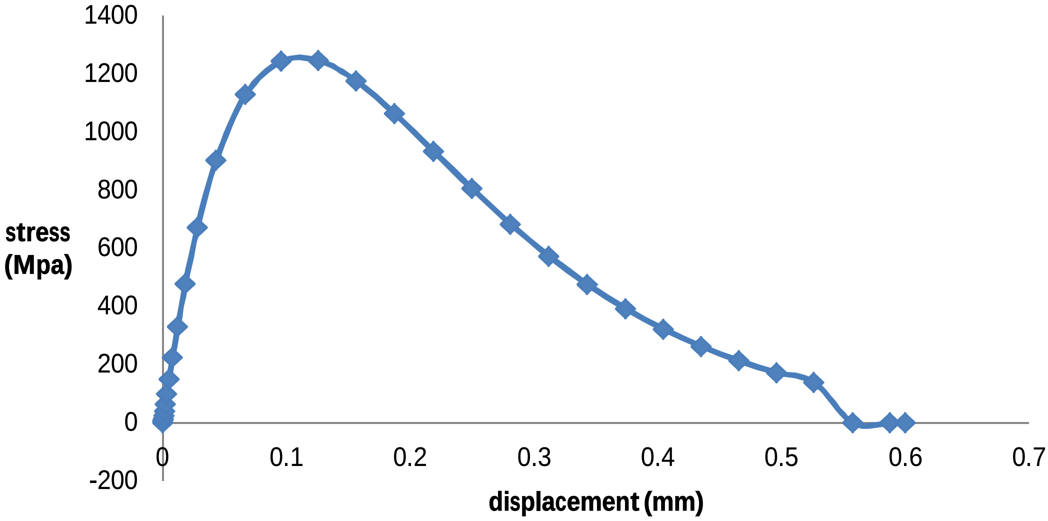

Figure 52 TSL reproduced in the patch test model

In Test 2, the plate is firstly elongated to 0.1 mm , then compressed back to under a compression of 0.005 mm and finally pulled again to 0.3 where the failure of the user cohesive element is expected, i.e. the crack propagates. The response of the patch test model is plotted as in Fig.53.

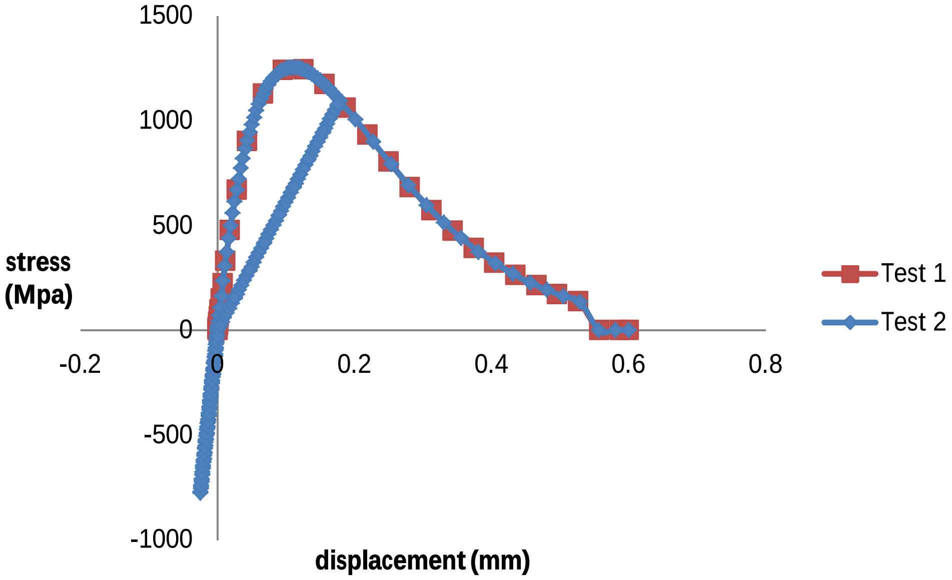

Figure 53 UEL Response in Patch Test Model

# 5.0 CRACK PROPAGATION UNDER FATIGUE LOADING USING UEL

## 5.1 Fatigue Saturation Problem

As mentioned in Section 1, crack propagation under fatigue loading is also very common in engineering practice. Therefore the application of the cohesive element for the simulation of fatigue crack propagation is also studied. In this section, the fatigue saturation problem described in Section 2.4.4 is verified.

The author applied a fatigue loading in the patch test model as depicted in Fig.54. The cohesive element is implemented using the standard ABAUS element same as in Section 3 and a user defined element same as in Section 4. The response of the model is plotted in Fig. 55 and Fig. 56 respectively.

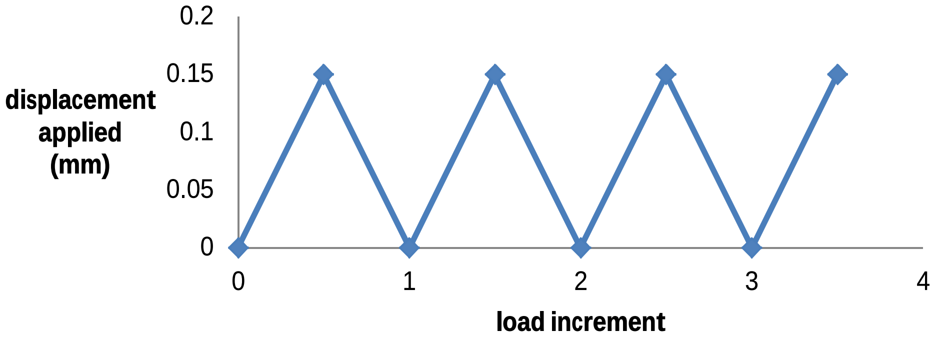

Figure 54 Fatigue Loading Defined as a Sequence of Static Loading

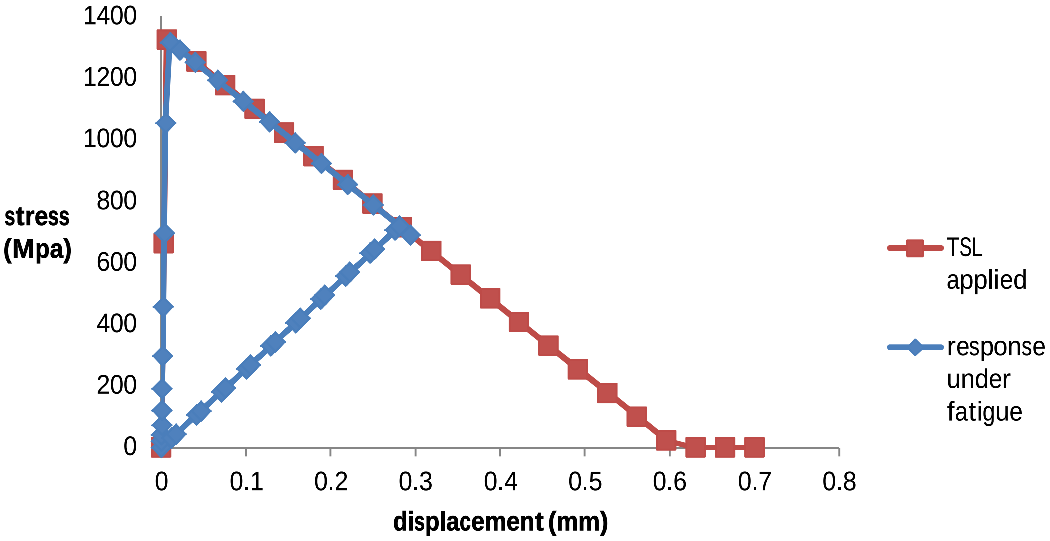

Figure 55 Fatigue Saturation Verification Using Standard Cohesive Element

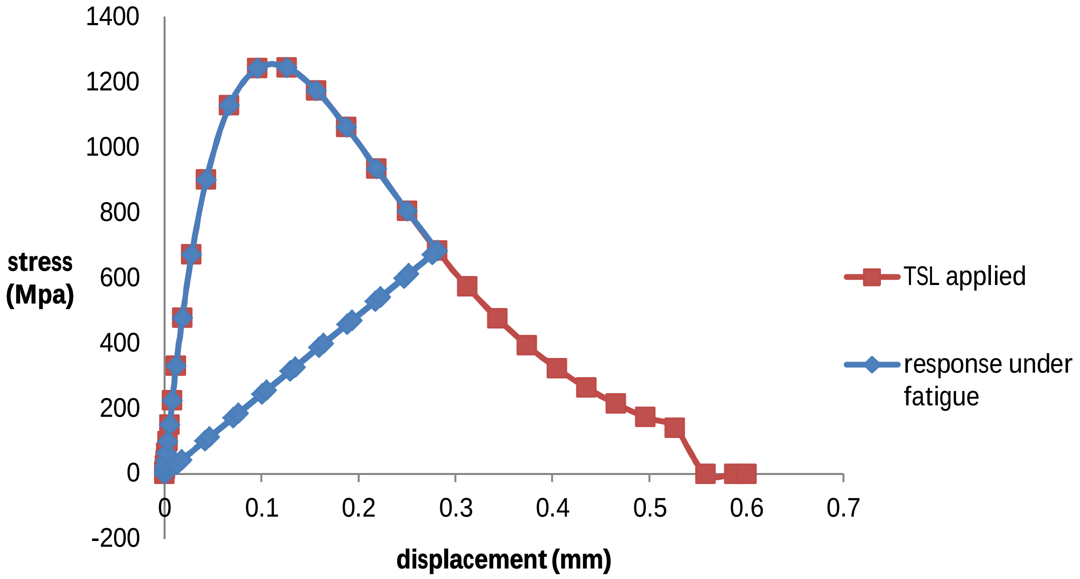

Figure 56 Fatigue Saturation Verification Using UEL A

In both cases, the unloading/reloading algorithm implemented is identified such that a unloading situation where the cracks close completely when no loads acting on the crack faces as mentioned before in Section 2.4.4 Fig.13 (a) The cyclic loading didn't cause any effect on the material deterioration. In other words, with the provide load cycles, the cohesive zone would remain its loading bearing capacity infinitely and thus no crack propagation would be observed. The results have proved the fatigue saturation problem [8]. This suggests that neither the standard cohesive element nor the user element monotonic loading are not able to predict crack behaviour under fatigue loading. New algorithm for the user element in cyclic loading should to be developed.

## 5.2 Damage Evolution Model for Fatigue Crack Propagation

According to Section 2.4.4, as a solution to the saturation problem, a damage variable that increases during load cycles is introduced to capture the material degradation behaviour.

Damage mechanics provides an appropriate method to account for such degradation of the cohesive parameters, where the degradation is implemented by a damage variable $D_c$ . This new state variable is defined as the effective surface density of micro defects in the interface [33], in other words, the value of the damage is quantified as the ratio between the damaged sectional area $A_D$ and the initial sound cross-sectional area $A_0$ , i.e. $D_c = \frac{A_D}{A_0}$ . Meanwhile the effective stress (traction) concept [11] is applied, given as;

$$T_{\text{eff}} A_{eff} = T_0 A_0$$
$$A_{eff} = A_0 - A_D$$

(Eq.28)

From the equations above, the constitutive relation for a cyclic CZM considering damage accumulation is arrived by replacing the traction by the effective traction [33], i.e.

$$T_n = T_{\mathrm{eff}} = \frac{T_0}{1 - D_{\mathrm{c}}}$$

Where $T_0$ is the actual traction in the complete cohesive zone. By substituting the effective traction into the TSL function discussed in Section 4, the cohesive strength is then given as

$$\sigma_{\max} = (1 - D_c)\sigma_{\max,0}$$

Hereby is introduced an existing damage accumulation model proposed by Roe and Siegmund [10],

$$\dot{D}_c = \frac{\Delta\dot{\bar{u}}}{\delta_\Sigma}\left[\frac{\bar{T}}{\sigma_{\max}} - \frac{\sigma_f}{\sigma_{\max,0}}\right] H\left(\sum\Delta\bar{u} - \delta_0\right) \; and \; \dot{D}_c \geq 0$$
$$\Delta\bar{u} = \sqrt{\Delta_n{}^2 + \Delta_t{}^2}, \quad \Delta\dot{\bar{u}} = \Delta\bar{u}_t - \Delta\bar{u}_{t-\Delta t}, \quad \bar{T} = \sqrt{T_n^2 + T_t^2/(2eq)}$$

**(Eq.29)**

The proposition can be related back to the following assumptions [11], [33]

1. Damage only starts to accumulate if a deformation measure, accumulated or current, is greater than a critical magnitude;
2. The increment of damage is related to the increment of deformation as weighted by the current load level;
3. There exists an endurance limit which is a stress level below which cyclic can proceed infinitely without failure.

Based on these three requirements, the evolution equation allows for damage accumulation of the cohesive zone under cyclic loading, which is illustrated as,

$$D_{c,i} = D_{c,i-1} + \dot{D}_c$$

**(Eq.30)**

As one can see, two new variables $\delta_\Sigma$ and $\sigma_f$ are introduced in the model. One of them is $\delta_\Sigma$, the accumulated cohesive length [9], is used to scale the increment of the effective material separation $\Delta\dot{\bar{u}}$. $\delta_\Sigma$ determines the amount of accumulated effective separation necessary to fail the cohesive zone, and is assumed as a multiple of $\delta_0$. The accumulated cohesive length is incorporated into the UEL as $\alpha\delta_0$

The second additional parameter is called the cohesive zone endurance limit $\sigma_f$ [9]. This quantity is incorporated via $\beta = \frac{\sigma_f}{\sigma_{\max,0}}$, the ratio of $\sigma_f$ and the initial undamaged cohesive normal strength: $\sigma_{\max,0}$. No damage accumulation will process if $\frac{\bar{T}}{\sigma_{\max}} < \frac{\sigma_f}{\sigma_{\max,0}}$

Additionally, in damage accumulation model, the Heaviside expression $H\left(\Delta\bar{u} - \delta_0\right)$, describes a threshold value for the damage accumulation. Both theoretical considerations [1], as well as experimental data from high resolution damage measurement indicate the necessity to account for such threshold [33]. Here, the damage accumulation starts once the accumulated effective opening displacement $\sum\Delta\bar{u}$, is greater than the characteristic separation $\delta_0$. In general, one can see that the magnitude of the incremental damage is dependent on the two additional material parameters and the proportional to the scaled and normalized incremental resultant separation, $\Delta\dot{\bar{u}}$ , weighted by a measure of current traction reduced by the endurance limit.

Considering all above, in our case of Mode 1 loading case, the damage accumulation model in Eq.29 can be rewritten in a simplified version as following

$$\dot{D}_c = \frac{\dot{\Delta}_n}{\alpha\delta_0}\left[\frac{T_n}{\sigma_{\max}} - \beta\right] H\left(\Sigma\Delta_n - \delta_0\right) \; and \; \dot{D}_c \geq 0$$

$$\dot{\Delta}_n = \dot{\Delta}_{n,t} - \dot{\Delta}_{n,t-\Delta t},$$

(Eq.31)

With

$$\alpha\delta_0 = \delta_\Sigma; \quad \beta = \frac{\sigma_f}{\sigma_{\max,0}}$$

The material degradation is accomplished by

$$\sigma_{\max} = (1 - D_c)\sigma_{\max,0}$$

(Eq.32)

Please note that it is assumed that the same TSL shape for monotonic loading is also applicable to fatigue loading, based on [2,4,18], as the newly introduced variables for damage accumulation play a major t role in fatigue simulation [2].

## 5.3 Patch Test

Again the patch model as in Fig.16 is applied. The cohesive parameters for the TSL are kept the same as in Section 4.2. The parameters for the damage accumulation is $\alpha = 5, \quad \beta = 0.25$

The fatigue loading under displacement control is plotted as in the Fig.57. The amplitudes for the load cycles are kept constant. The response of the patch test model is plotted similarly as before at the target point in Fig. 58.

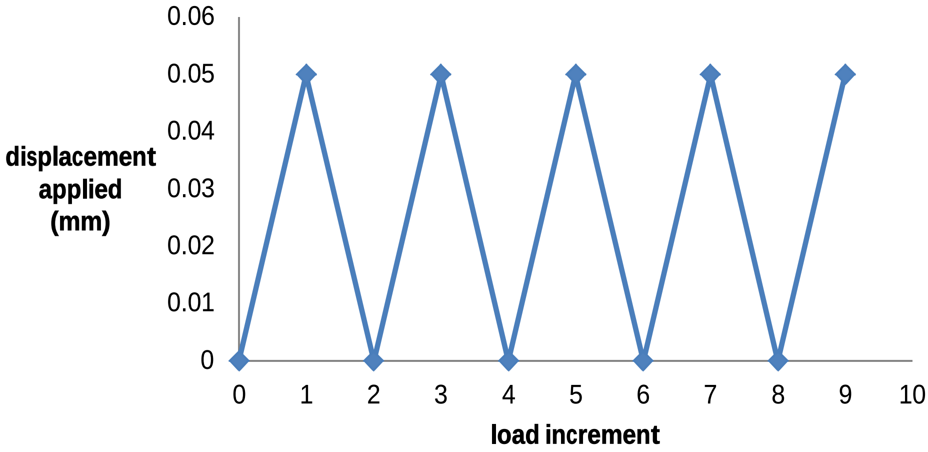

Figure 57 fatigue load definition for the patch test model with UEL B

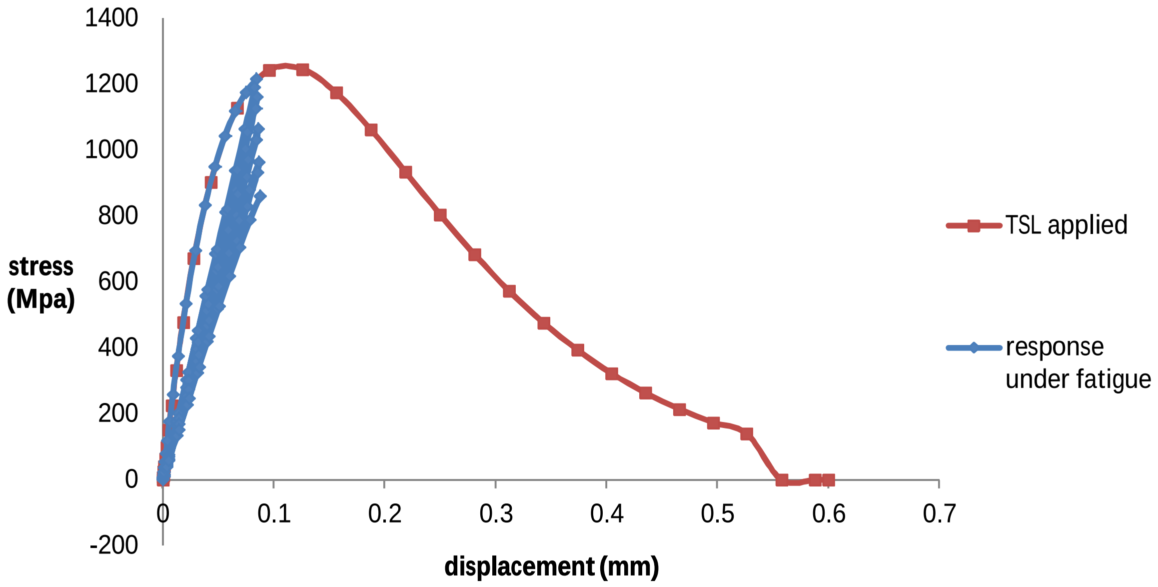

Figure 58 model response at the variation of Alfa=5, Beta=0.25

One can see that the TSL that the element follows is lowered cycle by cycle, which represents the gradual material degradation. As expected, the unloading-reloading in two consecutive load cycles occurs in the same path, e.g. increment 1 to 2 and 2 to 3. However, author didn't define a different path for two non-consecutive load cycles with constant amplitude either even though the damage variable is indeed increasing, which is not the case unexpectedly from the gradual decrease in the traction observable in Fig. 58. This flexibility may come from the analysis setting of the ABAQUS software. Unfortunately, the state variables such as the damage variable is not obtained here due to time limitation, but it is achievable in ABAQUS by converting the user elements into standard elements through a script in Python, see [41]. Therefore the model response can only be viewed in a qualitative manner, so as in the following sections.

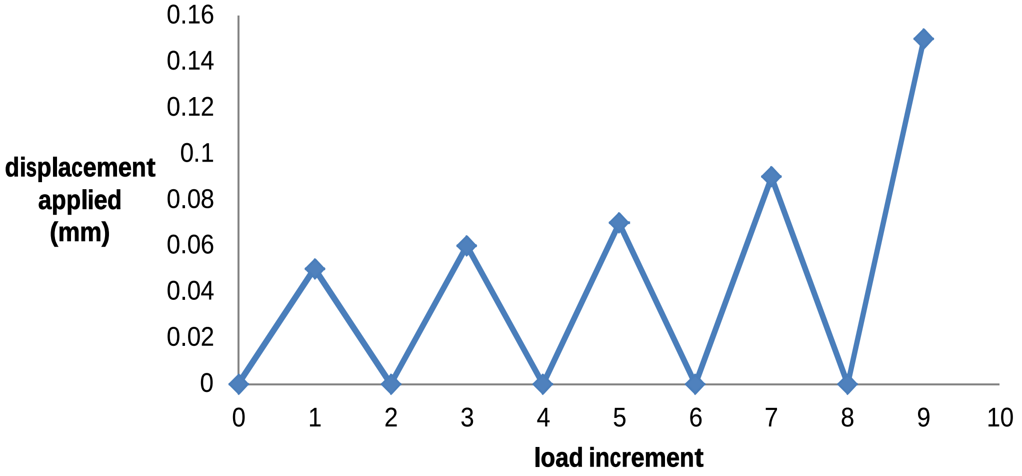

Figure 59 Fatigue Loading Definition with Increasing Amplitude

In order to make the response more observable and also more convenient in comparison in the following parametrical study, another series of cyclic load is applied with the amplitude increasing cycle by cycle to amplify the degradation mechanism, as shown in Fig. 59. The corresponding response is plotted in the Fig. 60.

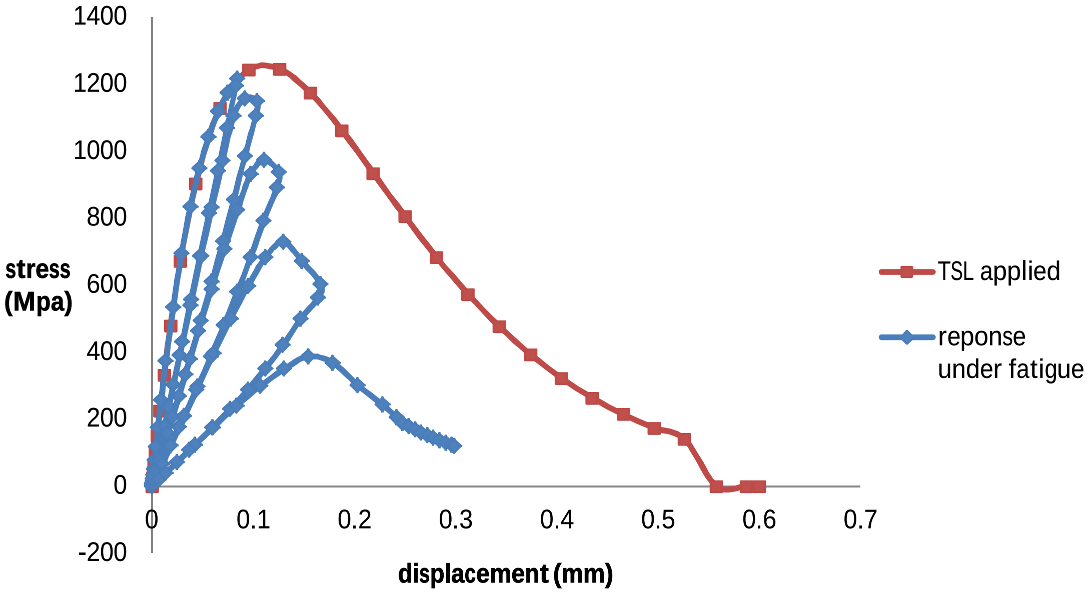

Figure 60 Model Response with Increasing-Amplitude Fatigue Loading (Alfa=5, Beta=0.25).

In Fig.60, one can see that in the first cycle, the response followed the initial TSL because no damage accumulation occurs as the accumulated separation remained below the threshold value $\delta_0$. With the cyclic loading going on, the accumulated separation became larger than $\delta_0$ and damage started to accumulate. Since the load amplitude has been increased, the damage was expected to be larger than the previous one with constant amplitude, which can be justified by the lower traction in the model response in the Fig. 60 than in Fig.58.

## 5.4 Qualitative Study on Damage Model Parameters

As introduced previously, the cohesive endurance limit $\sigma_f$ is the highest traction that can be repeated without failure of the cohesive zone. The accumulated cohesive length $\delta_\Sigma$, normalizes the increment of material separation and therefore determines the magnitude of the damage increment at a given state of load [33]. It is a very important issue to know how would the parameters introduced in the damage accumulation model influence the crack propagation process. Therefore, a series of parametric study is conducted as in Table 5

**Table 5 Plan of Parametrical Study**

| | $\beta = 0.25$ | $\beta = 0.35$ | $\beta = 0.5$ |
|---|---|---|---|
| $\alpha = 4$ | √ | | |
| $\alpha = 5$ | √ | √ | √ |

| | | | |
|---|---|---|---|
| $\alpha = 6$ | √ | | |

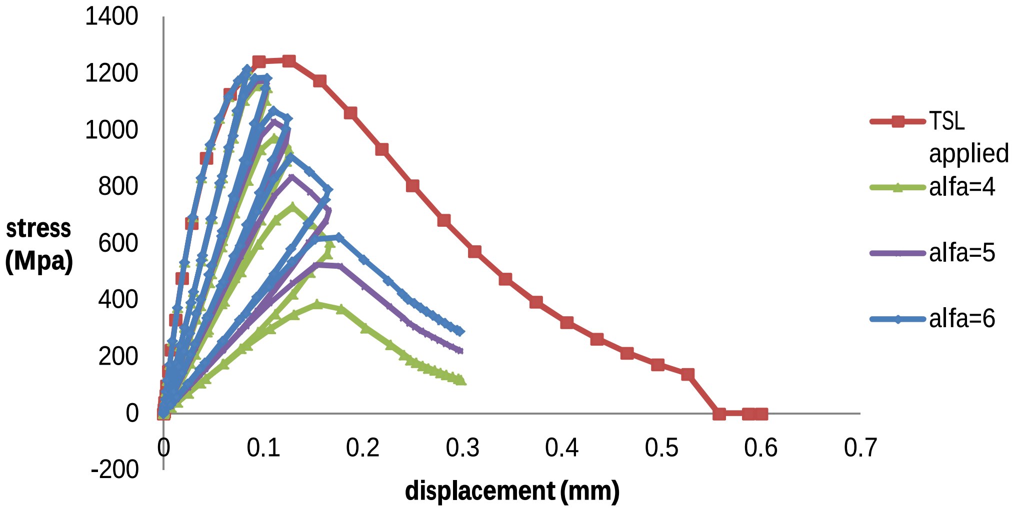

Figure 61 model response at the variation of Alfa, with Beta=0.25

Fig. 61 has suggested that by increasing the value of alfa, more cycles or more accumulated deformation would be required for the same damage increment. Therefore the damage accumulation was delayed as the material degradation at a lower speed.

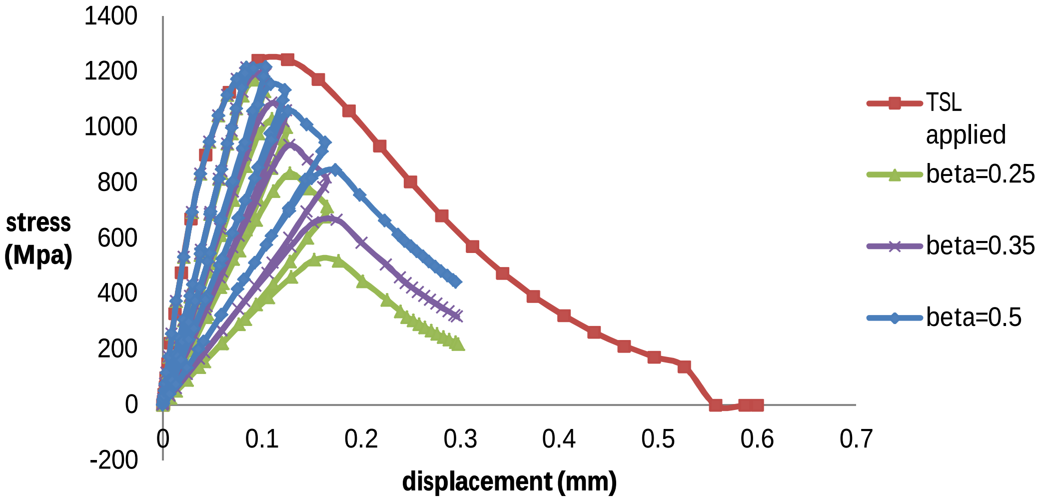

Figure 62 Model response at the variation of Beta, with Alfa=5

Fig. 62 has suggested that by increasing the value of beta, a higher endurance limit reduced the effective load range and thus the damage accumulation was delayed as the material degradation at a lower speed.

The separation in the cohesive zone model can be directly related to the (plastic) strain occurring in the material by a definition of constitutive thickness. From a physical point of view, the repeated variations of loads (in our case, variations of strain), would induce alternate plastic strain in the material. The damage model has incorporated both the concepts of plastic strain and stress via the parameters $\delta_{\Sigma}$ and $\sigma_f$. These two parameter from the damage accumulation model will determine, by definition, the number of cycles to failure at a load level just above the endurance limit, i.e. they can be related to the location of the "knee" of a S-N curve. However, this would be related to the high-cycle fatigue phenomenon. Due to the fact that the CZM here considered crack propagation on a macroscopic level, the models may need to be modified further at much smaller level (meso or micro) and the parameter definition should be established more carefully from both physical and numerical point of view.

## 5.5 Increment Size Dependency

Due to the introduction of $\frac{\bar{T}}{\sigma_{\max}} < \frac{\sigma_f}{\sigma_{\max,0}}$, one may assume that if the increment is large, the damage accumulation may be ignored due to a quick jumping-down the traction. Therefore a larger load increment may delay the accumulation of the damage. In literature this expression is sometimes ignored [12]. However, as verified in the Fig.63, the influences of the increment size do appear in the model response. Therefore, a sufficiently small increment size is suggested during an application of the subroutine UEL in simulation of fatigue crack propagation.

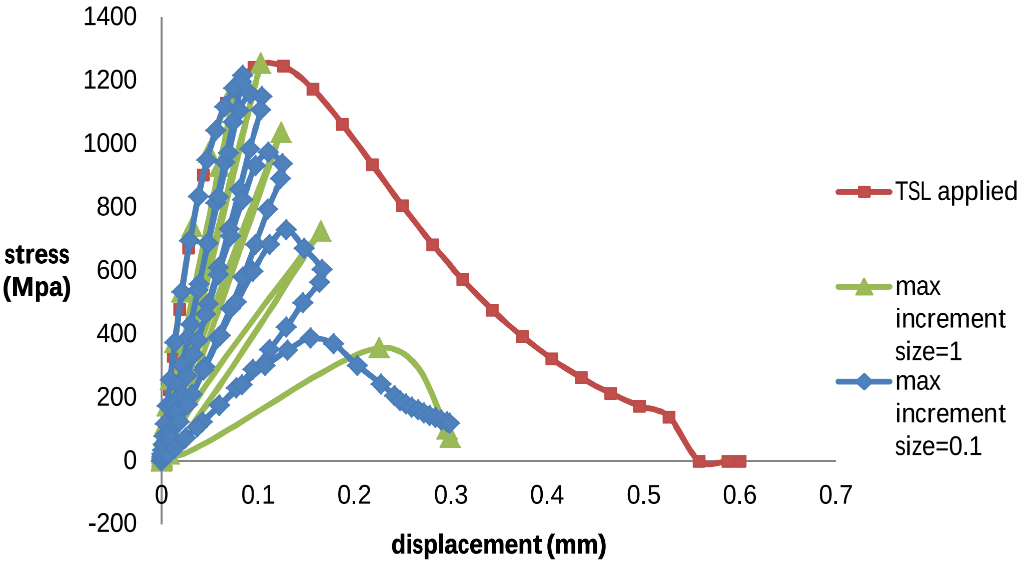

Figure 63 increment size dependency

It is better to check the model features should by looking into the process of damage evolution quantitatively. Since a detailed evolution of the damage variable is not monitored here, the functionality of the UEL for cyclic CZM should be tested further in future applications.

## 5.6 Application of the Cyclic CZM in High-Cycle Fatigue

The scope of the projects focused the crack growth on a macro level, which means the parameters for the phenomenological CZM are related to macroscopic physics. For high-cycle fatigue, especially in case of the non-propagating small cracks, the threshold remote stress range, denoted as the fatigue limit, is more related to the material properties on a micro level [15]. The feasibility of the cyclic cohesive zone model in simulation under high-cycle fatigue is checked in the patch model. A newly cyclic load is defined.

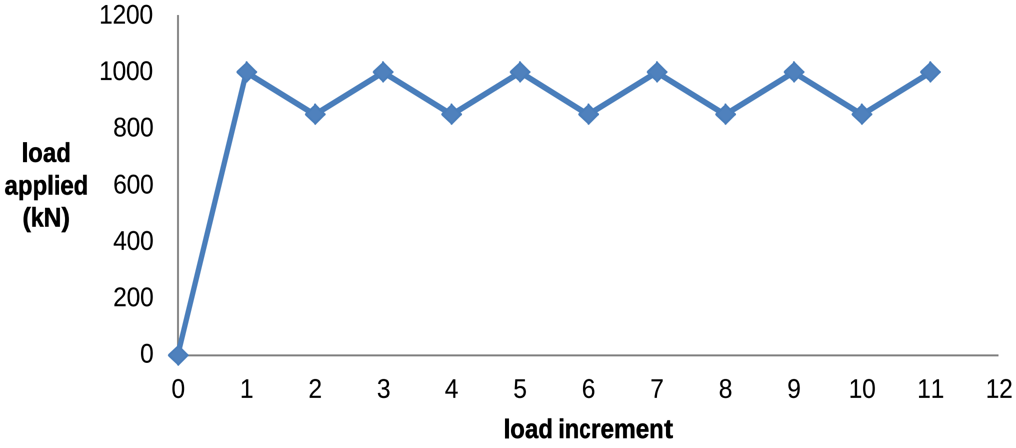

Figure 64 Fatigue Loading Definition

As depicted in Fig.64, the force-controlled load applied cycles between 850 Mpa to 1000 Mpa, with a mean stress level of 925 Mpa. Here it is assumed that the fatigue limit for the current material is $\Delta\sigma = 200Mpa$ for the current load ratio. For the damage accumulation model, alfa=5, beta=0.35. It is easy to recognise that the applied load level have exceeded the endurance limit 0.35*1260=441 Mpa. Please note that the values here are assumed randomly for illustrative purpose. The mean stress level could have been be lower but is applied in a way that the damage evolution is accelerated.

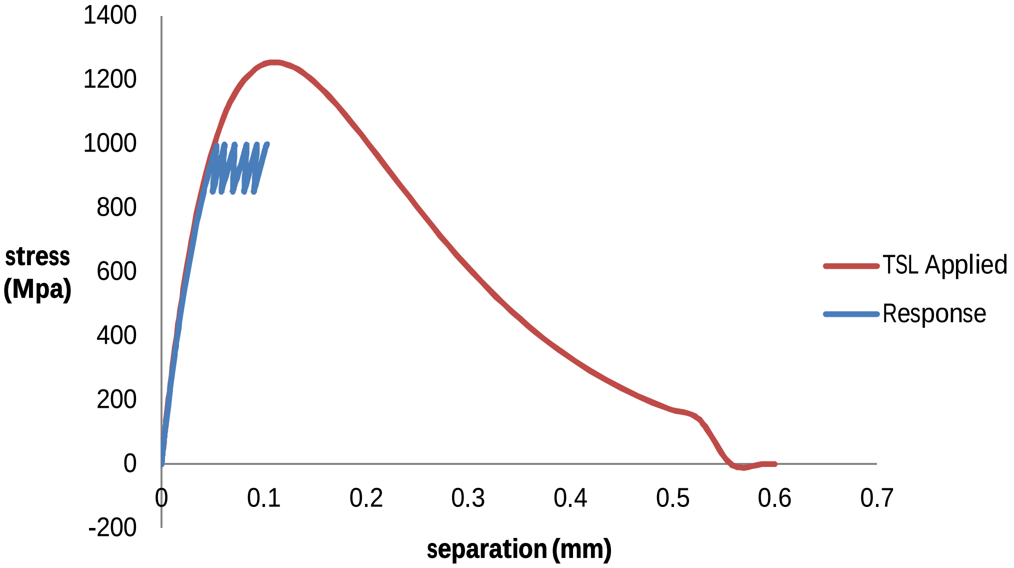

Figure 65 Model Response at Small Load Amplitude

From the model response in Fig.65, one can find that the damage is evolving, which is indicated by the increasing separation required to reach the same imposed load level. However, physically the material is not expected to be governed by the fatigue failure because of the unreached fatigue limit. This implies that the cyclic cohesive zone is only applicable for low-cycle fatigue simulation. Due to the nature of the CZM as a phenomenological model, for smaller length scale, further modification on the damage model may be necessary and the model parameters need to be determined on an according level.

## 6.0 SUMMARIES AND SUGGESTIONS

In this thesis project, author aimed to study the feasibility of the cohesive zone model in numerical simulation of crack propagation in pipeline steel. The commercial analysis coding ABAQUS has provided a standard cohesive element with a triangle-shaped traction separation law, which in the first part of the study has been applied in the parametric study. In the second part the numerical implementation of a different shape of TSL is explored via subroutine UEL A variety of load cases are accounted for. Meanwhile, the application of cohesive zone model in fatigue crack propagation is also studied.

In Section 3, a series of parametric study using a SENT fracture specimen is conducted using the standard cohesive element. The following summaries can be concluded

1) There is a huge difference in the parameter calibration between the suggestions in literature and the ABAQUS standard cohesive element. As a preliminary result, in order to observe crack propagation in pipeline steel, the reasonable values of the cohesive parameters are suggested approximately as

$$\Gamma_n \approx 3\% \frac{K_{Ic}^2}{E'}, \quad \sigma_{\max} \approx 1.5\sigma_y$$

The huge difference also implies that the cohesive parameters recommended from the literature calibrated for a different TSL is not suitable for the triangle-shaped TSL. Thus there exists a TSL-shape dependency for the calibration of the cohesive parameter.

2) The cohesive strength influences the plastification developing near the crack tip. A larger value allows for a higher level of plastification in the material and delays or prevents the full development of the cohesive zone and vice versa. While cohesive energy controls the energy needed for the full development of the cohesive zone. In this way, a larger value of cohesive energy delays the crack initiation and decreases the speed and the amount of crack extension. The size of the cohesive zone tends to stabilize during crack propagation. And the cohesive zone length increases with increased level of cohesive energy. Meanwhile, the triangle-shape TSL, the initial stiffness is found to have a minor influence on the crack propagation.

3) The influences of the cohesive parameters on cracking process are further studied in terms of the J-resistance curves. On one hand, the relationship between the cohesive energy and the J-integral evaluated at the crack initiation can be found as $J_{\text{ini}} = \Gamma_n$. An increase in the cohesive energy represents a higher resistance in crack initiation and extension. The cohesive energy has less influence

on changing the ductility of the crack propagation with the triangle TSL. On the other hand, a higher value of the cohesive strength represents higher ductility of the crack propagation by increasing the slope of the J-resistance curve, the increment in the crack resistance suggests a plastic component $J = \Gamma_n + J_{pl}$ , i.e. the energy input from the applied load is absorbed by both creating new crack surface and plastification of material surrounding the crack tip.

4) The difference between the experiments and simulation results has suggested "more ductile" crack propagation in pipeline steel than the standard cohesive element is able to capture. This implies that the triangle-shaped TSL describes brittle or quasi brittle crack behaviour and is not suitable to model the fracture behaviours of the pipeline steel X65.

In Section 4, based on the proposition of Needleman, the author explored the possibility of implementing a different TSL into a user defined cohesive element for the axis-symmetrical problem. A contact algorithm is implemented successfully accounting for the possible overclosure effect. However, the problem is initially defined as axis-symmetrical, the formulation of the element matrices are also established accordingly. The assumption of totally zero tangential separation may lead to convergence problems especially in elastic-plastic analysis such that future work may be necessary to address this issue in more detail.

In Section 5, the ABAQUS standard cohesive element has been proven incapable in fatigue crack propagation and new algorithm needs to be incorporated in the subroutine UEL. An existing damage accumulation model introducing more model parameters proposed by Roe and Siegmund is applied. Regarding the newly introduced damage model, the influences of two parameters, the accumulative cohesive length $\delta_\Sigma$ and the endurance limit $\sigma_f$ are studied on a qualitative base. The accumulative cohesive length scales the separation increment and determines the number of accumulated separation (or plastic strain) at a specific load level. While the endurance limit incorporates the concept of stress into the damage model and controls the effective load range. The qualitative study verifies the model features and shows the potential of such user cohesive element in parameter calibration in fatigue simulation. The cyclic CZM here describes the damage evolution on a macro scope and is proven more suitable for low-cycle fatigue problems. The functionality of the cyclic CZM needs to be looked into in further applications.

For the future work, it is also very interesting to look into the following aspects:

1) The impact of the material hardening behaviour on the calibration of the cohesive element to have a more rounded understanding in linking the phenomenological model parameters with real material physics;

2) The influences of different TSL shapes on the fracture process for both monotonic loading and fatigue loading, by applying the user cohesive element implementing a user defined TSL;

3) More experimental works shall be necessary for the calibration of the cohesive parameters. The material parameters such as the critical stress intensity factors are not taken from the same material applied for fracture simulation but just as rough estimation from the literature. Although series of variations on the input cohesive parameters have been checked, a more accurately determined experiment value helps to correlate the numerical model to the physical process.

4) Different algorithm in the user element implementation to account for more physically related effects, e.g. different unloading/reloading path allowing for residual separation, shear stiffness definition, damage accumulation model, etc.

5) Specifically for the cyclic cohesive element, an explicit quantitative study on the damage evolution process is necessary to check the model features and its feasibility in simulation of fatigue crack propagation. Moreover, this cyclic CZM is more applicable for low-cycle fatigue simulation on a macroscopic level. For smaller length scale, a different damage model shall be applied and the model parameters may need to be determined more rigorously on an according level.

## REFERENCES

[1] J. Lemaitre, R. Desmorat. Engineering Damage Mechanics. 205 Springer

[2] J. Liu, J. Li, B, Wu. The Cohesive Zone Model for Fatigue Crack Growth. Advances in Mechanical Engineering .Volume 2013.

[3] J.J. Munoz, U. Galvanetto , P. Robinson. On the numerical simulation of fatigue driven delamination with interface elements. International Journal of Fatigue 28 (2006) 1136–1146

[4] H. Li, H. Yuan. Cohesive zone modelling of low cycle fatigue cracks in cracked and notched specimens, Fatigue &Fracture of Engineering Materials & Structures, 2013, 36, 1246-1257.

[5] D. S. Dugdale, Yielding of steel sheets containing slits, Journal of the Mechanics and Physics of Solids, vol. 8, no. 2, pp. 100–104, 1960.

[6] G. I. Barenblatt, The mathematical theory of equilibrium cracks in brittle fracture, Advances in Applied Mechanics, vol. 7, pp. 55–129, 1962.

[7] Needleman, A., 1990. An analysis of decohesion along an imperfect interface. Int. J. Fract. 42, 21-40

[8] Meinhard Kuna, Finite Elements in Fracture Mechanics

[9] B. Wang, T. Siegmund. Simulation of fatigue crack growth at plastically mismatched bi-material interfaces, International Journal of Plasticity 22 (2006) 1586-1609

[10] Roe, K.L., Siegmund, T., 2001. Simulation of interface fatigue crack growth via a fracture process zone model. In: Bathe, K.J. (Ed.), Proc. 1st M.I.T. Conf. Comp. Fluids Solid Mech. Elsevier, Boston, MA, pp. 435-437

[11] Lemaitre J. A Course on Damage Mechanics. Berlin: Springer-Verlag; 1996

[12] Y. Xu, H. Yuan. On damage accumulations in the cyclic cohesive zone model for XFEM analysis of mixed-mode fatigue crack growth. Computational Materials Science 46 (2009) 579–585

[13] S. Silitonga, J. Maljaars, F. Soetens, H. Snijder. Numerical simulation of fatigue crack growth rate and crack retardation due to an overload using a cohesive zone model. 2014, Advanced Materials Research Vols. 891-892 (2014) pp 777-783

[14] Fracture Mechanics: Fundamentals and Application (Third Edition), T.L. Anderson,2005, Taylor & Francis Group

[15] Fatigue of structures and materials, J. Schijve. 2009 Springer Science+Business Media, B.V.

[16] K. Schwalbe, I. Scheider, A. Cornec. Guidelines for Applying Cohesive Models to the Damage Behaviour of Engineering Materials and Structures, 2013, Springer

[17] G. Pluvinage, J. Capelle, Z. Azari**,** Design based on ductile-brittle transition temperature for API 5L X65 steel used for dense CO2,

[18] I. Aguirre, I. Ferreira. Experimental and Numerical Analysis for SE(B) and SE(T) J-integral Fracture Toughness Testing. 18th International Congress of Mechanical Engineering, 2005

[19] Sunil Bhat, Vijay G. Ukadgaonker. Dugdale cohesive zone modeling to evaluate J integral at the interface of strength mismatched steels: A simplified numerical approach, Finite Elements in Analysis and Design 46 (2010) 601–610

[20] W. Brocks and I. Scheider. Numerical Aspects of the Path-Dependence of the J-Integral in Incremental Plasticity, 2001, Technical Note GKSS/WMS/01/08 internal report

[21] I. Scheider, W. Brocks, The effect of the traction separation law on the results of cohesive zone crack propagation analyses.

[22] I. Scheider, W. Brocks, Effect of Cohesive Law and Triaxiality Dependence of Cohesive Parameters in Ductile Tearing

[23] I. Scheider, W. Brocks, Cohesive elements for thin-walled structures. Computational Materials Science 37 (2006) 101–109

[24] I. Scheider, M. Rajendran, A. Banerjee. Comparison of different stress-state dependent cohesive zone models applied to thin-walled structures. Engineering Fracture Mechanics 78 (2011) 534–543

[25] I. Scheider, Schödel, M. and Schönfeld, W., Crack Propagation Analysis with CTOA and Cohesive Model: Comparison and Experimental Validation.

[26] I. Scheider, V. Uz, N. Huber, Applicability of the Cohesive Model to Fracture of Light-weight Structures: Parameter Identification and Thickness Dependence.

[27] B. Wang, T. Siegmund, Numerical simulation of constraint effects in fatigue crack growth. International Journal of Fatigue 27 (2005) 1328–1334

[28] J. Liu, C. Xiang, H. Yuan, Prediction of 3D small fatigue crack propagation in shot-peened specimens. Computational Materials Science 46 (2009) 566–571

[29] R.D. de Bort, L.J.Sluijs, Computational Methods in Non-linear Solid Mechanics, 2013

[30] Stine Vethe, Numerical Simulation of Fatigue Crack Growth, Mater thesis in Norwegian University of Science and Technology. 2012

[31] T. Yamaguchi, T. Okabe, S. Yashiro. Fatigue simulation for titanium/CFRP hybrid laminates using cohesive elements.

[32] S. Silitonga, J. Maljaars, F. Soetens, H.H. Snijder. Numerical Simulation of Fatigue Crack Growth Rate Using a Cohesive Zone Model . ECCOMAS 2012.

[33] Roe, K.L., Siegmund, T., An irreversible cohesive zone model for interface fatigue crack growth simulation. Engineering Fracture Mechanics 70 (2003) 209–232

[34] Y. Xu, H. Yuan, Computational modeling of mixed-mode fatigue crack growth using extended finite element methods. Int J Fract (2009) 159:151–165

[35] Kyoungsoo Park, Glaucio H. Paulino, Computational implementation of the PPR potential-based cohesive model in ABAQUS: Educational perspective. Engineering Fracture Mechanics 93 (2012) 239–262

[36] Williams ML (1957) On the stress distribution at the base of a stationary crack. J Appl Mech 24:109–114

[37] Irwin GR (1957) Analysis of stresses and strains near the end of a crack traversing a plate. J Appl Mech 24:361–364

[38] Griffith AA (1921) The phenomena of rupture and flow in solids. Philos Trans Ser A 221: 163–198

[39] Tvergaard, V., Hutchinson, J.W.: The relation between crack growth resistance and fracture

process parameters in elastic-plastic solids. J. Mech. Phys. Solids 40, 1377–1397 (1992)

[40] ASTM-E 1820 (2007) Standard test method for measurement of fracture toughness. Technical Report, American Society for Testing and Materials, West Conshohocken

[41] ABAQUS 6.10 Manual Documentation

[42] Frost, N.E., Marsh, K.J. and Pook, L.P., Metal Fatigue. Clarendon, Oxford (1974).

[43] Paris, P.C., Gomez, M.P. and Anderson, W.E., A rational analytical theory of fatigue. The Trend of Engineering, Vol. 13 (1961), pp. 9–14.

[44] Paris, P.C. and Erdogan, F., A critical analysis of crack propagation laws. Trans. ASME, Series D, Vol. 85 (1963), pp. 528–535

[45] Forman, R.G., Kearney, V.E. and Engle, R.M., *Numerical analysis of crack propagation in cyclic-loaded structures*. J. Basic Engrg., Trans. ASME, Vol. D89 (1967), pp. 459–464.

[46] Priddle, E.K., *High cycle fatigue crack propagation under random and constant amplitude loadings*. Int. J. Pressure Vessels & Piping, Vol. 4 (1976), p.89.

[47] Hillerborg, A., Modeér, M., Petersson, P.E.: Analysis of crack formation and crack growth in concrete by means of fracture mechanics and finite elements. Cem. Concr. Res. 6, 773–782 (1976)

[48] Project Group DMS466b, Formulation of Cohesive Finite Element for Analysing Strength of Wrinkles in Glass-Epoxy Laminates. 2013. Aalborg University.

[49] V. Olden, A. Alvaro, O. M. Akselsen. Hydrogen diffusion and hydrogen influenced critical stress intensity in an API X70 pipeline steel welded joint e Experiments and FE simulations.2012

## **APPENDIX** INPUT FILE FOR VERIFCATION OF THE UEL IMPLEMENTATION

```
*Heading
** Job name: ueltest Model name: Model-1
** Generated by: Abaqus/CAE 6.10-1
*Preprint, echo=NO, model=NO, history=NO, contact=NO
**
** PARTS
**
*Part, name=Part-1
*Node
      1,           0.,           0.
      2,           1.,           0.
      3,           1.,  0.100000001
      4,           0.,  0.100000001
      5,           1.,   1.10000002
      6,           0.,   1.10000002
*USER ELEMENT, TYPE=U1, NODES=4, COORDINATES=2, PROPERTIES=6,
VARIABLES=5
1,2
*Element, type=U1
1, 1, 2, 3, 4
*Element, type=CPS4R
2, 4, 3, 5, 6
*Nset, nset=_PickedSet11, internal, generate
 3,  6,  1
*Elset, elset=_PickedSet11, internal
 2,
** Section: steelsection
*Solid Section, elset=_PickedSet11, material=steel
,
*End Part
**
**
** ASSEMBLY
**
*Assembly, name=Assembly
**
*Instance, name=Part-1-1, part=Part-1
*End Instance
**
*Nset, nset=_PickedSet4, internal, instance=Part-1-1
 1, 2
*Elset, elset=_PickedSet4, internal, instance=Part-1-1
 1,
*Nset, nset=_PickedSet8, internal, instance=Part-1-1
 5, 6
*Elset, elset=_PickedSet8, internal, instance=Part-1-1
 2,
*Nset, nset=_PickedSet10, internal, instance=Part-1-1
 5, 6
*Elset, elset=_PickedSet10, internal, instance=Part-1-1
 2,
*Nset, nset=_PickedSet11, internal, instance=Part-1-1
 5, 6
*Elset, elset=_PickedSet11, internal, instance=Part-1-1
```

```
 2,
*Nset, nset=_PickedSet12, internal, instance=Part-1-1
 5, 6
*Elset, elset=_PickedSet12, internal, instance=Part-1-1
 2,
*Nset, nset=_PickedSet13, internal, instance=Part-1-1
 5, 6
*Elset, elset=_PickedSet13, internal, instance=Part-1-1
 2,
*Nset, nset=_PickedSet15, internal, instance=Part-1-1
 5, 6
*Elset, elset=_PickedSet15, internal, instance=Part-1-1
 2,
*Elset, elset=cohset, instance=Part-1-1
 1,
*Elset, elset=continuum, instance=Part-1-1
 2,
*End Assembly
*Amplitude, name=Amp-5
        0.,         0.,         1.,         0.5,         2.,         0.,         3.,         0.6
        4.,         0.,         5,          0.7,         6.,         0.,         7.,         0.9
        8.,         0.,         9.,         1.5
**
** MATERIALS
**
*Material, name=steel
*Elastic
211000., 0.3
*UEL PROPERTY, ELSET=cohset
378.7, 0.4, 1260, 1, 4, 0.25
**
** BOUNDARY CONDITIONS
**
** Name: BC Type: Symmetry/Antisymmetry/Encastre
*Boundary
_PickedSet4, PINNED
** ----------------------------------------------------------------
**
** STEP: loadunload
**
*Step, name=loadunload, inc=1000
*Static
0.001, 10., 1e-07, 0.1
**
** BOUNDARY CONDITIONS
**
** Name: load Type: Displacement/Rotation
*Boundary, amplitude=Amp-5
_PickedSet15, 2, 2, 0.1
**
** CONTROLS
**
*Controls, reset
*Controls, analysis=discontinuous
*Controls, parameters=field, field=displacement
, , , , , , ,
**
```

```
** OUTPUT REQUESTS
**
*Restart, write, frequency=0
**
** FIELD OUTPUT: foutput
**
*Output, field
*Node Output
CF, RF, U
*Element Output, directions=YES
FV, LE, MFR, PE, PEEQ, PEMAG, S, SDV, STATUS, STATUSXFEM, UVARM
**
** HISTORY OUTPUT: H-Output-2
**
*Output, history, variable=PRESELECT
*End Step
```